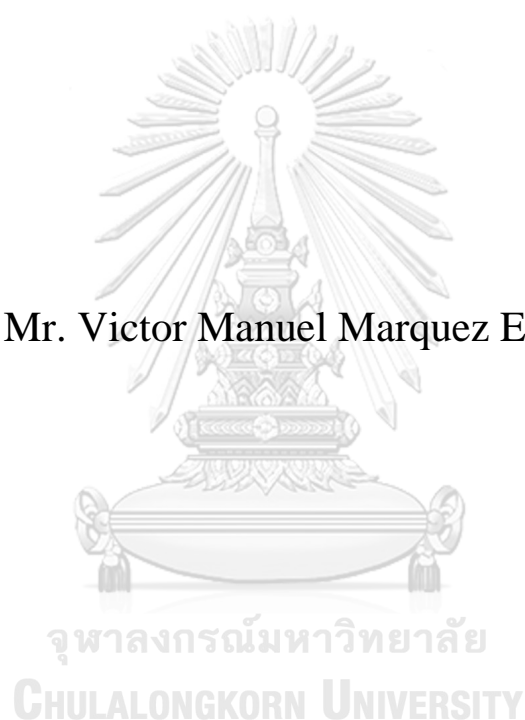


Electrocatalytic hydrogenation of Nitrobenzene on high entropy materials (HEMs)

Mr. Victor Manuel Marquez Espinoza



A Dissertation Submitted in Partial Fulfillment of the Requirements
for the Degree of Doctor of Engineering in Chemical Engineering
Department of Chemical Engineering
FACULTY OF ENGINEERING
Chulalongkorn University
Academic Year 2022
Copyright of Chulalongkorn University

ไฮโดรเจนช่องทางไฟฟ้าของไนโตรเบนซีนบนวัสดุที่มีเอนโทรปีสูง (HEMs)



วิทยานิพนธ์นี้เป็นส่วนหนึ่งของการศึกษาตามหลักสูตรปริญญาวิศวกรรมศาสตรดุษฎีบัณฑิต

สาขาวิชาวิศวกรรมเคมี ภาควิชาวิศวกรรมเคมี

คณะวิศวกรรมศาสตร์ จุฬาลงกรณ์มหาวิทยาลัย

ปีการศึกษา 2565

ลิขสิทธิ์ของจุฬาลงกรณ์มหาวิทยาลัย

| | |
|-------------------|---|
| Thesis Title | Electrocatalytic hydrogenation of Nitrobenzene on high entropy materials (HEMs) |
| By | Mr. Victor Manuel Marquez Espinoza |
| Field of Study | Chemical Engineering |
| Thesis Advisor | Professor PIYASAN PRASERTHDAM |
| Thesis Co Advisor | Associate Professor SUPAREAK PRASERTHDAM |

Accepted by the FACULTY OF ENGINEERING, Chulalongkorn University
in Partial Fulfillment of the Requirement for the Doctor of Engineering

..... Dean of the FACULTY OF
ENGINEERING
(Professor SUPOT TEACHAVORASINSKUN)

DISSERTATION COMMITTEE

..... Chairman
(Associate Professor Okorn Mekasuwandumrong)
..... Thesis Advisor
(Professor PIYASAN PRASERTHDAM)
..... Thesis Co-Advisor
(Associate Professor SUPAREAK PRASERTHDAM)
..... Examiner
(Professor BUNJERD JONGSOMJIT)
..... Examiner
(Professor JOONGJAI PANPRANOT)
..... Examiner
(Professor TAWATCHAI CHARINPANITKUL)

จุฬาลงกรณ์มหาวิทยาลัย
CHULALONGKORN UNIVERSITY

วิกเตอร์ มานูเอล มาเคซช เอสปิโนซา : ไฮโดรเจนชั้นทางไฟฟ้าของไนโตรเบนซินบนวัสดุที่มีเอนโทรปีสูง (HEMs). (Electrocatalytic hydrogenation of Nitrobenzene on high entropy materials (HEMs)) อ.ที่ปรึกษาหลัก : ปิยะสาร ประเสริฐธรรม, อ.ที่ปรึกษาร่วม : สุกฤกษ์ ประเสริฐธรรม

ภาวะโลกร้อนและมลพิษต่อสิ่งแวดล้อมเป็นความท้าทายสำคัญสองประการที่เป็นที่จับตามองในวงการวิจัย ณ ขณะนี้ ปฏิริยาไฮโดรเจนชั้นโดยการเร่งปฏิริยาเชิงไฟฟ้าของไนโตรเบนซินสามารถจัดการกับปัญหาสองประการดังกล่าวได้ในทางหนึ่งนั้นนี่ถือเป็นตัวเลือกหนึ่งในการแทนที่กระบวนการการผลิตอะนิลีนซึ่งขาดแคลนทรัพยากรและไม่เป็นมิตรต่อสิ่งแวดล้อม ที่ใช้งานในปัจจุบัน อีกทางหนึ่งปฏิริยานี้ นับเป็นกระบวนการที่จะสามารถเพิ่มประสิทธิภาพในการย่อยสลายสำหรับการใช้เทคโนโลยีบำบัดน้ำเสียซึ่งเป็นที่จับตามอง โดยใช้ไนโตรเบนซินเป็นตัวแทนของสารมลพิษในน้ำ ด้วยการนี้ผู้วิจัยสนใจศึกษาปฏิริยาไฮโดรเจนชั้นโดยการเร่งปฏิริยาเชิงไฟฟ้าของไนโตรเบนซินโดยใช้วัสดุเอนโทรปีสูง (HEMs) เพื่อทำหน้าที่เป็นวัสดุอิเล็กโทรด งานนี้ใช้วิธีการหลากหลายวิธีเพื่อสังเคราะห์วัสดุโลหะผสมเอนโทรปีสูง (HEAs) และ ออกไซด์เอนโทรปีสูง (HEOs) อีกทั้งมีการวิเคราะห์สมบัติทางกายภาพและเชิงเคมีไฟฟ้าเพื่อหาความสัมพันธ์ระหว่างสมบัติของตัวเร่งปฏิริยาและความว่องไวในการเร่งปฏิริยาไฮโดรเจนชั้น ทั้งนี้ได้ทำการศึกษาผลของศักย์ไฟฟ้าที่จ่าย (0.0 ถึง -2.0 โวลต์) ที่ค่าพีเอชต่าง ๆ ของสารละลาย (5 และ 14) ที่ความเข้มข้น 400 μM พบว่าค่าการเลือกเกิดจำเพาะของปฏิริยาขึ้นกับความเข้มข้นของไฮโดรเจนที่ผลิตได้บนผิวของตัวเร่งปฏิริยา การศึกษาผลของอุณหภูมิการทำแอนนิลิ่ง เผยให้เห็นสมบัติเชิงสัณฐานที่แตกต่างกันซึ่งแปลผลได้ผ่านประสิทธิภาพของการเกิดปฏิริยาไฮโดรเจนชั้นของ HEOs โดยพบความสัมพันธ์ที่ชัดเจนระหว่างความเข้มข้นของช่องว่างของออกซิเจน สมบัติรีดอกซ์ของตัวเร่งปฏิริยา และ ความว่องไวในการเกิดปฏิริยาไฮโดรเจนชั้น สุดท้ายนี้จะทำการให้ความร้อนที่ 500 $^{\circ}\text{C}$ แก่วัสดุ HEO (ชื่อ HEO500) เพื่อใช้ในการประเมินการสลายไนโตรเบนซินในตัวอย่างที่มีน้ำเป็นส่วนประกอบที่ความเข้มข้นตั้งแต่ 100 ถึง 1000 μM ซึ่งให้ค่าการสลายที่สูงยิ่งมากกว่า 90 % ($E_{\text{app}} = 1.7 \text{ V vs Ag/AgCl}$) ภายใต้ภาวะการไหลอากาศเข้า (aerated condition)) แสดงให้เห็นถึงบทบาทสำคัญของ อนุภาคซูเปอร์ออกไซด์ (super-oxide radical ($\text{O}_2^{\bullet-}$)) ในกลไกการกำจัดมลพิษ กลไกการเสื่อมสภาพหลายตัว หาโดยความล้มเหลวเชิงกลของอิเล็กโทรดเป็นกลไกเสื่อมที่สำคัญที่สุดตามมาด้วยการเปลี่ยนแปลงพื้นที่เหนี่ยวนำโดยความต่างศักย์ไฟฟ้า

จุฬาลงกรณ์มหาวิทยาลัย
CHULALONGKORN UNIVERSITY

สาขาวิชา วิศวกรรมเคมี
ปีการศึกษา 2565

ลายมือชื่อนิสิต
ลายมือชื่อ อ.ที่ปรึกษาหลัก
ลายมือชื่อ อ.ที่ปรึกษาร่วม

6471044921 : MAJOR CHEMICAL ENGINEERING

KEYWOR High entropy alloys, High entropy oxides, Nitrobenzene

D: hydrogenation, Electrocatalysis

Victor Manuel Marquez Espinoza : Electrocatalytic hydrogenation of Nitrobenzene on high entropy materials (HEMs). Advisor: Prof. PIYASAN PRASERTHDAM Co-advisor: Assoc. Prof. SUPAREAK PRASERTHDAM

Global warming and environmental pollution are two of the major challenges currently in the spotlight of the research community. Nitrobenzene electrocatalytic hydrogenation could simultaneously tackle two problems. In the first place, as an option to replace the resource-inefficient and non-environmentally friendly processes for aniline production used nowadays. Also, as a viable and applicable process to enhance the degradation efficiency for wastewater treatment rising technologies, using nitrobenzene as a model pollutant. Herein, We present a comprehensive study of the nitrobenzene catalytic hydrogenation using high entropy materials (HEMs) as electrode materials. Different synthesis methods were used to produce high entropy alloys (HEAs) and high entropy oxides (HEOs), and extensive physical and electrochemical characterization was performed to establish correlations between the catalyst's properties and the hydrogenation catalytic activity. The effect of the applied potential (0.0 - -2.0 V) was evaluated in different solution pH (5 and 14) using a concentration of 400 μM , and the selectivity of the reaction was found to be dependent on the surface concentration of hydrogen produced. A study on the effect of the annealing temperature revealed different morphological properties which were reflected in the hydrogenation performance of the HEOs, showing a clear correlation between the oxygen vacancies concentration, the redox properties of the catalysts, and the hydrogenation activity. Finally, a selected material heat treated at 500 $^{\circ}\text{C}$ (HEO500) was used to evaluate the nitrobenzene degradation in aqueous media, with concentrations ranging from 100 to 1000 μM , with outstanding results above 90% degradation ($E_{\text{app}} = 1.7 \text{ V}$ vs Ag/AgCl in aerated condition), showing the important role played by the superoxide radical ($\text{O}_2^{\cdot-}$) in the extensive mineralization mechanism. Several deactivation mechanisms were observed where the mechanical failure of the electrode was the most important one, followed by the potential-promoted surface transformations.

Field of Study: Chemical Engineering

Student's Signature

Academic 2022

.....
Advisor's Signature

Year:

.....
Co-advisor's Signature

.....

ACKNOWLEDGEMENTS

First of all, I would like to thank God.

Second, I thank my family for all their support during this process.

Thanks to Professor Piyasan Prasertdam for giving me the opportunity and trust to carry on this research project, and for giving timely advice and support.

I would also like to acknowledge the research team I worked with for the last years, especially Professor Oswaldo Nuñez, Mohammad Fereidooni, Mohammad Yazdanpanah, Dr. Janaina Santos, Dr. Chistian Paz, as well as all the great students I've met along the doctoral program.

I am also grateful to Professor Supareak Prasertdam for co-advising my project and to the whole computational team Dr. Tinakorn, Dr. Meena, and Dr. Jasmin for the fruitful discussions and valuable insights.

A special mention to the thesis committee members for the time invested in the evaluation of this project, and for the valuable comments and recommendations to improve the quality of the final manuscript.

I would like to acknowledge the staff of the department of chemical engineering at Chulalongkorn University for their valuable assistance and guidance through the administrative processes.

Finally, I'd like to extend an acknowledgment to Chulalongkorn University and the C2F foundation for the funding and resources provided in the pursuit of the research project.

Victor Manuel Marquez Espinoza

TABLE OF CONTENTS

| | Page |
|---|-------------|
| ABSTRACT (THAI) | iii |
| ABSTRACT (ENGLISH) | iv |
| ACKNOWLEDGEMENTS | v |
| TABLE OF CONTENTS | vi |
| LIST OF TABLES | ix |
| LIST OF FIGURES | x |
| CHAPTER I: | 1 |
| INTRODUCTION | 1 |
| 1.1 Objective | 4 |
| 1.2 Scope of the Research | 4 |
| CHAPTER II: | 1 |
| BACKGROUND AND LITERATURE REVIEW | 1 |
| 2.1 Nitrobenzene uses and hazards | 1 |
| 2.2 Nitrobenzene and Aniline industry | 2 |
| 2.3 Nitroarenes hydrogenation | 3 |
| 2.3.1 Nitrobenzene electrocatalytic hydrogenation | 7 |
| 2.3.1.1 Hydrogen evolution reaction | 7 |
| 2.3.1.2 Hydrogen transfer reaction | 8 |
| 2.4 Nitrobenzene degradation | 10 |
| 2.5 High entropy materials (HEMs) | 12 |
| 2.5.1 High entropy alloys (HEAs) | 13 |
| 2.5.2 High entropy oxides (HEOs) | 14 |
| CHAPTER III: | 16 |
| EXPERIMENTAL SECTION | 16 |
| 3.1 Catalysts synthesis | 16 |

| | |
|---|----|
| 3.1.1 HEAs synthesis..... | 16 |
| 3.1.2 HEOs synthesis..... | 17 |
| 3.2 Electrodes preparation..... | 17 |
| 3.3 Catalysts characterization..... | 18 |
| 3.3.1 SEM-EDX..... | 18 |
| 3.3.2 HR-TEM..... | 19 |
| 3.3.3 X-ray diffraction..... | 19 |
| 3.3.4 X-ray photoelectron spectroscopy (XPS)..... | 19 |
| 3.3.5 Fourier transformed Infra-red (FT-IR)..... | 19 |
| 3.3.6 TGA and DSC..... | 20 |
| 3.3.7 Surface area measurements (BET)..... | 20 |
| 3.3.8 Electrochemical measurements..... | 20 |
| 3.4 Nitrobenzene concentration measurement..... | 20 |
| 3.5 Nitrobenzene hydrogenation..... | 21 |
| 3.6 Nitrobenzene degradation..... | 21 |
| CHAPTER IV:..... | 23 |
| RESULTS AND DISCUSSION..... | 23 |
| 4.1 Catalysts physical characterization..... | 23 |
| 4.1.1 High entropy alloys (HEAs)..... | 23 |
| 4.1.1.1 SEM-EDX..... | 23 |
| 4.1.1.2 HR-TEM..... | 24 |
| 4.1.1.3 XPS analysis..... | 26 |
| 4.1.1.4 X-ray diffraction..... | 29 |
| 4.1.1.5 FT-IR analysis..... | 30 |
| 4.1.2 High entropy oxides (HEOs)..... | 31 |
| 4.1.2.1 SEM-EDX..... | 31 |
| 4.1.2.2 X-ray diffraction..... | 33 |
| 4.1.2.3 TGA and DSC..... | 34 |
| 4.1.2.4 FT-IR analysis..... | 36 |

| | |
|---|----|
| 4.1.2.5 XPS analysis | 38 |
| 4.2 High entropy condition..... | 42 |
| 4.3 Catalysts electrochemical characterization..... | 43 |
| 4.3.1 Linear sweep voltammetry | 43 |
| 4.3.2 Cyclic voltammetry | 50 |
| 4.3.2.1 Electrochemical behavior of HEA in acid medium..... | 50 |
| 4.3.2.2 Electrochemical behavior of HEA in Alkaline medium..... | 51 |
| 4.3.2.3 Electrochemical behavior of HEOs | 53 |
| 4.3.3 Electrochemical impedance spectroscopy | 56 |
| 4.3.3.1 The impedance of HEA in acid medium | 56 |
| 4.3.3.2 The impedance of HEA in alkaline medium | 58 |
| 4.3.3.3 The impedance of HEOs..... | 60 |
| 4.4 Electrocatalytic hydrogenation of Nitrobenzene | 63 |
| 4.4.1 Hydrogenation over HEAs | 63 |
| 4.4.2 Hydrogenation over HEOs | 67 |
| 4.5 Electrocatalytic degradation of nitrobenzene | 72 |
| 4.6 Catalysts Stability..... | 78 |
| CHAPTER V: | 84 |
| CONCLUSIONS AND RECOMMENDATIONS | 84 |
| 5.1 Conclusions | 84 |
| 5.2 Recommendations | 85 |
| REFERENCES | 86 |
| VITA..... | 99 |

LIST OF TABLES

| | Page |
|--|-------------|
| Table 1: Elemental composition of the synthesized materials measured by TEM-EDX** | 26 |
| Table 2: Elemental composition of the synthesized HEA/g-40 material measured by SEM-EDX and XPS* | 28 |
| Table 3: Elemental composition of the synthesized HEA/g-80 material measured by SEM-EDX and XPS* | 28 |
| Table 4: Elemental composition of the synthesized HEA/g-120 material measured by SEM-EDX and XPS* | 28 |
| Table 5: FT-IR Peaks HEAs from figure 20..... | 31 |
| Table 6: Physical analysis of the catalysts synthesized using different calcination temperatures..... | 36 |
| Table 7: FT-IR peaks assignation in Figure 25..... | 37 |
| Table 8: Surface concentration of different oxygen species on the surface of the catalysts measured by XPS. | 40 |
| Table 9: Fitting parameters extracted from EIS analysis of figure 42d..... | 63 |
| Table 10: Elements concentration on the HEO500 electrode before and after stability tests | 83 |

LIST OF FIGURES

| | Page |
|--|-------------|
| Figure 1: Nitrobenzene structure and GHS hazard classification..... | 1 |
| Figure 2: Different products derived from the aniline production..... | 2 |
| Figure 3: Haber mechanism for nitrobenzene hydrogenation mechanism | 5 |
| Figure 4: Nitrobenzene hydrogenation mechanism proposed by Makaryan and Savchenko[63]. | 5 |
| Figure 5: Nitrobenzene direct hydrogenation mechanism proposed by Visentin et al.[38]...... | 6 |
| Figure 6: Nitrobenzene hydrogenation mechanism with different possible pathways[56]...... | 7 |
| Figure 7: Scheme for selective catalytic hydrogenation of nitrobenzene mediated by the adsorbed hydrogen. | 10 |
| Figure 8: Schematic representation of the nitrobenzene degradation promoted by the hydrogenation step[75]. | 11 |
| Figure 9: a) Different “binding peaks” and the effect on different surface reactions. b) Schematic representation of the “cascade effect” on a HEA[37]. | 14 |
| Figure 10: XRD patterns of an equimolar mixture of MgO, NiO, ZnO, CuO, and CoO treated at different temperatures. Samples stabilized for 2 hr in air atmosphere and quenched by extracting from the oven[83]. | 15 |
| Figure 11: Schematic representation of the HEAs supported on graphite synthesis procedure..... | 16 |
| Figure 12: Schematic representation of the HEOs synthesis procedure. | 17 |
| Figure 13: Schematic representation of the preparation of electrodes..... | 18 |
| Figure 14: Schematic representation of the cell configurations used. a) separate compartments cell. b) single-compartment cell | 22 |
| Figure 15: SEM images with different magnifications of the three catalysts synthesized. (a,d,g) HEA/g-40; (b,e,h) HEA/g-80; (c,f,i) HEA/g-120..... | 23 |
| Figure 16: SEM-EDX results for the HEA/g-40 material. (a) SEM Image of the sample. (b) EDX spectrum. (c-d) Elemental mapping of different components. | 24 |

| | |
|--|----|
| Figure 17: TEM results for the synthesized HEAs. (a,d,g,j) TEM image, interplanar distance, SAED pattern, and EDX for HEA/g-40, (b,e,h,k) HEA/g-80, and (c,f,i,l) HEA/g-120, respectively..... | 25 |
| Figure 18: XPS data measured from sample HEA/g-40. (a) Wide scan. (b-g) High-definition scan for each component. | 27 |
| Figure 19: XRD scan of the synthesized materials including peak identification. (\diamond) Graphite signals. | 30 |
| Figure 20: ATR FT-IR of the synthesized HEAs. | 31 |
| Figure 21: SEM images of the synthesized HEOs with different annealing temperatures..... | 32 |
| Figure 22: SEM-EDX elemental mapping of the HEO500 catalyst. | 33 |
| Figure 23: wide angle XRD patterns of the HEOs synthesized at different temperatures. a) Complete scan angles. b) selected angles region. The patterns used correspond to the reference patterns. Magnetite (JCPDS 96-900-6921), Tenorite (JCPDS 96-900-8962) and Zincite (JCPDS 96-900-4179)..... | 34 |
| Figure 24: a) TGA measurement of the as-synthesized HEO catalyst annealed at 300°C. b) DSC pattern obtained from the thermal scan of the HEO catalyst annealed at 300°C. | 35 |
| Figure 25: ATR FT-IR of the synthesized HEOs after the annealing process..... | 37 |
| Figure 26: High-resolution XPS measurement of HEOs synthesized with different annealing temperatures. | 39 |
| Figure 27: Entropy diagram of synthesized HEAs..... | 43 |
| Figure 28: Entropy diagram for synthesized HEOs..... | 43 |
| Figure 29: Linear sweep voltammetries of HEA electrodes with different loadings. Scan rate 1 mV/s, Na ₂ SO ₄ 0.1 M. a) cathodic direction scan. b) anodic direction scan. | 45 |
| Figure 30: Tafel plots of HEA electrodes from LSV in figure 29. a) Cathodic scan. b) Anodic scan..... | 45 |
| Figure 31: Linear sweep voltammetries of HEA/g-40 electrodes in different solutions. Scan rate 1 mV/s, Na ₂ SO ₄ 0.1 M and KOH 1.0 M. a) Vs Ag/AgCl reference electrode. b) Vs NHE (pH = 0)..... | 46 |
| Figure 32: Tafel plots for hydrogen evolution reaction of the synthesized HEAs in two different pH values. Na ₂ SO ₄ 0.1 M (pH = 5) and KOH 1.0 M (pH = 14). | 48 |

| | |
|--|----|
| Figure 33: Linear sweep voltammeteries(LSV) of the synthesized HEOs in 1.0 M KOH solution at a scan rate of 1 mV/s. a) Cathodic scan. b) Anodic scan. | 49 |
| Figure 34: Tafel plots extracted from the data in figure 33 of the synthesized HEOs in 1.0 M KOH solution at a scan rate of 1 mV/s. a) HER. b) OER. | 49 |
| Figure 35: Cyclic voltammeteries of HEA/g-40 electrode in Na ₂ SO ₄ a different scan rates. a) 0.1 M Na ₂ SO ₄ . b) 0.1 M Na ₂ SO ₄ + 400 μM NB | 51 |
| Figure 36: Cyclic voltammeteries of HEA/g-40 electrode in KOH a different scan rates. a) 1.0 M KOH. b) 1.0 M KOH + 400 μM NB. | 53 |
| Figure 37: Cyclic voltammeteries obtained for the different HEO electrodes at a scan rate of 50 mV/s. a) in 1.0 M KOH. b) in 1.0 M KOH + 400 μM NB. | 55 |
| Figure 38: EIS measurements (Nyquist plot) of the HEA/g-40 electrode at different applied potentials. a) in 0.1 M Na ₂ SO ₄ . b) in 0.1 M Na ₂ SO ₄ + 400 μM NB | 57 |
| Figure 39: R _{ct} and C _p parameters extracted from the EIS measurements using an R _s (R _{ct} C _p) equivalent circuit. a) in 0.1 M Na ₂ SO ₄ . b) in 0.1 M Na ₂ SO ₄ + 400 μM NB. | 58 |
| Figure 40: EIS measurements (Nyquist plot) of the HEA/g-40 electrode at different applied potentials. a) in 1.0 M KOH. b) in 1.0 M KOH + 400 μM NB. | 59 |
| Figure 41: R _{ct} and C _p parameters extracted from the EIS measurements using an R _s (R _{ct} C _p) equivalent circuit. a) in 1.0 M KOH. b) in 1.0 M KOH + 400 μM NB. | 60 |
| Figure 42: Impedance results for HEOs sintered at different temperatures measured in 1.0 M KOH (a), (c), and 1.0 M KOH + 400 μM NB (b), (d). Symbol (experimental data), continuous line (numerical fitting) using equivalent circuits (e) and (f). | 61 |
| Figure 43: Concentrations of (a) nitrobenzene and (b) aniline measured during the hydrogenation process in 0.1 M Na ₂ SO ₄ solution at different applied potentials. (c) Conversion and selectivity (towards aniline) at different applied potentials. (d) Aniline production rate as a function of time at different applied potentials. | 65 |
| Figure 44: Comparison of results obtained in different media at E _{app} = -1.0 V. (a) Aniline (AN) production and nitrobenzene (NB) conversion rates. (b) NB conversion and AN selectivity. (pH 5 in case of Na ₂ SO ₄ and pH 14 for KOH) | 66 |
| Figure 45: (a) First-order adjustment for the conversion of nitrobenzene. (b) the concentration of aniline vs time. (c) Current density during the hydrogenation reaction. | 67 |
| Figure 46: Productivity of nitrobenzene hydrogenation using different HEOs catalysts at (a) -1.0 V and (b) -1.4 V. | 69 |

| | |
|--|----|
| Figure 47: Correlation between resistance to the NB reduction (R_{NB}) and the pseudo-first-order reaction constant for the nitrobenzene hydrogenation at $E_{app} = -1.4V$ (vs Ag/AgCl) in 1M KOH + 400 μ M NB..... | 70 |
| Figure 48: Correlation between the aniline selectivity (%), the ratio of surface concentration of H and NB (Q_H/Q_{NB}), and the crystallite size of the different catalysts. | 72 |
| Figure 49: Nitrobenzene conversion at different applied potentials for a separate cell setup in a 1M KOH solution. | 73 |
| Figure 50: NB conversion vs type of cell setup used for the degradation experiments. | 74 |
| Figure 51: Conversion rate Vs applied potential for the different experimental setups used. a) 1.3 V. b) 1.5 V. c) 1.7 V. d) Charge efficiency of the hydrogenation process in different conditions. | 76 |
| Figure 52: Nitrobenzene and aniline concentration profiles as a function of hydrogenation time in the different experimental setups used. a) Separate cells. b) Single-cell N_2 saturated. c) Single-cell Air saturated E_{app} : 1.7 V vs Ag/AgCl in 1.0 M KOH..... | 77 |
| Figure 53: a) Nitrobenzene conversion as a function of initial concentration. b) NB degradation rate at different initial concentrations. | 78 |
| Figure 54: Stability tests of HEO500 electrode in 1.0 M KOH + 400 μ M NB at -1.4 V Vs Ag/AgCl. a) Conversion. b) selectivity. c) Faradaic Efficiency. d) Electrode current density during hydrogenation. e) transient current density pre hydrogenation. | 79 |
| Figure 55: Open circuit potential decay after the applied potential for 200 s in a 1.0 M KOH + 400 μ M NB solution. a) HEO500 electrode. b) HEO1000 electrode. | 81 |
| Figure 56: XPS wide scan measurement of a) fresh and b) used HEO500 electrode after the 5 th stability experiment. | 83 |
| Figure 57: SEM-EDX images measure from the HEO500 electrode a) before the stability tests. b) after the stability tests. | 83 |

CHAPTER I:

INTRODUCTION

The last two decades have seen a fast-paced increase in environmental-related research, going from approximately 44.000 documents published in the year 2000, with the keyword “Environment”, to over 250.000 publications in 2021. This increase in the number of published research can be directly correlated with the objectives of most grant and funding institutions, which is also in line with the global program known as the UN’s 2030 agenda and the global impact reduction expectations[1].

This increased concern in environmental-related topics has led to the re-evaluation of many industrial processes, especially catalytic processes[2,3]. The use of earth-scarce and expensive elements like Pt, Pd, Ir, Rh, or Ru is falling on a second plane, and the focus of new catalysts has been drawn to non-precious metal catalysts, based on abundant elements like Fe, Ni, Co, Cu or Ti, among others[4–6]. Another focal point in the catalyst recent research is placed in the development and use of non-metal catalysts, based on carbon-modified structures. The combination of low-cost materials and innovative nanostructures has been the inspiration of many researchers to develop increasingly efficient materials like graphene-derived materials[7,8], carbon nanotubes[9,10], metal-organic frameworks (MOF)[11,12], and carbon-supported catalysts[13,14]. In the same sense, using adequate catalytic parameters to evaluate new materials, like intrinsic activity, has led to the design of material-efficient structures like the single-atom catalysts[15], or high entropy materials[16,17], where the active amount of active element required is reduced. Most of these novel technologies are still in the early phases of research but outstanding results have been reported so far, which creates a synergistic effect on the amount of research produced, leading to the exponentially fast development of new technologies.

These new catalytic materials were rapidly adopted by the electrocatalytic research community, leading to a well-defined field of application for each type. Carbon-based materials like graphitic carbon nitrides, carbon nanotubes, and carbon nano-shells,

used either as catalytic materials or as conductive substrates, found applications in reduction or hydrogenation processes[8,18–21]. The high conductivity of the carbon substrates makes them excellent candidates for hydrogenation reactions. In this regard, reactions like the hydrogen evolution reaction (HER)[22] or the nitrobenzene hydrogenation to aniline[9], an added-value product, have attracted considerable attention in recent years. The major drawback of these catalysts is that the carbon substrates, or catalysts, are not well suited for oxidation reactions because of the low resistance to oxidation of the carbon materials, leading to fast deactivation or degradation of the electrodes.

For the oxidation reaction, metal oxides are the preferred options because these materials have higher stability in oxidative environments[23–25]. The single atom catalysts, of high entropy oxides (HEOs), have shown remarkably good activities for reactions involving extensive oxidation like the oxygen evolution reaction (OER)[12,26,27] or oxygen reduction reaction (ORR)[28,29], or in some cases extensive mineralization of different pollutants. High entropy materials (HEMs) are a relatively new type of compound [30] which includes high entropy alloys (HEAs)[31], high entropy oxides (HEOs)[32], high entropy sulfides (HESs)[33,34], and high entropy phosphides (HEPs)[35,36], among others. This class of materials has many different properties that make them suitable catalysts for a wide range of catalytic reactions, especially when different reactions must take place simultaneously or several intermediates are involved in the reactions. One of the major advantages of these materials is their increased stability due to an increase in the entropy of the solid mix reducing the mobility of atoms and slowing down possible rearrangements in the nanostructures[37].

The hydrogenation of nitrobenzene, and nitroarenes in general, presents great interest to the chemical industry. Nitrobenzene by itself has few applications, but aniline (the principal hydrogenation product) is used as the main precursor in a variety of industries, thus increasing its value considerably. The current processes for aniline hydrogenation involve the use of large amounts of reactants and very demanding conditions to achieve good results, these conditions are not environmentally friendly or energy efficient[3,38]. Electrocatalytic hydrogenation can be effectively achieved

in aqueous media at room temperature and with relatively small energy input. The main problem with nitrobenzene hydrogenation is the complicated mechanism involved and the possible intermediates that can reduce the selectivity of the process[39]. One of the major problems of the nitrobenzene industry is the amount of wastewater produced, combined with the intrinsic toxicity of nitrobenzene and its derivatives, which have created serious environmental hazards. In this regard, the selective hydrogenation of nitrobenzene presents an option for solving this problem. Another complication of the nitrobenzene industry is that the direct degradation of nitrobenzene is remarkably difficult because of its stability against oxidating agents, but the aniline is much more reactive and easier to oxidize leading to mineralization[40–42]. This approach has been used with outstanding results leading to the development of single-step degradation processes with low energy input requirements.

In this work a series of high entropy materials (HEMs) were prepared using rationally selected elements, Cu for its capacity to strongly adsorb hydrogen and make it available for hydrogenation reactions [43], Zn for the ability to adsorb anions and reduce the hydrogen evolution reaction [44], Ni and Co because of their high activity toward reducing protons and producing hydrogen adsorbed species in alkaline media [45], and Fe because of its well-known capacity to adsorb oxygen species, which improves the activity in alkaline media and improves the oxygen reduction reaction [46]. This combination of catalytic properties of each metal, mixed with their electronic and atomic similarities, covers all the properties required, theoretically, to achieve good hydrogenation results. The catalysts were carefully characterized, and their catalytic performance was evaluated using kinetic and thermodynamic parameters to determine the optimal reaction conditions, as well as the possible causes controlling the activity of each material. A correlation between the surface concentration of hydrogen and the catalyst selectivity was found, and the electron transfer rate was the controlling parameter for the overall nitrobenzene conversion, this was also dependent on the surface concentration of nitrobenzene.

The effect of nitrobenzene hydrogenation was evaluated on the degradation of nitrobenzene with possible wastewater treatment applications, and the superoxide

radical (O_2^{*-}) was found to have a strong effect on the degradation process. Demonstrating how the reduction reactions control the mineralization process.

1.1 Objective

Synthesize efficient high entropy materials (HEMs) for the electrocatalytic nitrobenzene hydrogenation with non-noble metals to improve the conversion selectivity and catalyst stability.

1.2 Scope of the Research

- Evaluate the effect of applied potential (0.0 to -2.0 V) on the hydrogenation of nitrobenzene using High entropy materials and high entropy oxides.
- Study the effects of pH on the hydrogenation of nitrobenzene over high entropy alloys, pH= 5 and 14
- Measure the effect of the High entropy alloy loading (5, 10, 20% w/w) on the electrochemical behavior for hydrogen evolution.
- Establish a correlation between the composition, structure, and physical and electrochemical properties of the High entropy oxides and the nitrobenzene hydrogenation performance.
- Evaluate the effect of the hydrogenation process on the degradation of nitrobenzene.
- Evaluate the possible mechanisms for catalysts deactivation.

CHAPTER II:

BACKGROUND AND LITERATURE REVIEW

2.1 Nitrobenzene uses and hazards

Nitrobenzene (NB) (Figure 1) is an organic compound with an aromatic ring and a nitro functional group, with a chemical formula $C_6H_5NO_2$. It is a yellow oily liquid (25 °C), with an almond-like smell, a boiling point of 211 °C, and moderately soluble in water (1.9 g/l at 20 °C). Nitrobenzene has a moderate explosion hazard when exposed to flames and presents the risk of explosion when in contact with solid or concentrated alkali[47]

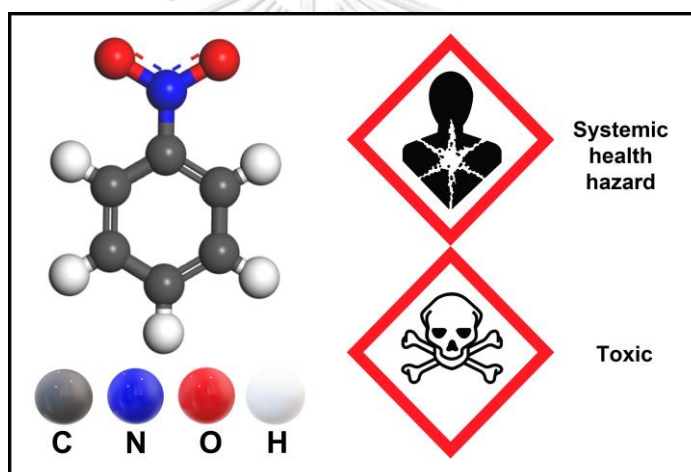


Figure 1: Nitrobenzene structure and GHS hazard classification

Nitrobenzene has been categorized as a health risk for humans and the environment by several international agencies[47]. The principal symptoms of nitrobenzene poisoning are central cyanosis, low blood oxygen saturation, metabolic acidosis, methemoglobinemia, respiratory failure, and death[48]. The lethal oral dose ranges between 1 and 5 grams and is rapidly absorbed through the skin. The OSHA exposure ceiling limit of 2 ppm. Therefore, reducing its concentration in industrial effluents and water reservoirs has been a top priority for environmental organizations and researchers[42,49–53]

2.2 Nitrobenzene and Aniline industry

The principal use of nitrobenzene is the production of aniline, which has a much higher value as a precursor for several industrial processes. Aniline is one of the principal compounds used in the manufacture of dyes, resins, varnishes, perfumes, pigments, herbicides, fungicides, explosives, isocyanates, hydroquinones, and rubber chemicals (Figure 2). Aniline is also categorized as a toxic compound by several international organizations[47].

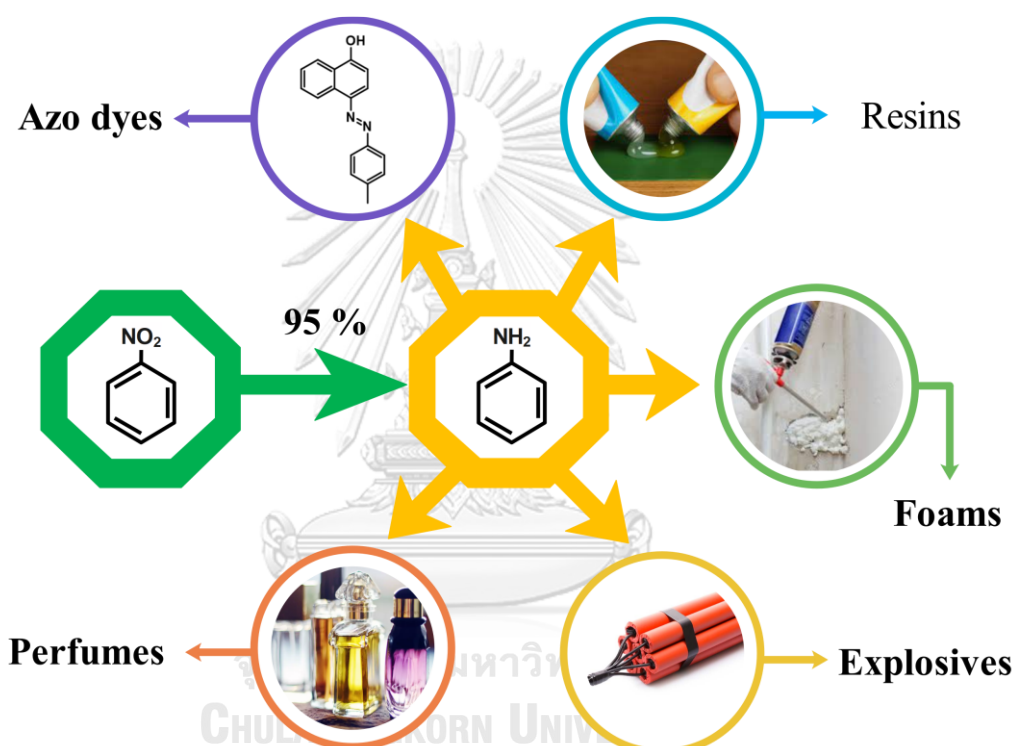


Figure 2: Different products derived from the aniline production

Nitrobenzene is a highly toxic, carcinogenic, and difficult-to-degrade contaminant compound. NB has been reported to be one of the main contaminants in industrial waste due to its extensive use, mainly for the production of aniline. [40,54,55]. Worldwide nitrobenzene consumption is closely related to aniline use. The extended use of nitrobenzene and its toxicity led many countries to establish strict regulations regarding the maximum accepted level in working spaces since the early 90's [47].

2.3 Nitroarenes hydrogenation

The catalytic hydrogenation of nitroarenes has shown to be an important process in the chemical industry. Currently, most of the amines' production industrial processes are non-catalytic and involve the use of stoichiometric quantities of reducing agents. These kinds of processes normally involve a serious environmental impact and are subject to relatively low selectivity, especially with poly-substituted nitroarenes. One of the most used methods to substitute the non-catalytic processes involve the use of Pt catalysts, high temperatures, and high pressures of hydrogen. The catalytic thermal conversion of nitrobenzene has proven to be very efficient when it comes to extensive hydrogenation, but the selectivity problem remains, especially when the catalysts used involve noble metals like Pt, Pd, Rh, or Ru. In 2007 Corma et. al.[56,57] presented a different approach to the selectivity problem. Using gold nanoparticles supported on titanium dioxide (Au/TiO₂) they reported how the support material can modify the interaction between the nitrobenzene and the Au active site, causing the reaction to follow a different pathway and increasing the selectivity consequently. Although these results provided important insights into the hydrogenation mechanism of nitroarenes, the use of gold strongly limits the application of this kind of catalyst. Later in 2013, Beller's group reported the use of earth-abundant non-noble-metal catalysts supported in carbon materials, with outstanding results for the selective hydrogenation of multiple nitroarenes[58,59]. Their approach was based on the ability to carefully control the molecular structure of homogeneous catalysts and use these modified structures, supported on appropriate materials, to control the activity of the catalysts. They also reported enhanced stability of the catalysts, even in the presence of water steam.

Another interesting approach seen in the literature is the use of different hydrogen donors to tune the selectivity of the process, the use of high-pressure hydrogen involves high costs, high temperatures to activate the H₂ molecule, and serious explosion hazards. In this regard, the use of different species like hydrazine, formic acid, or different alcohols has attracted considerable attention with good results[12,60].

The relatively demanding conditions required for the nitroarenes hydrogenation process led many researchers to evaluate different approaches which did not require high temperatures or high gas pressures. Photocatalysis and electrocatalysis have gained strong momentum in the research community since they offer lower initial investment costs, lower energy input for the reaction, and can operate at room temperature. These advantages are also balanced out by the loss of selectivity, especially when the reaction is carried out in liquid media[61].

The most commonly accepted mechanism for nitrobenzene hydrogenation is the one based on the electrochemical model proposed by Haber[62] (Figure 3). In this mechanism there are two possible ways to produce the amine; the first pathway involves the sequential reduction of the nitrobenzene with two intermediates involved, nitrosobenzene and N-hydroxylamine, before the formation of aniline. The second pathway involves the condensation of the two intermediates to produce the *Azoxy* compound, followed by three more hydrogenation steps to finally produce aniline. This second route has been reported to be relevant only in the presence of strong bases.

Later in 1992, Makaryan et. al.[63] reported the hydrogenation of nitrobenzene on noble metal catalysts (Pt, Pd, Ir), in the reaction conditions used they observed a zero-order reaction kinetics with the concentration of nitrobenzene, and they concluded that all the active sites of the catalysts must have been occupied and the simultaneous hydrogenation of several byproducts would be unlikely. While changing the partial pressure on hydrogen in the system they also observed an increase in the nitrobenzene conversion kinetics, but the N-hydroxylamine conversion remained unchanged. These results led them to propose an alternate mechanism (Figure 4) where the aniline production is the result of the disproportionation of two N-hydroxylamine species, leading to an equilibrium with the *nitroso* intermediate.

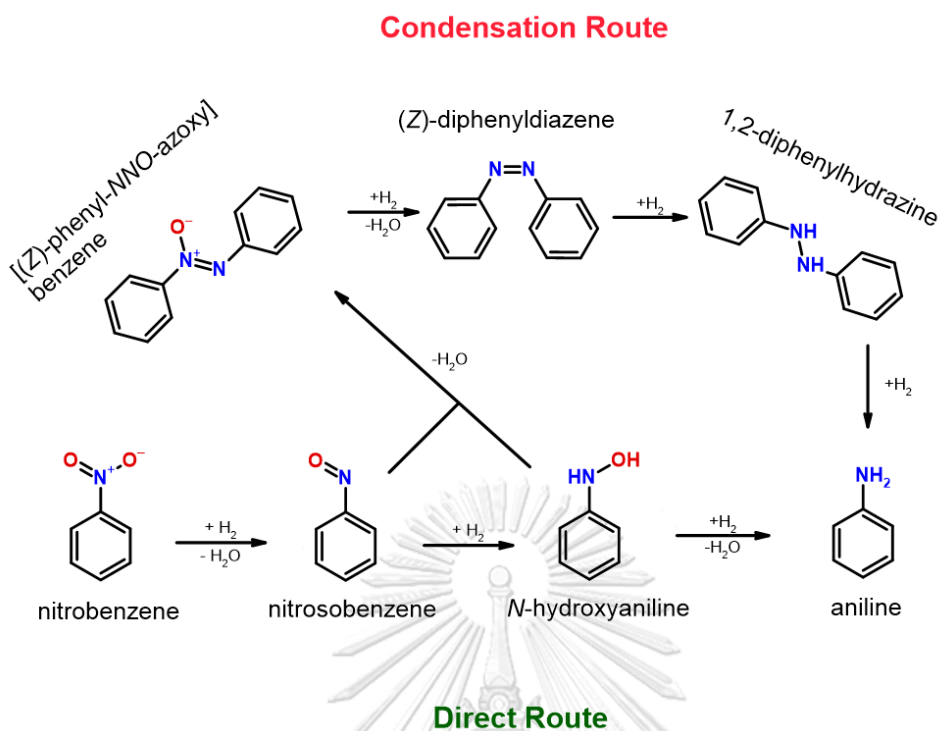


Figure 3: Haber mechanism for nitrobenzene hydrogenation mechanism

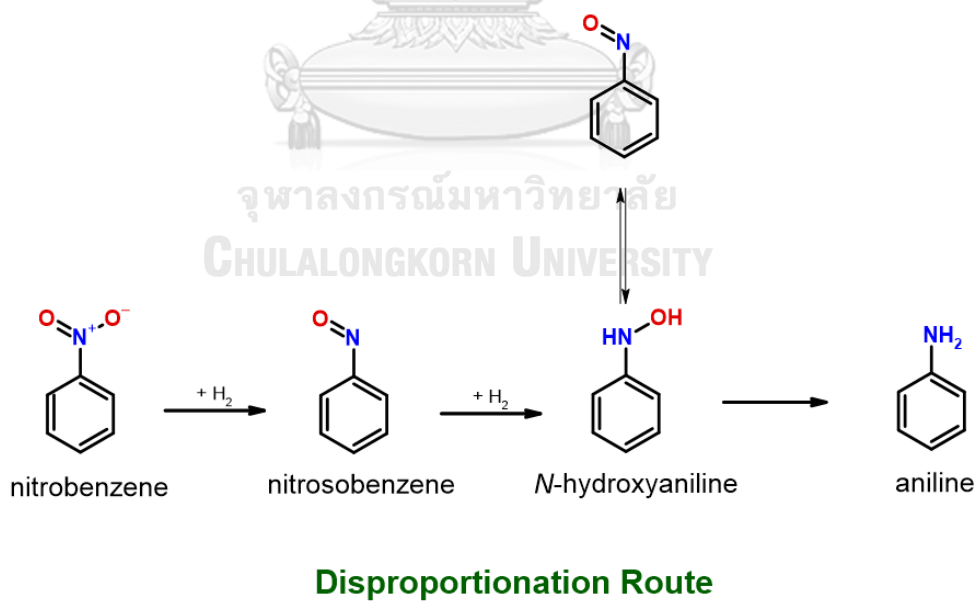


Figure 4: Nitrobenzene hydrogenation mechanism proposed by Makaryan and Savchenko[63].

In 2006 Visentin et al.[38] reported a new mechanism based on the findings of Makryan. In their work, Visentin used FTIR-ATR to evaluate the surface adsorption of different intermediates during the hydrogenation process over Pt/C catalysts. They combined the results of FTIR-ATR and hydrogen uptake to propose a direct hydrogenation pathway, where the *nitroso* intermediate is not produced and the hydrogenation goes directly from the nitrobenzene to the N-hydroxylamine, followed by a final hydrogenation step to produce aniline, as seen in Figure 5. In this mechanism, the accumulation of N-hydroxylamine was used as evidence to validate this last hydrogenation step as the rate-limiting step.

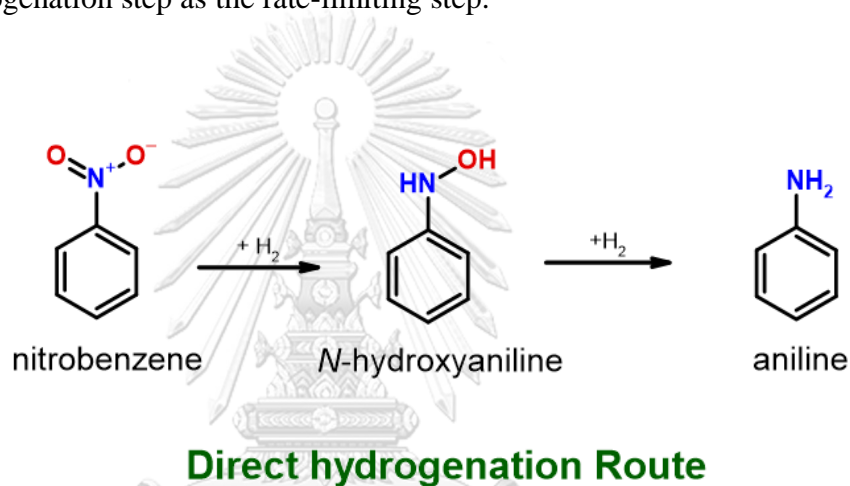


Figure 5: Nitrobenzene direct hydrogenation mechanism proposed by Visentin et al.[38].

In 2007 Corma et al.[56] proposed a mechanism for the hydrogenation of nitrobenzene based on the works of Makaryan and Visentin. Corma reported high selectivity values from the hydrogenation of nitrobenzene over Au/TiO₂, they concluded that the strong adsorption of nitrobenzene on the TiO₂ could regulate the hydrogenation mechanism and promote the direct hydrogenation from the *nitro* to the *hydroxy* compound. They based their conclusions on the low concentrations of the *azo* intermediate obtained and they also showed that the hydrogenation of the N-Hydroxylamine was the rate-limiting step (Figure 6).

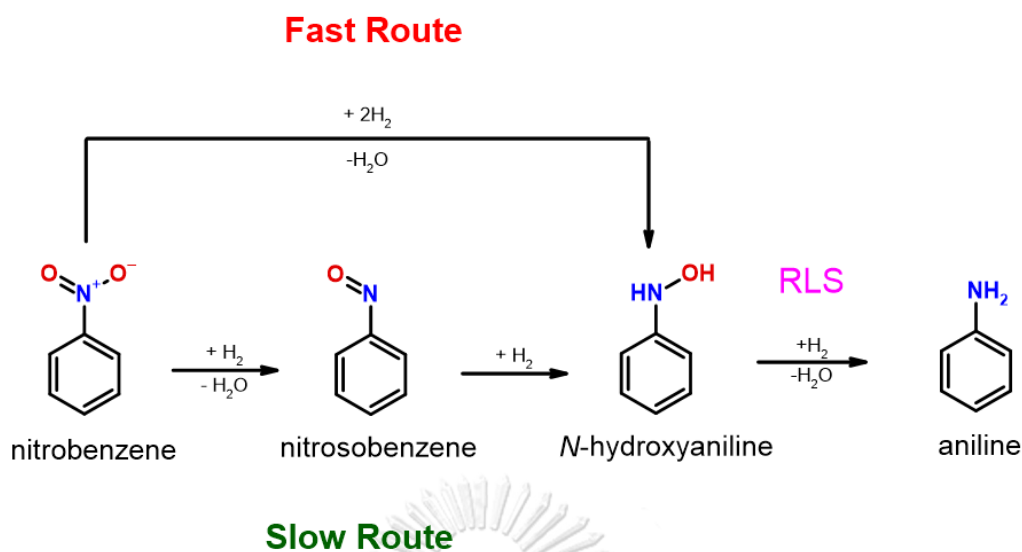


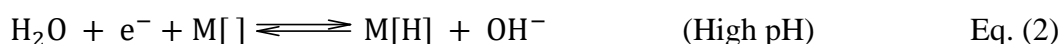
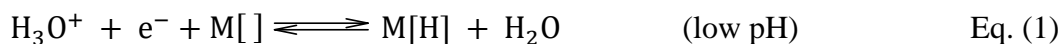
Figure 6: Nitrobenzene hydrogenation mechanism with different possible pathways[56].

2.3.1 Nitrobenzene electrocatalytic hydrogenation

2.3.1.1 Hydrogen evolution reaction

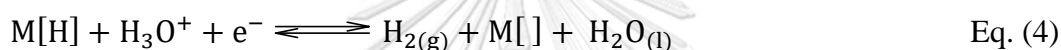
The electrocatalytic hydrogenation processes usually involve the Hydrogen Evolution Reaction (HER) as a first step to produce the hydrogen required for the reaction to take place, but it can also be a competitive pathway reducing the Faradic efficiency of the processes and affecting the selectivity of the reaction.

The electrochemical HER has been widely studied in acid and alkaline media. The commonly accepted mechanisms Volmer-Tafel [64,65] and Volmer-Heyrovsky [64,66] involve a series of chemical and electrochemical steps, which are normally used to characterize the catalytic behavior of different electrodes. The first step is usually described by the Volmer reaction, which involves the adsorption of the precursor species and depends on the pH of the solution, according to Eq. 1 and Eq. 2:



where $M[]$ represents an adsorption site on the electrode surface.

Once the Volmer reaction takes place, the adsorbed hydrogen species $M[H]$ (or $-H$) are the precursors of the gaseous hydrogen (H_2). In this regard, two mechanisms can occur simultaneously, i.e., the Tafel reaction, a chemical step where two adsorbed species recombine to produce H_2 (Eq. 3), and the Heyrovsky mechanism, an electrochemical step involving the concerted interaction between an adsorbed atom of hydrogen, another proton (or water molecule), and the transfer of a second electron (Eq. 4):



The combination of Eqs. 2 - 3 and Eqs. 2 - 4 are known as the Volmer-Tafel and Volmer-Heyrovsky mechanisms, respectively. These reactions have been widely studied on ideal surfaces (Pt, Pd) and many other surfaces including heterostructures and mixed materials [67,68], and provide useful information regarding the mechanisms or possible pathways followed during the HER or the hydrogen transfer reactions (HTR).

จุฬาลงกรณ์มหาวิทยาลัย
CHULALONGKORN UNIVERSITY

2.3.1.2 Hydrogen transfer reaction

As mentioned previously, the water reduction reaction (Eq. 2) is necessary to produce the reactive hydrogen species (H^*) on the surface of the catalysts. This first reaction will create an adsorption competition with the desired product to hydrogenate. Since Eq. 2 involves an electron transfer, the formation of adsorbed hydrogen can be regulated by the applied potential. Therefore, it is fundamental to properly control the applied potential to optimize the hydrogenation conditions.

On the other hand, the applied potential also has a very strong influence on the adsorption of the target species. It has been widely studied how the applied potential can affect the adsorption of different species leading to deviations from the predicted adsorption energies, therefore the traditional molecular simulations fail to correctly predict the real behavior of different electrochemical systems. In this regard, Norskov's group has pioneered the field of simulation of charged surfaces providing valuable theoretical insights into the properties of charged interphases[69,70]. Another important parameter for electrochemical reactions is the redox potential, which is determined by the Nernst equation (Eq. 5)

$$E_{red-ox} = E^0 - \frac{RT}{nF} \ln(Q) \quad \text{Eq.(5)}$$

Where E_{red-ox} is the observed reduction potential, E^0 is the standard reduction potential, R , T , n , F , and Q are the gases constant, temperature, number of electrons transferred, the Faraday constant and the chemical equilibrium respectively. The determination of standard potentials is normally only possible when adsorption steps are involved because the interactions vary with the substrate and the solvent.

The thermodynamic properties, like adsorption energies and formal reduction potentials, are strongly related to the kinetic behavior and catalytic performance of different materials. Extensive studies have reported on the electrochemical hydrogen evolution reaction, nitrogen reduction reaction, and oxygen evolution reaction, and most of them can be summarized in what is known as volcano plots, where the electrochemical activity, normally denoted as current density (j), presents a correlation with the adsorption energy[71].

All these parameters must be considered when working on electrochemical hydrogenation because the competition between different electroactive species can modify the electrochemical equilibrium conditions and subsequently deviate the experimental results from the theoretical ones. Following these premises, several research groups have found interesting correlations between the surface concentrations of different species[72,73]. In general, when the surface concentration of hydrogen on the electrocatalyst (electrode) is relatively low compared to the concentration of the target molecule, the conversions are typically high since most of

the active sites can be occupied and the reaction rate is increased. This increase in the kinetics of the reaction oftentimes causes a sharp decrease in selectivity, especially when there is an intermediate with strong adsorption, or the conversion is the rate-limiting step (RLS).

On the contrary, when the surface concentration of active hydrogen is high, compared to the concentration of the studied molecule, the conversions are typically lower, but the conversion is higher, especially for extensively hydrogenated molecules [72,73]. A simplified summary of the competitive adsorption and its effect on selective hydrogenation is shown in Figure 7.

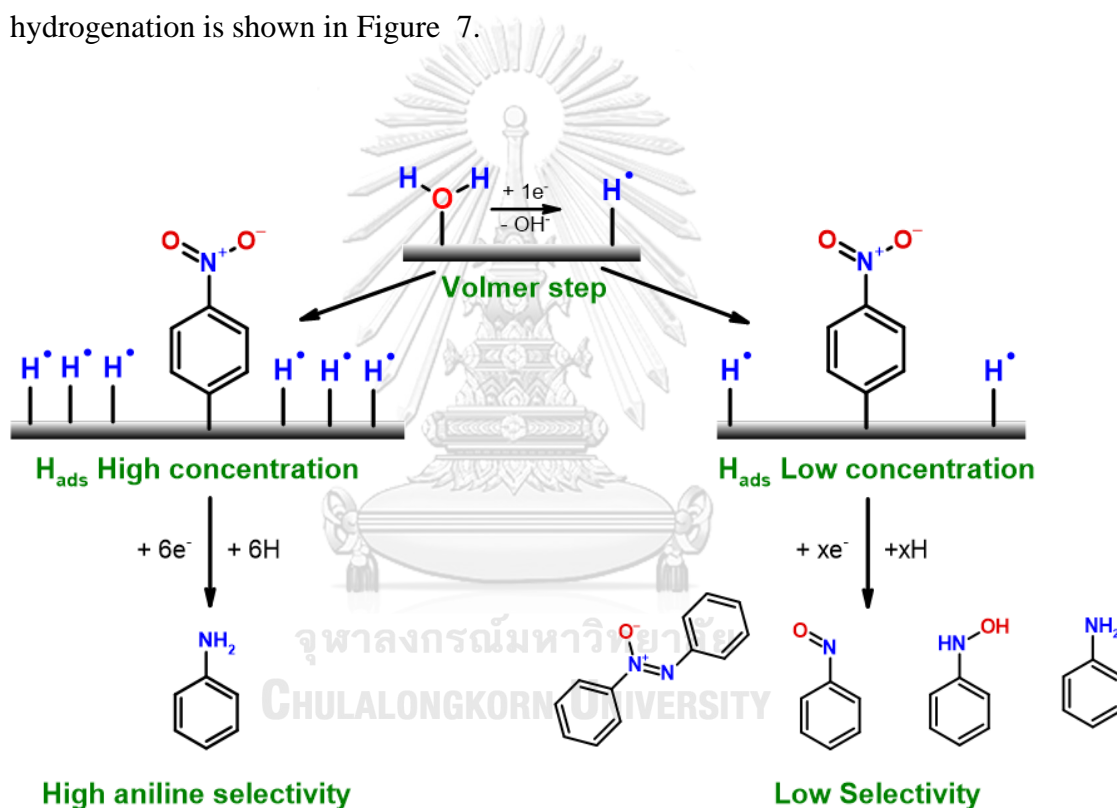


Figure 7: Scheme for selective catalytic hydrogenation of nitrobenzene mediated by the adsorbed hydrogen.

2.4 Nitrobenzene degradation

As mentioned previously, nitrobenzene is a health hazard, but also a serious environmental hazard, its aromatic ring makes it extremely difficult to naturally degrade and is considered a recalcitrant contaminant. The traditional approach to

direct degradation via oxidant radicals like OH^* or O_2^{*-} has shown good results, but extensive degradation and complete mineralization results are still elusive. Different approaches aiming to increase the rate of production of these oxidant radicals either by using new catalysts or by adding peroxides have been extensively reported in the last years. Another approach has been the use of more aggressive radicals like the sulfate radical (SO_4^{*-}), which has a higher oxidation capacity than the OH^* radical, but the energy required to produce it is considerably high and its lifetime is extremely short, thus requiring the use of sacrificial agents to produce it in the homogeneous medium to achieve good oxidation results[41].

Considering the stability of nitrobenzene towards oxidation, but its good reactivity towards hydrogenation, several reports have shown the efficient degradation of nitrobenzene through a two-step process. First extensive hydrogenation of nitrobenzene to aniline (or any partially hydrogenated by-product), followed by a radical attack on the aniline, which is much more susceptible to being oxidized, leading to the opening of the ring and subsequent degradation and mineralization[74,75] as shown in Figure 8.

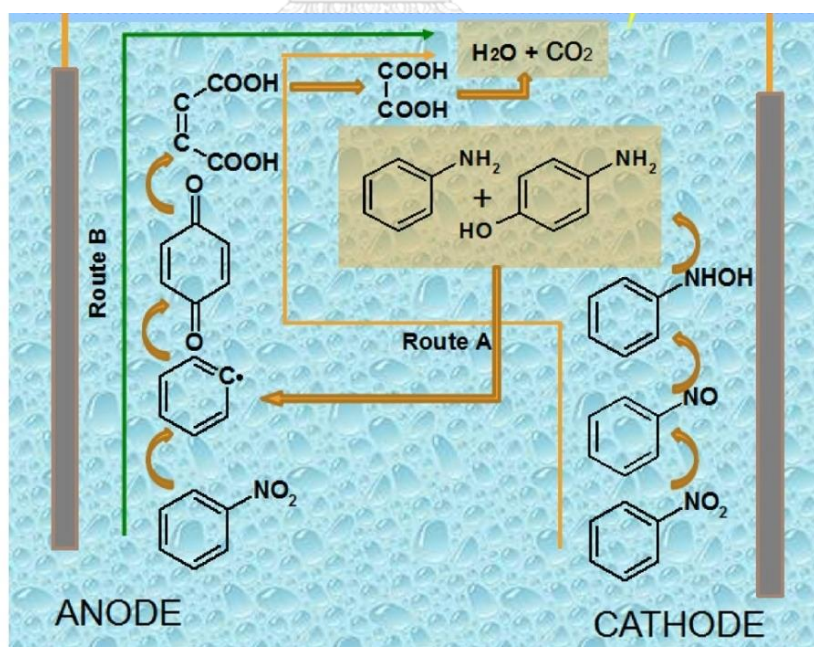


Figure 8: Schematic representation of the nitrobenzene degradation promoted by the hydrogenation step[75].

2.5 High entropy materials (HEMs)

The complexity of the different proposed mechanisms for selective hydrogenation mechanisms, which involve several intermediates, has raised several concerns regarding the use of traditional catalysts. The traditional approach to heterogeneous catalysis involves the presence of a unique type of active site, normally responsible for all the interactions and reactivity and the effect of some promoters or substrates on the activity of the active site. This approach is efficient when the reaction involves few intermediates, or the adsorption energies are considerably different. In the case of the electrochemical hydrogenation of nitrobenzene, several active sites are required, first for the reduction of the water molecule and (at least) one more type of active site for the adsorption of the nitrobenzene. If more sites are required, traditional catalysts fail to achieve efficient catalytic behavior. Several approaches have been used to tackle this problem with relatively good results. The use of heterostructures or mixed materials for catalytic applications is a common practice found in the literature, but this approach presents the complication of properly addressing the nature of the active sites and fails to consider the effect of the boundaries between different materials, normally wrongly attributing catalytic properties to different phases. Another interesting approach used recently is the use of amorphous materials for different reactions like CO₂ reduction or the oxygen evolution reaction. The main advantage of amorphous materials lies in the presence of multiple crystallographic defects which give the catalyst a multiplicity of active sites and can provide specific energy levels for different intermediates facilitating extensive hydrogenations or oxidations [76,77].

The so-called High-Entropy materials (HEMs) have the unique property of a multitude of active sites for different reactions owing to the independent interaction of each atom [78]. Another advantage of these materials is their intrinsic conductive nature, which makes them suitable candidates for electrocatalysis and provides an effective way to control the extent of the reaction as well as the energy input required. The HEMs are defined as mixtures with a minimum of 5 elements, where all of the elements are considered the majority (> 5 at.%), ideally in equimolar compositions, causing an increase in the mixing entropy (ΔS_{mix}). This equimolar composition (e.g.

20 at.% for each element) would produce the maximum increase of stability due to the entropy effect ($\Delta S_{\text{mix}} = 1.6R$, with R being the gas constant, $R = 8.3145 \text{ J mol}^{-1} \text{ K}^{-1}$). The minimum value to classify a material as high entropy, as reported initially by Yeh et al. [17] and later by Xu et al. [79] and Zhang et al. [80], is $\Delta S_{\text{mix}} = 1.5R$, which allows a variation of the elemental composition between 5 and 35 at.% as reported by Cantor et al.[30]. One of the consequences of this effect is the increase in the overall stability of the alloy materials due to the low diffusivity of constituent atoms [78]. In a broad definition, the HEMs can have a single crystalline phase, polycrystallinity, intermetallic properties, or even phase segregation, and are still considered high entropy materials. In the same sense, some alloys or materials with single-phase structure or different principal elements can be considered solid solutions, but necessarily fall within the high entropy classification. Because of this, a new term, compositionally complex solutions (CCSS), was coined by Löffler et. al.[37] to refer to high entropy materials with solid solution structure, where the interaction between atoms is increased and the properties of the catalysts can be carefully tuned by controlling the composition.

2.5.1 High entropy alloys (HEAs)

The high entropy alloys (HEAs), specifically the CCSS, possess a variety of properties that makes them promising candidates for electrocatalytic processes. Currently, an increasing number of publications involve the use of this kind of material showing increasingly good results in different processes[16,72,81,82]. One of the advantages of the HEAs is the flexibility for finely tuning the binding energies with different reactants, controlling the composition of the catalyst directly affects the short-range and long-range interactions between the neighboring atoms, therefore modifying the overall reactivity. The “multifunctionality” is another of the main advantages of these materials; if each element is considered as a reaction site with specific binding energy, then the atoms can be grouped in different “binding peaks”, which can then be controlled to enhance or suppress specific surface reactions leading

to what's called the cascade effect (Figure 9), this can lead a better understanding and control of the catalyst selectivity[37].

Many elements can be used to prepare highly active high entropy alloys, with the advantage of replacing expensive noble-metal elements with an appropriate combination of non-noble metals with similar or even improved activity. One of the biggest advantages of the HEAs is the increased stability caused by the entropy stabilization, which can drastically decrease ion mobility and limits the surface rearrangements normally observed in electrocatalytic reactions[37]

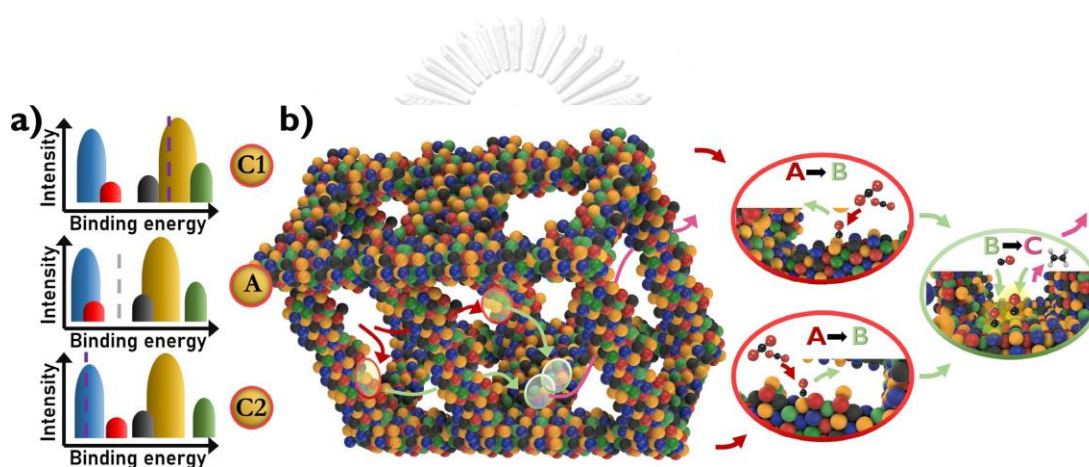


Figure 9: a) Different “binding peaks” and the effect on different surface reactions. b) Schematic representation of the “cascade effect” on a HEA[37].

2.5.2 High entropy oxides (HEOs)

The high entropy oxides or entropy stabilized oxides are a different subgroup of the high entropy materials, characterized by the incorporation of different cations in an oxide network with different possible configurations. One of the most interesting properties of the entropy-stabilized oxides is their ability to change from polycrystalline structures to single-phase materials upon heat treatment, and the reversibility of this phase transformation (single-phase to polycrystalline) only by heat treatment as seen in Figure 10. The concepts of entropy stabilization applied to the HEAs can also be applied to the high entropy oxides (HEOs) as shown by Rost et. al.[83]. The changes in configuration produced by the insertion of different atoms

(cations) in a single (or polymorphic) structure cause an increase in the number of surface defects present in the catalysts, leading to increased activities, oftentimes at the expense of stability[84–87].

An important property that differentiates the HEOs from the HEAs is the presence of oxygen vacancies, since the HEAs are composed of metallic atoms, the defects are caused by the presence of different adjacent atoms. In the case of the HEOs, the defects in the structure can be caused by different adjacent cations, but by the oxygen defects caused by the modified structures, leading to especially active catalysts with promising activities in different processes[87,88].

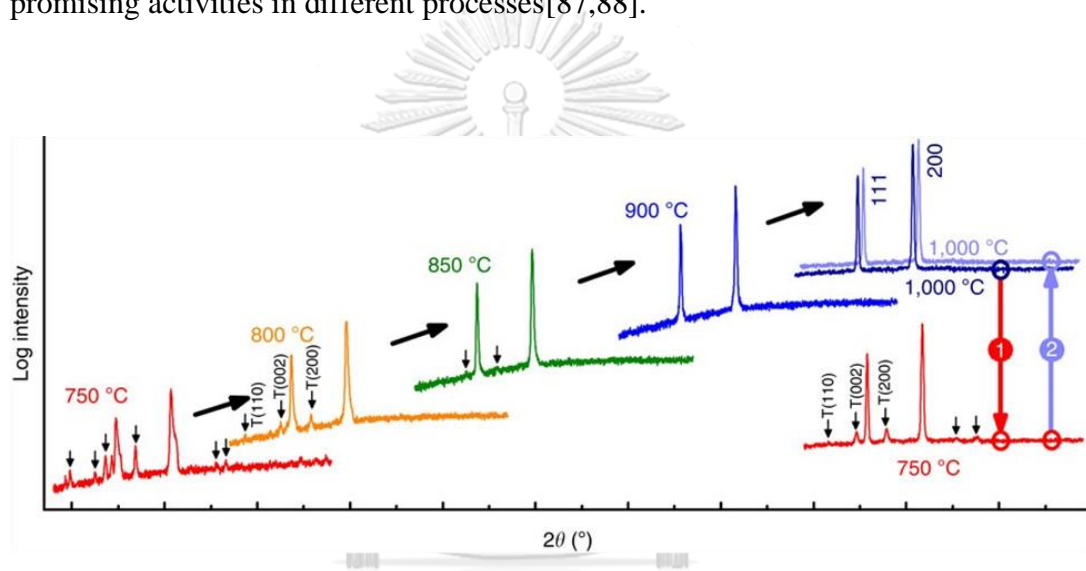


Figure 10: XRD patterns of an equimolar mixture of MgO, NiO, ZnO, CuO, and CoO treated at different temperatures. Samples stabilized for 2 hr in air atmosphere and quenched by extracting from the oven[83].

CHAPTER III: EXPERIMENTAL SECTION

3.1 Catalysts synthesis

3.1.1 HEAs synthesis

The high-entropy alloys were synthesized using an electroless deposition method. The graphite used as support was initially treated with concentrated boiling sulfuric acid (98%, Merck) for two hours, then rinsed and dried on a hot plate to evaporate the remains of sulfuric acid. A solution with a total metal concentration equal to 0.05 M, using an equimolar concentration of the precursor metals (i.e., CFe: CCo: CNi: CCu: CZn), was prepared using $\text{Fe}(\text{NO}_3)_3$, $\text{Co}(\text{NO}_3)_2$, $\text{Ni}(\text{NO}_3)_2$, $\text{Cu}(\text{NO}_3)_2$ and $\text{Zn}(\text{NO}_3)_2$ (Sigma-Aldrich, analytical grade, > 95%, used without further purification). Different ratios of metals solution volume (SM (mL)) versus the mass of graphite (g wt) (SM/g wt: 40, 80, 120 ($\text{mL}_{\text{solution}}/\text{g}_{\text{graphite}}$)) were used, to evaluate the variation in metal loading. The mixture was stirred vigorously for 24 h. After this, the remaining solid was filtered, rinsed with DI water, and dried at 110 °C for 24 h before use. The solids were stored and labeled HEA/g-x (X: 40, 80, 120) (Figure 11).

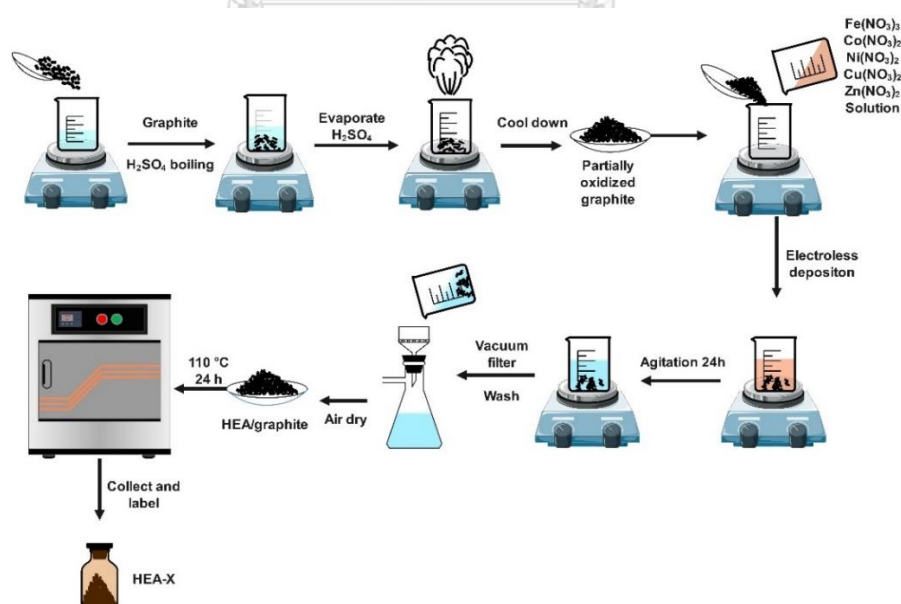


Figure 11: Schematic representation of the HEAs supported on graphite synthesis procedure.

3.1.2 HEOs synthesis

The HEOs were prepared via the urea hydrolysis method. An equimolar aqueous solution of Zn^{2+} , Cu^{2+} , Fe^{2+} , Co^{2+} , and Ni^{2+} ($0,002 \text{ mol L}^{-1}$) was prepared. Followed by the addition of urea (0.05 mol L^{-1} final concentration) and stirred for 1 h. The solution was transferred to an oven at $125 \text{ }^\circ\text{C}$ for 4 hours, then allowed to cool down to inside the oven. The precipitated solids were filtered and washed with DI water. The resulting powder was dried at $100 \text{ }^\circ\text{C}$ overnight. Afterward, the collected powder was calcinated in an air atmosphere at different temperatures ($300, 400, 500, 600, 800,$ and $1000 \text{ }^\circ\text{C}$) for 2 hr with a heating ramp of $5 \text{ }^\circ\text{C min}^{-1}$. The calcinated solids were stored and labeled HEOX (X: $300, 400, 500, 600, 800, 1000$) (Figure 12).

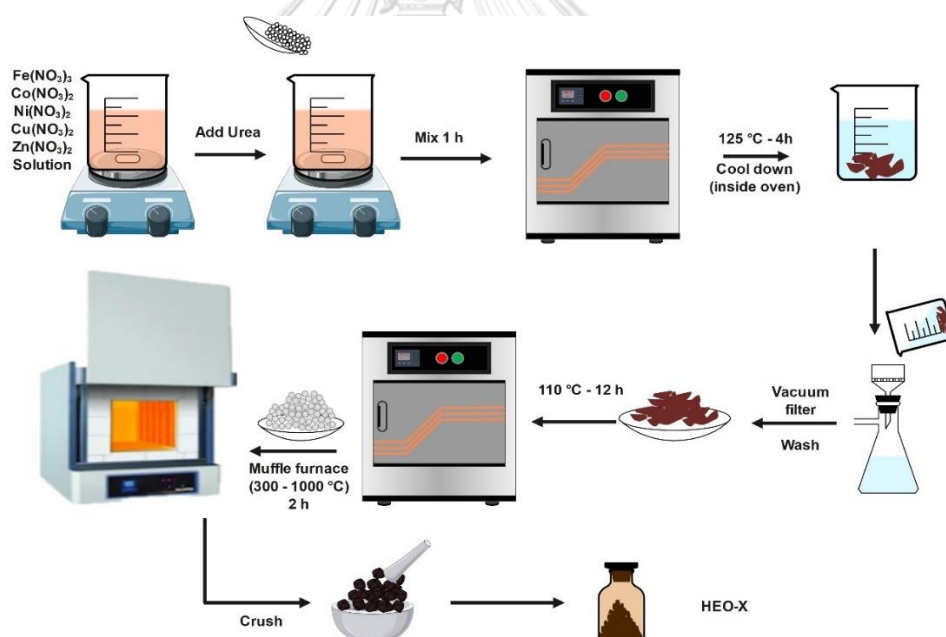


Figure 12: Schematic representation of the HEOs synthesis procedure.

3.2 Electrodes preparation

The catalyst ink was prepared by mixing 5 mg of catalyst, $50 \mu\text{L}$ of Nafion® solution 5 wt.% in short-chain alcohols (Sigma-Aldrich), $750 \mu\text{L}$ of isopropanol (Sigma-

Aldrich, > 99.5%), and 200 μL of DI water. The ink mixture was sonicated for 30 minutes at intervals of 5 minutes to ensure an appropriate mix, the mixing process was repeated 5 extra minutes before the preparation of the electrodes.

Graphite disks were polished with sandpaper #250, #400, and #600 grit, sonicated in isopropanol for 10 minutes, and in water, for 10 min to remove have a reproducible initial surface, remove remaining oil, and graphite powder. The flexible graphite foils were cleaned by sonication in isopropanol for 5 minutes, followed by water for 5 min, and repeated 3 times to clean the surface. As the last step for the surface preparation, the substrates were sonicated with isopropanol for 5 min and dried under air before adding 1 mL of HEOX ink, then was dried under air and at 80 $^{\circ}\text{C}$ in an air oven for 2 h (Figure 13). The graphite disks had a geometrical area of 0.79 cm^2 were used for hydrogenation with HEAs, graphite foils of 1 cm^2 were used for the hydrogenation tests with HEOs, and 2 cm^2 foils were used for the degradation tests as substrate.

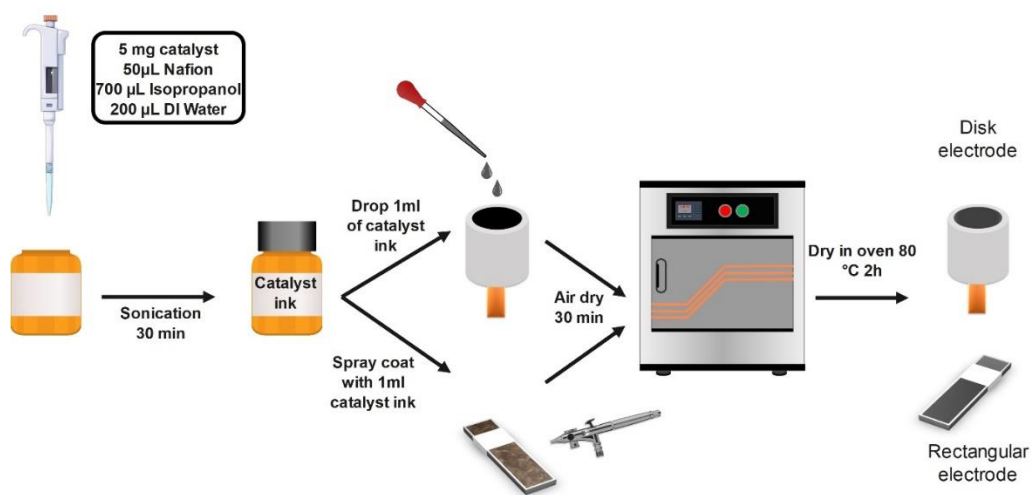


Figure 13: Schematic representation of the preparation of electrodes.

3.3 Catalysts characterization

3.3.1 SEM-EDX

Scanning Electron Microscopy (SEM) and Energy-Dispersive X-ray spectroscopy (EDX) were used to study the surface morphology of the catalysts and the relative elemental concentrations on the surface.

3.3.2 HR-TEM

High-resolution transmission electron microscopy (HR-TEM) measurements were made using a JEOL JEM-2010 equipment on a Cu grid and the EDX spectra using an Oxford X-Max 80T accessory.

3.3.3 X-ray diffraction

The crystal structure of the material was analyzed using X-ray diffraction (XRD) using the Bruker D8 Advance with the irradiation of Cu anodes and $K\alpha_1$ (1,544, a 2θ range from 10° to 80° and a scan rate of $0.02^\circ/\text{min}$.

3.3.4 X-ray photoelectron spectroscopy (XPS)

The surface of the catalysts was analyzed using X-ray photoelectron spectroscopy (XPS) with a spectrometer AMICUS with Mg $K\alpha$ X-ray radiation (1253.6 eV) and Al $K\alpha$ X-ray radiation (1486.6 eV) at a voltage of 15 kV and current of 12 mA. The binding energy value was calibrated by the C 1s peak at 2.6 eV, and the elements Fe 2s (6.398 eV), Co 2s (6.924 eV), Ni 2s (7.471 eV), Cu 2s (8.040 eV), and Zn 2s (8.630 eV), respectively.

3.3.5 Fourier transformed Infra-red (FT-IR)

The surface species and chemical bonds are analyzed by Fourier transform Infrared spectroscopy using a Nicolet 6700 FT-IR and a single point Attenuated Total Reflectance (ATR) accessory.

3.3.6 TGA and DSC

Thermogravimetric analysis (TGA) and differential scanning calorimetry (DSC) was performed using a Q600 SDT TA company, with a scan rate of $10\text{ }^{\circ}\text{C min}^{-1}$ in an air atmosphere (21% O_2 in N_2 , <15 ppm moisture, Linde).

3.3.7 Surface area measurements (BET)

The surface area, pore size, and pore volume are measured using an ASAP 2020 surface area and porosity analyzer (Micromeritics®) and adjusted to the Brunauer–Emmett–Teller (BET) isotherm.

3.3.8 Electrochemical measurements

Electrochemical experiments were performed using a potentiostat/galvanostat Autolab® PGSTAT204 equipped with a frequency response analyzer (FRA32M) module. The electrochemical impedance spectroscopy (EIS) measurements were performed using an A.C. perturbation of 10mV, in the range of 0.1 MHz to 0.1Hz at different applied potentials, and in the presence or absence of nitrobenzene. Before each electrochemical experiment, the solution was saturated with N_2 (> 99.99 %) for 30 min, and the open-circuit voltage was followed to have a reproducible and stable initial condition.

3.4 Nitrobenzene concentration measurement

The concentrations of the products, (NB and AN) were measured using a LAMBDA 650 UV/Vis spectrophotometer and a multi-peak deconvolution method to estimate the absolute concentrations.

3.5 Nitrobenzene hydrogenation

The hydrogenation of nitrobenzene was performed using an H-type cell with a solution volume of 50mL. The compartments were separated by a Nafion® 115 membrane. The counter electrode used was a platinized titanium mesh with a geometrical area of 6.25 cm². On the working electrode compartment, a solution of Na₂SO₄ (0.1 M), or KOH (1.0 M), and 400 µM concentration of nitrobenzene was used as support electrolyte under constant magnetic stirring. The solution used on the counter electrode compartment was prepared to match the concentration of the supporting electrolyte used on the working electrode compartment Na₂SO₄ (0.1 M), or KOH (1.0 M) respectively.

3.6 Nitrobenzene degradation

The degradation of nitrobenzene was also carried out in two different setups; first, an H-type cell with a solution volume of 50 mL. The conditions were similar to the hydrogenation experiments. For the single chamber experiments, the three electrodes were loaded in the same compartment, and a solution of KOH (> 85%, Univar) (1.0 M, pH 14), and different concentrations of NB (Sigma-Aldrich) were used as support electrolytes under constant magnetic stirring. The platinized titanium mesh (Anomet®) was replaced by an HEO electrode with similar dimensions to the working electrode. Figure 14 shows the different setups used for the two cell configurations.

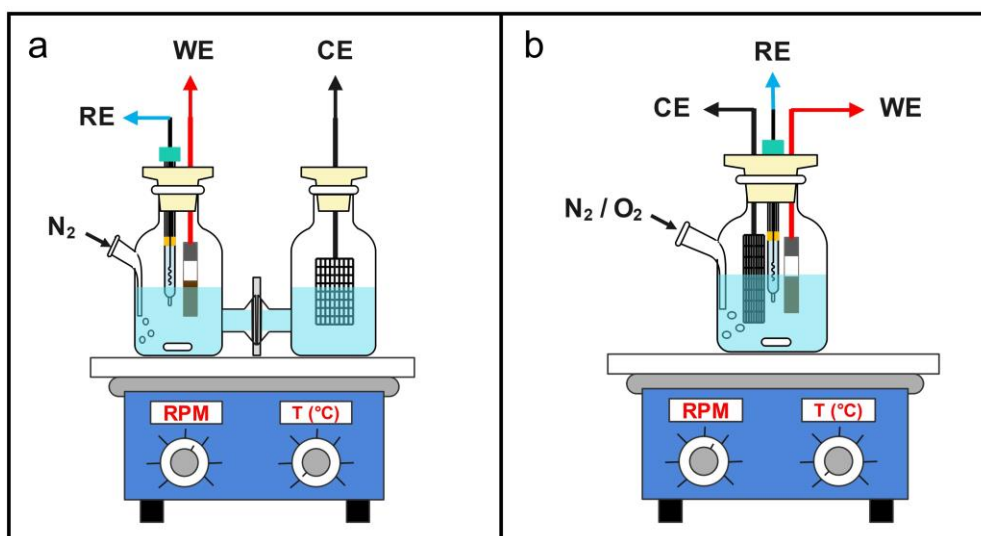


Figure 14: Schematic representation of the cell configurations used. a) separate compartments cell. b) single-compartment cell



CHAPTER IV:

RESULTS AND DISCUSSION

4.1 Catalysts physical characterization

4.1.1 High entropy alloys (HEAs)

4.1.1.1 SEM-EDX

The surface morphology of the synthesized catalysts was analyzed using SEM. Figure 15 depicts the micrographs of the material prepared with the three different compositions. The images show that all three materials exhibit similar morphology, corresponding to the laminar structure of the graphite substrate. The alloy particles were not observed due to their small size product of the low metal loading and the procedure used. The sheet-like structure of the graphite support ensures a high specific surface area available for the adsorption and homogeneous distribution of the alloy particles

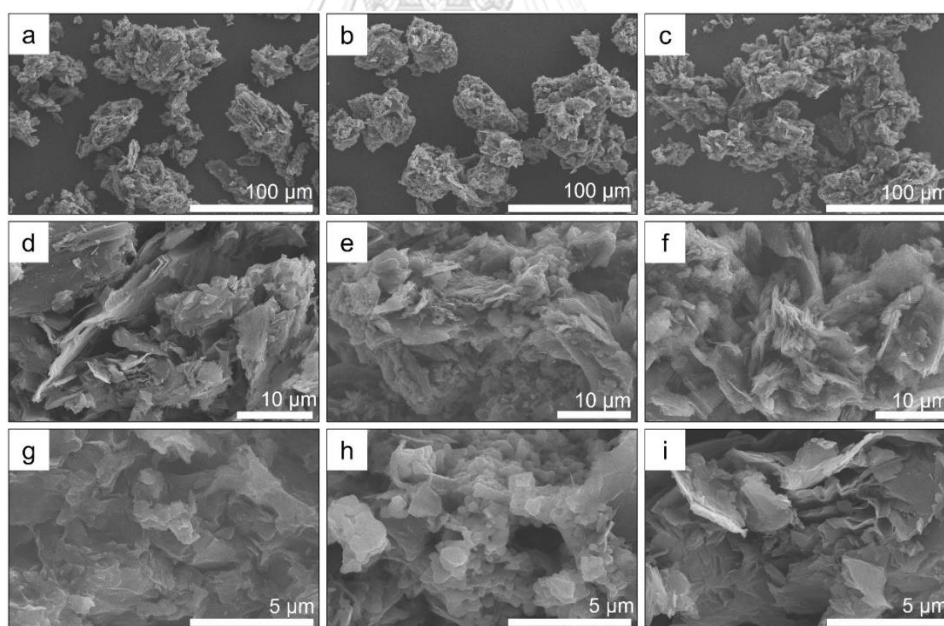


Figure 15: SEM images with different magnifications of the three catalysts synthesized. (a,d,g) HEA/g-40; (b,e,h) HEA/g-80; (c,f,i) HEA/g-120.

The distribution of the elements is shown in SEM-EDX results of the HEA materials (Figure 16), where the five elements of interest (Fe, Co, Ni, Cu, and Zn) are present on the surface of the catalysts in a fairly homogeneous distribution

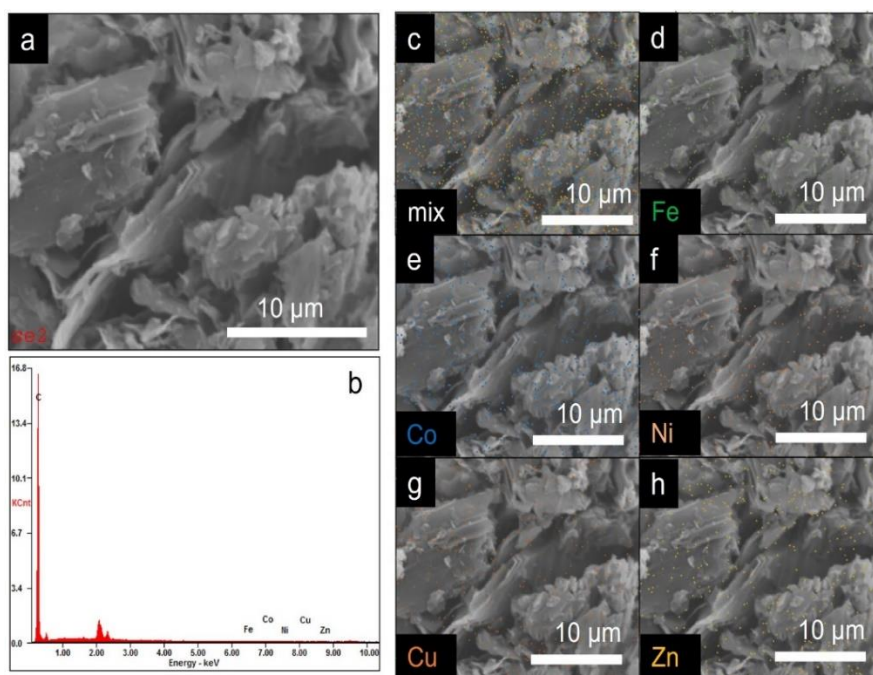


Figure 16: SEM-EDX results for the HEA/g-40 material. (a) SEM Image of the sample. (b) EDX spectrum. (c-d) Elemental mapping of different components.

4.1.1.2 HR-TEM

Figure 17 depicts the TEM results for the HEAs. It is important to remark that no clumping, individual metal clusters, or areas could be found. This implies that the probability of each metal interacting with the others is increased, and the segregation of the individual phases was avoided as shown in Figure 17a,d for the lowest metal loading (HEA/g-40), while the materials with higher metal loadings present phase segregation as seen in Figure 17b,e and Figure 17c,f for the HEA/g-80 and HEA/g-120, respectively. In Figure 2d-f, it can be seen how the interplanar distance of the films increases with the metal loading going from an average of (0.29 ± 0.03) nm in the HEA/g-40 to (0.38 ± 0.03) nm for HEA/g-80 and (0.33 ± 0.03) nm for HEA/g-120. This is most likely caused by the increase in the relative content of Zn in the

whole materials as reported by Huang et al. [89]. The difference in atomic size and crystal structure of Zn (hexagonal packed HCP) with the other elements Fe (BCC or FCC), Co (HCP), Ni (FCC), Cu (FCC), and the lack of empty orbitals on the d-level cause an increase in the structural stress, increase of interplanar distances, shifting to lower diffraction peaks' angles and a modification of the lattice constant

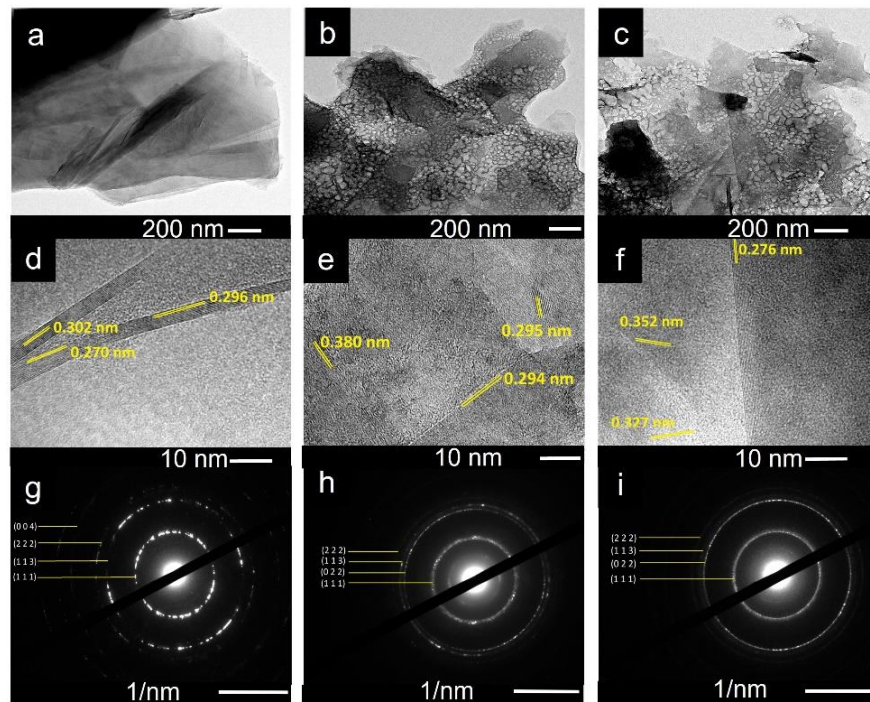


Figure 17: TEM results for the synthesized HEAs. (a,d,g,j) TEM image, interplanar distance, SAED pattern, and EDX for HEA/g-40, (b,e,h,k) HEA/g-80, and (c,f,i,l) HEA/g-120, respectively.

Additionally, the low concentration of the employed solution allowed the formation of thin films whose crystallization and growth was controlled by the thermodynamics of the process favoring the formation of single-phase multi-elemental alloys or HEAs at lower loadings and multi-phase films for the higher metal loadings [17]. This was confirmed by the selected area electron diffraction (SAED) measurements. In Figures 2g-I, the SAED patterns for the three materials correspond to a cubic structure, more specifically a magnetite-like structure ($Fd\bar{3}m$) due to the relatively high amount of iron in the sample and the oxidation of the surface. In the case of the HEA/g-40, a polycrystalline structure was observed on the SAED, while for the other two materials

the diffuse circles are evidence of amorphous characteristics. All the desired elements were detected by EDX measurements from the TEM selected area, with the relative concentrations given in

Table 1.

*Table 1: Elemental composition of the synthesized materials measured by TEM-EDX**.*

| Element | HEA/g-40 Wt.% (± 0.1) | HEA/g-80 Wt.% (± 0.1) | HEA/g-120 Wt.% (± 0.1) |
|----------------|---|---|--|
| Fe | 2.7 | 11.0 | 14.1 |
| Co | 2.7 | 9.5 | 8.6 |
| Ni | 1.2 | 6.3 | 6.9 |
| Cu | 91.8 | 65.5 | 64.0 |
| Zn | 1.6 | 7.7 | 6.4 |
| Metals | 100.0 | 100.0 | 100.0 |

**The grid used for TEM measurements was made of Cu.

4.1.1.3 XPS analysis

To further examine the surface of the catalysts, XPS analysis was performed, as shown in Figure 18 for the three different HEA/g-x materials. The wide scan shows two major edge signals, one at 280 eV corresponding to the C edge and a second one at 524 eV corresponding to the O edge. When it comes to the signals of the metals, the specific edge signals (719 eV (Fe); 790 eV (Co); 870 eV (Ni); 952 eV (Cu), and 1020 eV (Zn)) were within the noise level of the measurements and the oxidation states could not be analyzed. These results are a consequence of the low concentration of each metal on the catalyst (≈ 1 wt.%, see Table 1), the matrix effect of the sample, and possible interactions between elements that can cause the loss in the detection sensitivity [90–93]. The analysis of the C signal (for example, see Fig. S4g for the HEA/g-40 material) provides useful information. It shows the main signal corresponding to the C-H bond (285 eV) caused by the exposed edges of the graphite sheets, like the functionalization of graphene sheet edges. The other three signals at

286.1 eV, 287.1 eV, and 288.3 eV are attributed to the oxygenated groups C-O, C=O, and C-OOH, respectively.

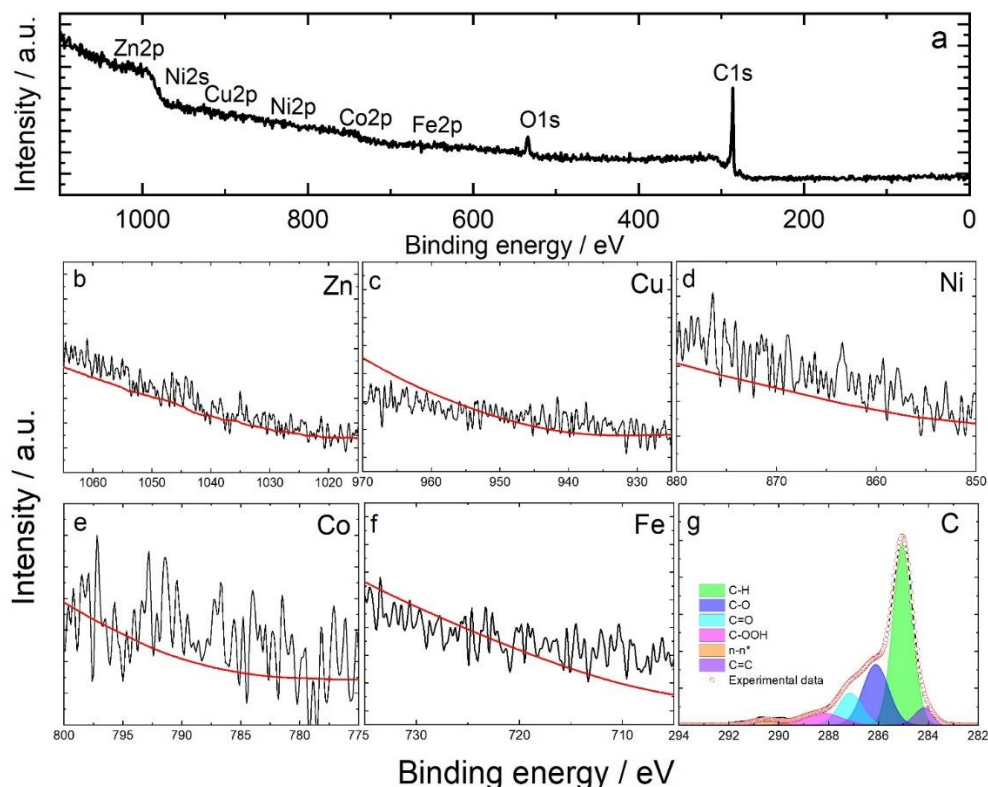


Figure 18: XPS data measured from sample HEA/g-40. (a) Wide scan. (b-g) High-definition scan for each component.

These oxygenated groups were expected as a result of the pretreatment of the graphite support before the alloys deposition, and have an important role in the electric performance of the catalysts, since these oxygenated functional groups may improve the dispersion of the substrate [94], the number of surface defects and adsorption sites [95,96], and may enhance the electrical conductivity of the laminar graphite structures [94]. The signal at 284 eV was attributed to the C=C bond in the graphite sheets. The semi-quantitative analysis obtained by XPS for the HEA/g-40 material (Table 2) showed elemental compositions in the range of 5.6-11.0 wt.%, while compositional data derived from SEM-EDX vary from 0.8 to 1.9 wt.%. The considerable difference between XPS and SEM-EDX data arises from the difference in penetration depth of each technique [90], i.e. relatively higher wt.% are obtained by XPS as a result of its smaller penetration depth. On the other hand, the E/Mt data (i.e., the ratio of each

element to the sum of all the metals) show near-equimolar compositions (~ 0.20) for each of the synthesized materials (Tables 2 to 4). This is clear evidence of the formation of high-entropy alloys as the (metallic) elemental composition falls well within the defined range of 10 to 35 at.% [59].

Table 2: Elemental composition of the synthesized HEA/g-40 material measured by SEM-EDX and XPS.*

| Element | HEA/g-40 | | | |
|-----------|-----------------------|------------------------|-----------------------|------------------------|
| | XPS | | SEM-EDX | |
| | Wt.% (± 0.1) | E/Mt (± 0.05) | Wt.% (± 0.1) | E/Mt (± 0.05) |
| Fe | 5.6 | 0.15 | 1.0 | 0.16 |
| Co | 6.5 | 0.16 | 0.8 | 0.12 |
| Ni | 9.0 | 0.22 | 1.0 | 0.16 |
| Cu | 11.0 | 0.26 | 1.5 | 0.24 |
| Zn | 9.4 | 0.23 | 1.9 | 0.31 |

Table 3: Elemental composition of the synthesized HEA/g-80 material measured by SEM-EDX and XPS.*

| Element | HEA/g-80 | | | |
|-----------|-----------------------|------------------------|-----------------------|------------------------|
| | XPS | | SEM-EDX | |
| | Wt.% (± 0.1) | E/Mt (± 0.05) | Wt.% (± 0.1) | E/Mt (± 0.05) |
| Fe | 9.9 | 0.18 | 3.2 | 0.13 |
| Co | 5.7 | 0.11 | 4.8 | 0.20 |
| Ni | 14.5 | 0.27 | 4.4 | 0.18 |
| Cu | 14.9 | 0.27 | 6.1 | 0.25 |
| Zn | 9.1 | 0.17 | 6.2 | 0.25 |

Table 4: Elemental composition of the synthesized HEA/g-120 material measured by SEM-EDX and XPS.*

| Element | HEA/g-120 | | | |
|-----------|-----------------------|------------------------|-----------------------|------------------------|
| | XPS | | SEM-EDX | |
| | Wt.% (± 0.1) | E/Mt (± 0.05) | Wt.% (± 0.1) | E/Mt (± 0.05) |
| Fe | 10.1 | 0.22 | 3.2 | 0.25 |
| Co | 6.9 | 0.15 | 1.9 | 0.15 |
| Ni | 11.0 | 0.25 | 2.4 | 0.18 |
| Cu | 9.9 | 0.22 | 2.9 | 0.22 |
| Zn | 7.4 | 0.16 | 2.7 | 0.21 |

*E/Mt = Ratio of each individual element Wt.% and the sum of all the metals Wt.% (note: the Wt.% of C which was excluded from the tables).

4.1.1.4 X-ray diffraction

When it comes to multi-elemental alloys or high-entropy alloys, the phase of the material is a critical parameter, since it can cause different responses in the activity of the catalysts, as well as the selectivity and stability in different experimental conditions. The XRD results (Figure 19) of the samples show a major signal corresponding to the characteristic peak of the graphite (0 0 2) plane at 26° . This signal tends to be a sharp peak for pristine graphite. In the HEA/g-x materials, the peak exhibits a broader shape, which is most likely the result of a modification of the inter-layer distance distribution, causing the broadening. This result is the consequence of two factors; first, the pre-treatment applied to the graphite to activate it, and second, the insertion of the HEA particles in the interlayer zones distorting the crystal structure, without breaking it. The smaller signal around 43° corresponds to the (1 0 0) plane and shows a similar broadening as the main peak. The third and smallest signal at 54° corresponds to the (0 0 4) peak from the graphite structure. The signal present at 45° was attributed to the (1 1 1) plane of the FCC structure of the HEA (FeCoNiCuZn), as reported by Huang et al. [89], and is consistent with the results obtained from the SAED measurements showing a cubic structure (Figure 17g-i). It must be noted that this structure was obtained by direct electrochemical reduction without annealing treatments. The crystallite size of the metallic phases, calculated using Scherrer's equation (Eq. 6), gave an approximate size of (5 ± 1) nm.

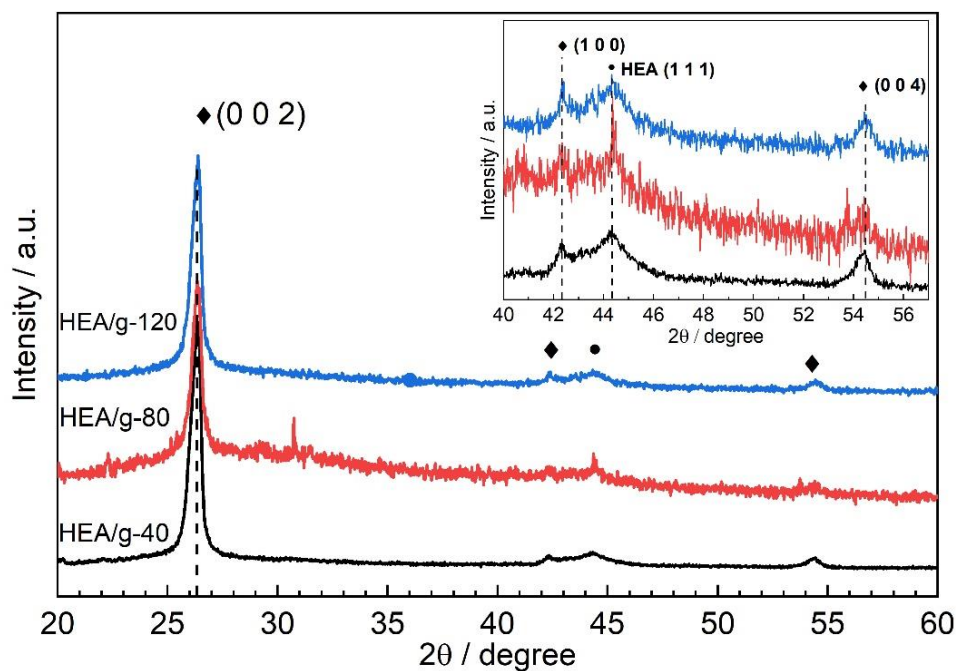


Figure 19: XRD scan of the synthesized materials including peak identification. (\diamond) Graphite signals.

4.1.1.5 FT-IR analysis

The surface of the synthesized HEAs was evaluated using FT-IR, to measure the presence of remnants for the synthesis procedure and to extract information regarding the interactions between the graphite substrate and the catalytic materials. Five principal absorption signals were observed in all the samples. At 3038 cm^{-1} a signal corresponding to the OH band of adsorbed water, overlapped with the characteristic C-H stretching from the aromatic ring corresponding to the graphite support. The other signals 1663 , 1629 , 1479 , and 881 cm^{-1} were attributed to the signals of the graphite substrate, specifically to the C = C stretching, the R-C=C-H stretching, the C-C stretching of the ring, and C-H out of plane vibrations, respectively. No specific signal corresponding to the metal-oxygen interaction or metal-carbon interaction was observed. This supports the conclusion of having the active phase as metallic elements and not as surface oxides and also confirms the role of graphite as a supporting material without any chemical modification on the metallic alloys.

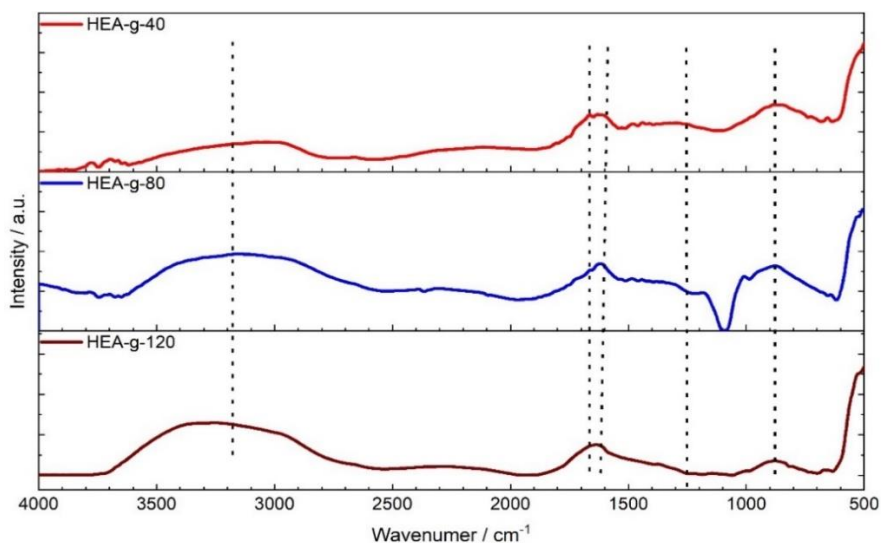


Figure 20: ATR FT-IR of the synthesized HEAs.

Table 5: FT-IR Peaks HEAs from figure 20

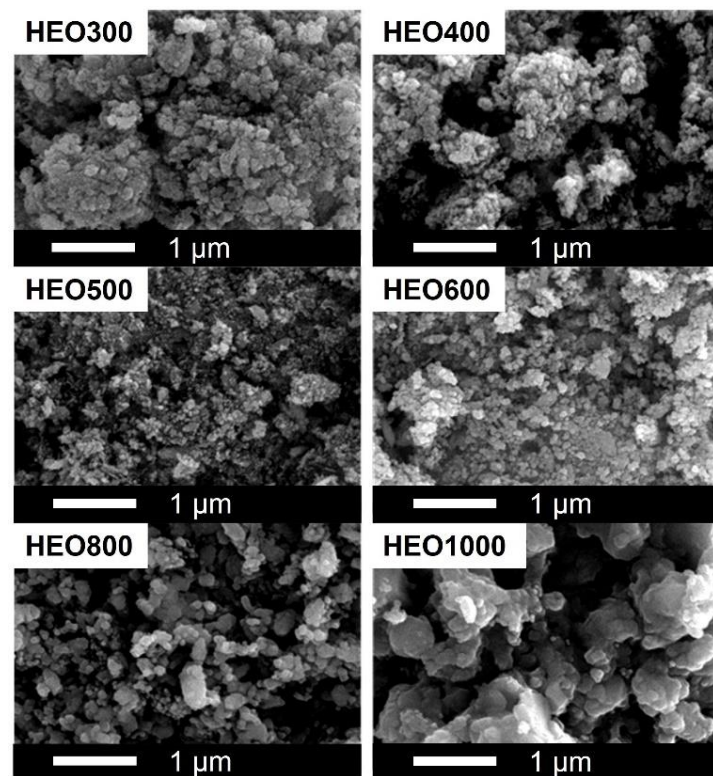
| Wavenumber (cm^{-1}) | Group |
|------------------------------------|----------------------|
| 3038 | Ar – H (stretching) |
| 1663 | C = C |
| 1629 | Ar-CH = CH-R |
| 1479 | C – C (ring) |
| 881 | C – H (out of plane) |

4.1.2 High entropy oxides (HEOs)

4.1.2.1 SEM-EDX

The surface of the catalysts was analyzed using scanning electron microscopy (SEM). The micrographs of the materials shown in Figure 21 present agglomeration of the semi-spherical particles obtained for the lowest calcination temperatures (300 – 600 °C) and sintering for the materials treated at the highest temperatures (800 – 1000 °C). The elemental composition of the catalysts was measured by SEM-EDX and is shown in Figure 22. The elemental mapping of the surface (Figure 22) revealed a homogenous distribution of the elements (Fe, Co, Ni, Cu, Zn) on the surface of the

particles, and no segregation was observed, although the surface concentration of Fe observed was higher than the other elements. This homogeneous distribution of the elements supports the presence of high entropy oxides (HEOs), increasing the interaction between all the elements. The elemental distribution obtained for all the materials was almost equal, with slight differences within the error of the measurements.



CHULALONGKORN UNIVERSITY

Figure 21: SEM images of the synthesized HEOs with different annealing temperatures.

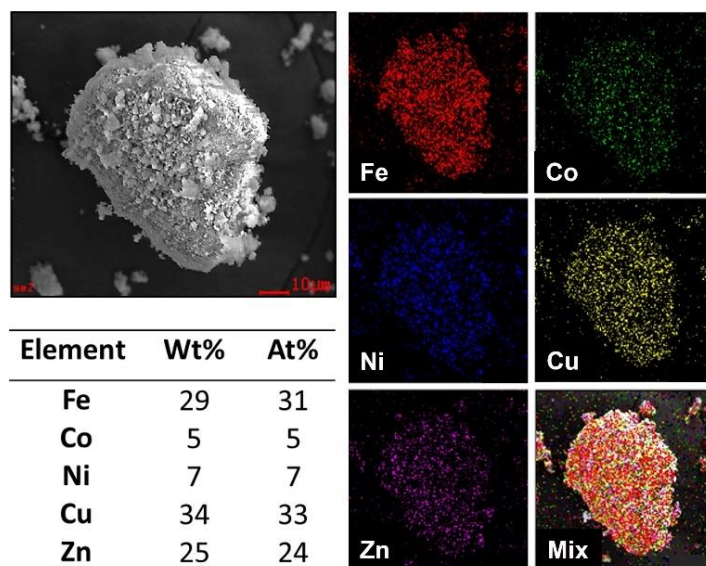


Figure 22: SEM-EDX elemental mapping of the HEO500 catalyst.

4.1.2.2 X-ray diffraction

The crystal structures of the catalysts were measured by XRD and can be seen in Figure 23. The most intense peaks, located at the positions 32° (1 0 0), 34° (1 1 3), 38° (2 2 2), 43° (0 0 4), 58° (1 1 5), and 62° (0 4 4) were attributed to the magnetite (Fe_3O_4 - cubic) structure (JCPDS 96-900-6921). The peaks observed at 36° (0 0 2), 39° (1 1 1) and 49° (2 0 0) were assigned to tenorite (CuO - monoclinic) (JCPDS 96-900-8962), while the peaks observed at 32° (1 0 0), 35° (0 0 2), 37° (1 0 1), 49° (1 0 2) and 57° (1 1 0) corresponded to the structure Zincite (ZnO - Hexagonal) (JCPDS 96-900-4179). The diffraction patterns showed an evident change in the crystallography of the samples as a function of the calcination temperature (Figure 23a). The peaks of the Zincite structure became sharper when the calcination temperature increased from 300°C (small signals) to 800°C (well-defined) decreasing again at 1000°C , while the signal corresponding to the principal peak of the magnetite ($2\theta = 34^\circ$) became the dominant signal, and some from the tenorite ($2\theta = 39^\circ$) remained. These results agree with the results reported by Rost et. al.[83], which showed that different crystallographic phases may arise if the material cools down naturally, instead of applying the quenching process.

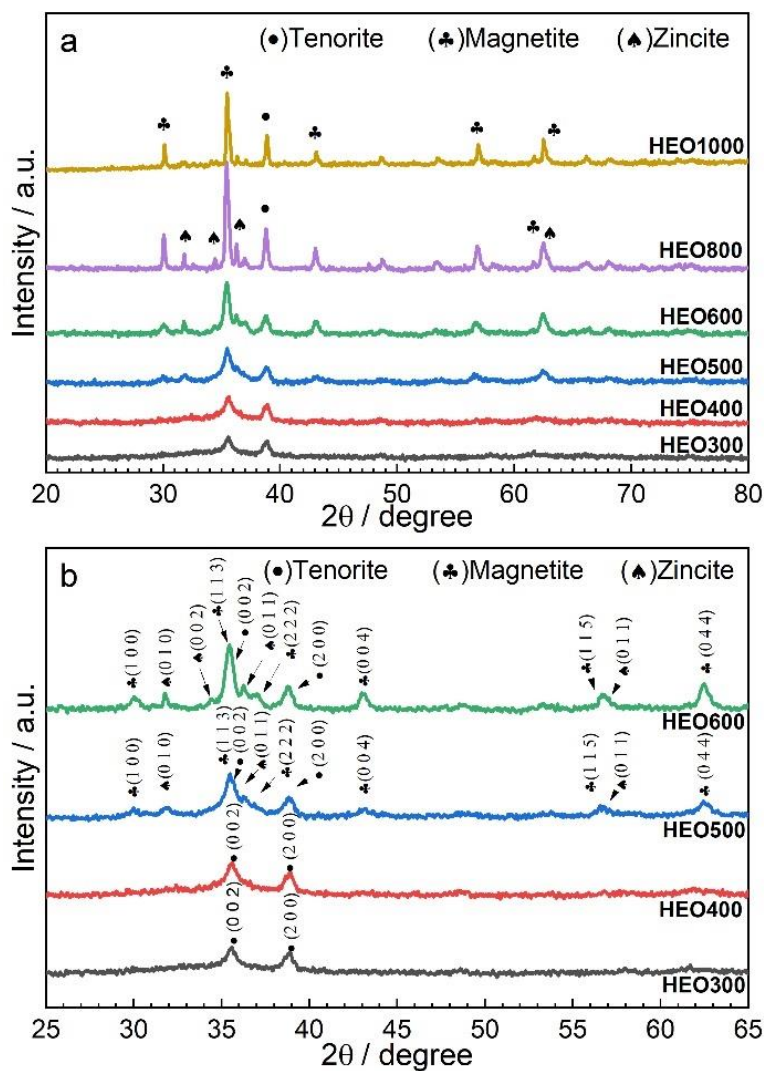


Figure 23: wide angle XRD patterns of the HEOs synthesized at different temperatures. a) Complete scan angles. b) selected angles region. The patterns used correspond to the reference patterns. Magnetite (JCPDS 96-900-6921), Tenorite (JCPDS 96-900-8962) and Zincite (JCPDS 96-900-4179)

4.1.2.3 TGA and DSC

TGA was used to measure the changes in the materials as a function of the temperature and is shown in Figure 24. Three main weight loss signals were observed from the thermal analysis scan. First, a loss of 3.32% wt. below 200 °C was assigned to the dehydration of the sample [83,97]. A second weight loss of 2.02% wt. between 200 and 550 °C was attributed to the loss of strongly-bonded hydroxylated groups

[83,97]. The final weight loss region, above 600 °C was attributed to the loss of any carbonaceous species, or coke, that could have been trapped inside the structure of the HEOs [98]. A final small weight loss above 800 °C was attributed to the change in the spinel structure, where oxygen is lost to change the oxidation state from M^{+3} to M^{+2} [99], this reduction can be reversed if the material is allowed to cool down naturally in the presence of oxygen [83]. From the DSC analysis shown in Figure 24, no evident phase change took place on the materials below 1000 °C, the elemental composition of the materials, and the entropy stabilization. It has been reported that equimolar compositions are required to achieve the eutectic value and reduce the crystallization temperature to obtain solid-state solutions[30,100,101]; in the case of the HEOs synthesized, the composition of Fe, Cu, and Zn were higher than the desired 20%, shifting the crystallization point to higher temperatures[101].

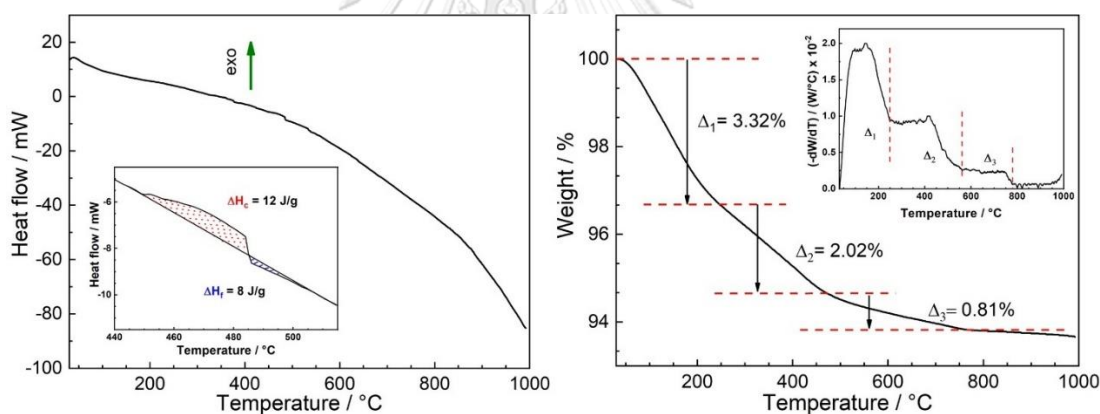


Figure 24: a) TGA measurement of the as-synthesized HEO catalyst annealed at 300°C. b) DSC pattern obtained from the thermal scan of the HEO catalyst annealed at 300°C.

The sintering observed in Figure 21, could cause a decrease in the surface area and an increase in the porosity (pore size and pore volume) with increasing temperatures. The crystallite size of the catalysts was calculated using Scherrer's equation, Eq. (6), and a trend decreasing tren in crystallinity was obtained when the annealing temperature increased.

$$D = \frac{K\lambda}{\beta \cos(\theta)} \quad \text{Eq.(6)}$$

Where K corresponds to the shape factor (0.9 for cubic shape), λ is the X-ray wavelength (1.544 Å), β is the line broadening of the peaks, and θ is the Bragg angle or the position of the peak. A summary of the results obtained from the surface analysis is presented in Table 6. As mentioned previously, a decrease in the surface area and the pore size were observed as functions of the treatment temperature, on the contrary, the pore size and the crystallite size increased directly with the calcination temperature.

Table 6: Physical analysis of the catalysts synthesized using different calcination temperatures.

| Catalyst | BET area (cm ² g ⁻¹) | Pore size (Å ^o) | Pore volume (cm ³ g ⁻¹) | Crystallite size (nm) |
|----------------|---|-----------------------------|--|-----------------------|
| HEO300 | 104 ± 1 | 147 ± 1 | 0.38 ± 0.01 | 12 ± 1 |
| HEO400 | 64 ± 1 | 227 ± 1 | 0.36 ± 0.01 | 12 ± 1 |
| HEO500 | 45 ± 1 | 255 ± 1 | 0.29 ± 0.01 | 11 ± 1 |
| HEO600 | 25 ± 1 | 221 ± 1 | 0.13 ± 0.01 | 15 ± 1 |
| HEO800 | 19 ± 1 | 3 ± 1 | 0.01 ± 0.01 | 27 ± 1 |
| HEO1000 | 1 ± 1 | 752 ± 1 | 0.03 ± 0.01 | 36 ± 1 |

The results shown in Table 6 follow the same trend reported for most catalysts treated at different temperatures. A decrease in the surface area normally involves a decrease in the catalytic activity of the materials due to the lower density of available active sites for the desired reactions [102]. The variation in the crystal size can also affect the catalytic activity of the materials, especially when the reaction is surface sensitive [102].

4.1.2.4 FT-IR analysis

FT-IR ATR (Figure 25) measurements of the materials were performed from 500 to 4000 cm⁻¹ to evaluate the presence of carbon functional groups and the metal-oxygen interactions. The wide band observed between 3380 and 2333 cm⁻¹ was assigned to the OH bonding from water adsorption and hydroxyl species on the surface [103,104]. The decrease in the OH group signal intensity supports the hypothesis of dehydration

of the samples, between 200 °C and 600 °C (Figure 24). For calcination at temperatures above 600 °C, the OH signal showed the lowest intensities (800 – 1000 °C), and a change in the shape of the signal. The signals observed between 1700 and 900 cm^{-1} were assigned to the carbon-containing functional group, probably remaining from the synthesis process [105]. The intensity of these signals decreased with the calcination temperature and was more notorious above 600 °C, where these signals practically disappeared. The signals at 890, 836, 678, and 597 cm^{-1} were attributed to the metal-oxygen vibrations (M-O) [106,107], it should be noted that all the M-O signals have similar intensities, but when calcination temperature increased, the intensity of the signals at 836 and 678 cm^{-1} decreased, while the signals at 890 and 597 cm^{-1} increased.

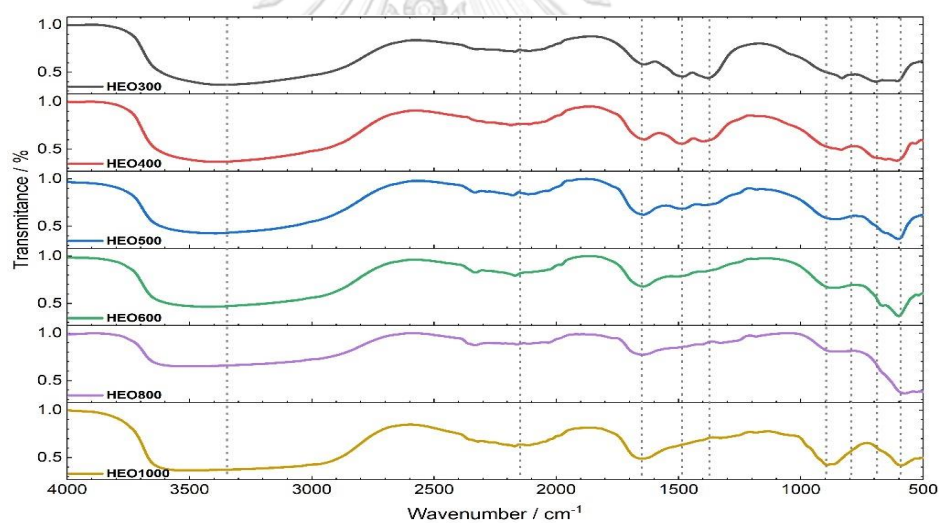


Figure 25: ATR FT-IR of the synthesized HEOs after the annealing process.

This change in the M-O signals supports the conversion from a polycrystalline material obtained at low calcination temperature to a more homogeneous material with a Fe_3O_4 cubic spinel structure [106,107]. A detailed assignment of the peaks observed from the FT-IR measurements is shown in Table 7.

Table 7: FT-IR peaks assignment in Figure 25.

| Wavenumber (cm^{-1}) | Group |
|------------------------------------|---------------------|
| 3380 | OH (stretching) |
| 2333 | OH (bending) |
| 1648 | C = CH ₂ |
| 1490 | C - C (ring) |
| 1367 | C- H (Rocking) |
| 890 | M-O |
| 836 | M-O |
| 678 | M-O |
| 597 | M-O |

4.1.2.5 XPS analysis

The trend observed in Figure 23 and Figure 25 has an associated change in the chemical environment of the elements of the HEOs. These changes were evaluated using XPS, because it can provide analytical information about the condition of the surface, due to its penetration small depth (<10 nm depth), and discrimination of the defects and oxidation states can be made. This information can be used to understand the catalytic activity, especially when surface-dependent processes are involved [97,108]. Figure 26 shows the O 1s high-resolution XPS spectra of the synthesized materials, broad bands were observed for the catalysts treated at low temperatures (300 – 600 °C), and were attributed to the multiplicity of coordination environments derived from multiple oxide structures. In the XPS signals for the materials annealed at higher temperatures (HEO800 and HEO1000) the oxygen signal became increasingly sharp, this as a consequence of the presence of a more homogeneous and crystalline material [97].

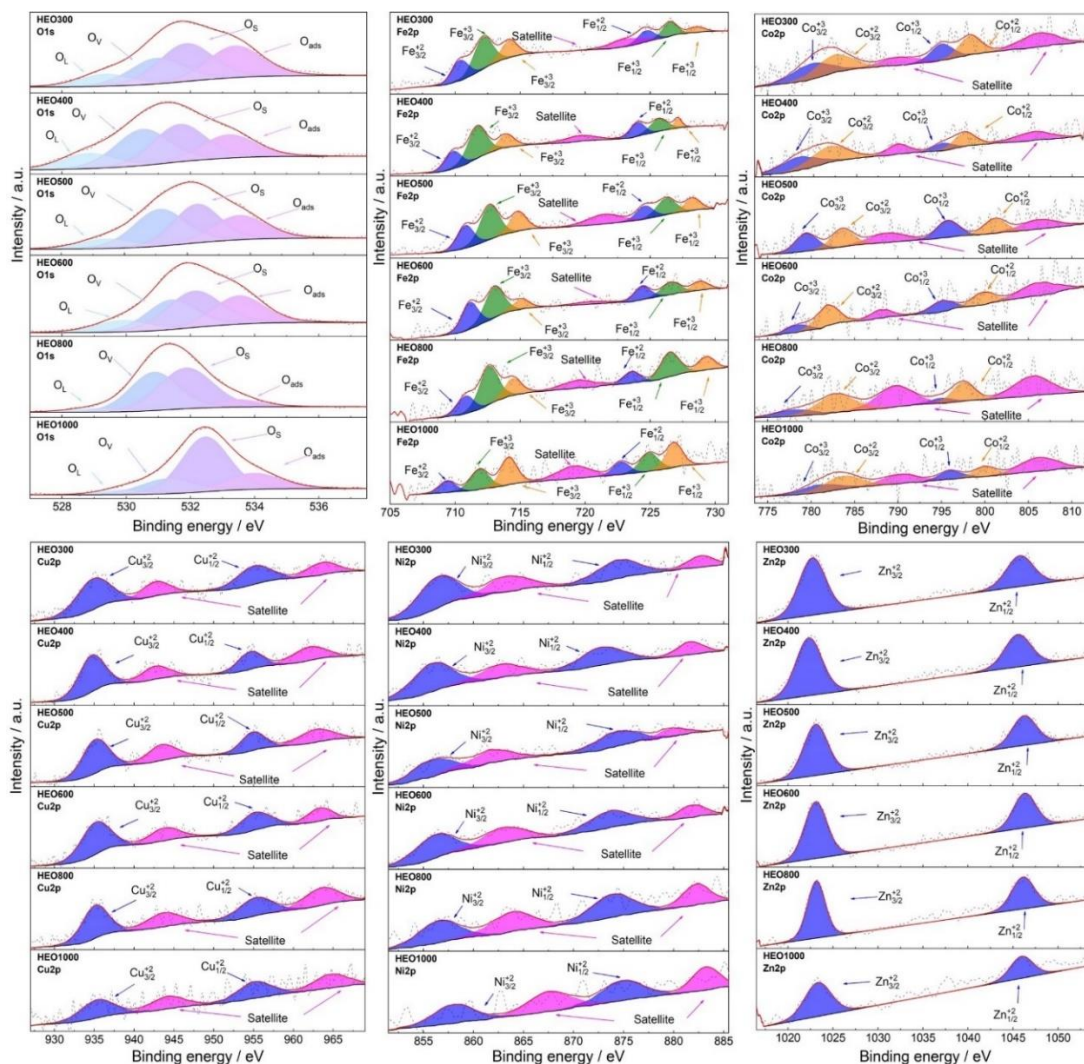


Figure 26: High-resolution XPS measurement of HEOs synthesized with different annealing temperatures.

The O 1s signals were deconvoluted into four components, oxygen atoms in the lattice of the crystal, located at 529 eV (O_L), oxygen atoms in the vicinity of an oxygen vacancy, centered at 531 eV (O_V), oxygen atoms on the surface, with lower coordination number 532 eV (O_S), and oxygen species adsorbed at 533 eV (O_{ads}) [109,110], caused by adsorption from the environment. A remarkable change was observed for the HEOs samples; at the lowest temperatures, a decrease in the O_L was associated to the stripping of OH groups from the lattice observed between 200 and 500 °C (Figure 24). The HEO500 showed the biggest decrease in the lattice oxygen (O_L) and the highest increase in the oxygen vacancies (O_V). These changes were

attributed to the formation of the spinel structure observed (M_3O_4) and the creation of oxygen vacancies [109]. For the HEO600 and HEO800 for the HEO800 the number of oxygen vacancies increased, this was attributed to the subsequent phase change observed from the spinel structure with a combination of M^{+3}/M^{+2} to a structure with mostly M^{+2} oxidation states to arrange all the elements in a uniform crystallographic organization [97,109]. A considerable decrease in intensity of the O_L for the catalysts annealed at higher temperatures (HEO800 – 1000), was attributed to the growth in the material particles caused by sintering. The HEO1000 showed the highest relative content of O_S , corresponding to a more ordered crystallography and bigger particle sizes. An increase in the O_{ads} signal for this material was attributed to an increased hygroscopicity as a consequence of the annealing process. The relative concentrations for the oxygen species on the surface of the different HEOs are shown in Table 8, the ratio of oxygen vacant sites and surface oxygen (O_V/O_S) was calculated, and a clear trend was observed, this value showed an increase with the calcination temperature reaching a maximum value for the HEO500 and afterward, a continuous decrease was observed until the HEA1000.

Table 8: Surface concentration of different oxygen species on the surface of the catalysts measured by XPS.

| Sample | O_L at. % | O_V at. % | O_S at. % | O_{ads} at. % | O_V/O_S |
|----------------|----------------|----------------|----------------|--------------------|-----------|
| HEO300 | 11 | 24 | 35 | 30 | 0.68 |
| HEO400 | 14 | 32 | 33 | 21 | 0.99 |
| HEO500 | 9 | 35 | 33 | 24 | 1.06 |
| HEO600 | 11 | 27 | 36 | 26 | 0.76 |
| HEO800 | 4 | 30 | 53 | 13 | 0.57 |
| HEO1000 | 5 | 18 | 58 | 19 | 0.31 |

* O_L = lattice oxygen, O_V = oxygen vancancy, O_S = surface oxygen and O_{ads} = oxygen from adsorption of water.

The ammount of oxygen vacancies has been reported to be strongly affect the electronic, catalytic, and (electro)chemical properties of the catalysts [111,112], these defects produced by the missing oxygen atoms cause distortions in the lattice of the materials, producing high charge density sites, enhancing the activity and selectivity of complex hydrogenation mechanisms[29,113].

The high-resolution XPS measurements of different metals are shown in Figure 26. In the case of the Fe 2p signal, three species were found, Fe⁺² (710, 724 eV), Fe⁺³ in a tetrahedral coordination site (713, 723 eV), and Fe⁺³ in a octahedral coordination site (714, 728 eV). This also corroborated the presence of the spinel structure, especially when the calcination temperature was above the crystallization temperature (450 °C) [114–116]. The Co 2p measurements also showed evidence of a similar spinel structure. Two species were observed, the first corresponding to the Co⁺³ in an octahedral coordination site (779, 795 eV), and the second one corresponding to the Co⁺² in a tetrahedral coordination site (782, 798 eV), the signals located at 790 and 806 eV were attributed to the surface and bulk plasmonic effects and were considered as the “satellite” peaks. Co⁺³ signals increased and the satellite signals decreased from 300 °C to 500°C, which corresponded to the formation of spinel structures. [115,116]. Co⁺³ decreased at calcination temperatures of 600°C or higher, in line with phase changes in the Co₃O₄ structure to the CoO structure, this is also supported by the increase in satellite signals by the increase in d-d coupling from the octahedral Co⁺². [115], also consistent with the weight loss observed. The Ni 2p XPS spectra remained almost constant in the temperature range studied, and only two species were observed, one corresponding to the Ni⁺² (856, 874 eV) and one corresponding to the satellite signals (863, 882 eV) [114]. A similar behavior was observed for the satellite signal, decreasing to a minimum in the HE0500, corresponding to the presence of the Ni in the spinel structures. The increase in the satellite for the samples calcined above 500 °C, was attributed to the re-crystallization of the spinel structure, increasing the d-d couplings [115]. The Cu 2p signals presented only one species, Cu⁺² (934, 955 eV) and the satellite signals (963, 942 eV) [117]. No Cu⁺¹ or Cu⁰ were observed, consistent with the tenorite structure observed in XRD measurements (Figure 12). The Zn 2p XPS measurements also showed a constant behavior in the Zn⁺² signals observed (1022, 1045 eV) [117], only a slight decrease in the intensity of the sample was observed for the HEA1000, possible caused by the evaporation of segregated Zn.

4.2 High entropy condition

As mentioned before, one of the parameters to determine if a material can be classified as high-entropy alloy is the value of ΔS_{mix} . If this value is above the mark of $1.5R$, the entropy effect is considered high enough to overcome the enthalpy of the mix and the material can be considered to be entropy stabilized, using equation 7:

$$\Delta S_{\text{mix}} = -R \sum_i x_i \ln(x_i) \quad \text{Eq. (7)}$$

Where x_i is the mole fraction of each element and R is the gas constant ($R= 8.3145 \text{ J mol}^{-1} \text{ K}^{-1}$).

Figure 27 and Figure 28 show the individual contribution of each element, in each sample, to the entropy of the mix using the concentrations obtained from EDX measurements (Table 4 and Figure 11), and it shows how the ΔS_{mix} of the materials falls within the range of high entropy stabilized materials [17,79,118]. It is important to notice that the contribution of each component increases steeply in the mole fraction range from 0.05 reaching a maximum value at $x_i = 0.35$, and after $x_i > 0.4$ the contribution to the entropy decreases sharply until it becomes zero when $x_i = 1$ shown in Figure 27 and 28. This is the reason why increasing the concentration of a single element beyond this value has a negative effect on the contribution to the entropy of the mix.

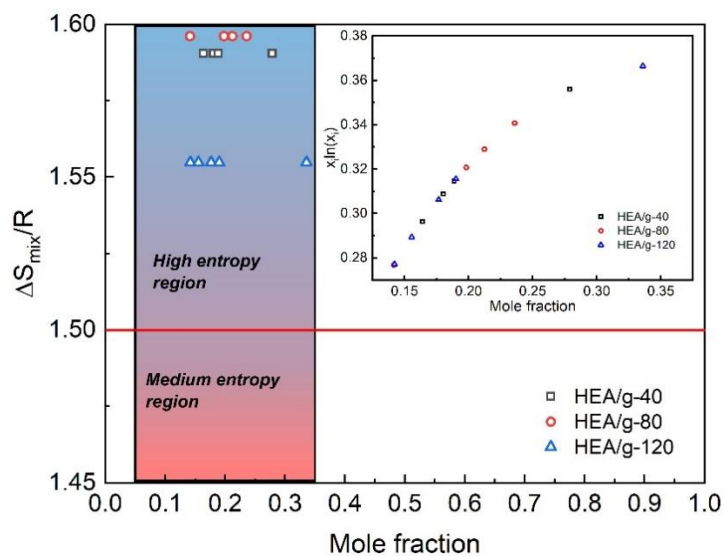


Figure 27: Entropy diagram of synthesized HEAs

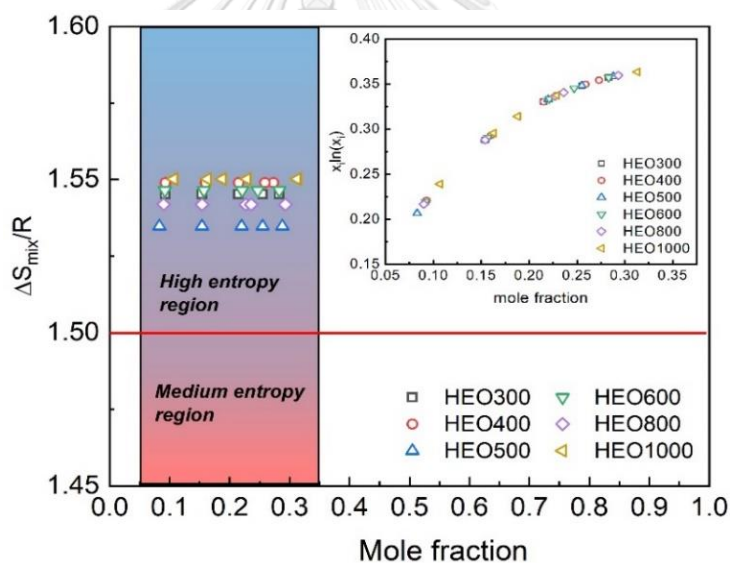


Figure 28: Entropy diagram for synthesized HEOs

4.3 Catalysts electrochemical characterization

4.3.1 Linear sweep voltammetry

To further study the elemental distribution and presence of different phases or metal segregations, linear scan voltammetry (LSV) was carried out in alkaline media. The reduction of the different oxide species present on the surface was examined. Figure

29 shows the electrochemical response of the three synthesized materials. For samples HEA/g-80 and HEA/g-120, a single broad signal was observed at -0.5 V (as indicated by arrow *a*), where the reduction of surface oxides (-0.5V) and water reduction (-1.0V) were overlapped, causing the loss of a well-defined peak for each process, and producing a current increase and reaching a quasi-steady-state until -1.4 V where hydrogen evolution took place and the current increased exponentially. This single signal showed that there is no metal segregation, as confirmed previously by SEM-EDX. In the case of the catalyst HEA/g-40, the signal showed two distinct peaks, the first at -0.5 V (*a*) and the second at -1.0 V (*b*), and finally, the hydrogen evolution reaction took place at -1.6 V (*c*). In this case, these two peaks were attributed [119–124] to the reduction of the surface oxide and the adsorption of water (according to the Volmer mechanism) before the hydrogen massive evolution. In Figure 29b, the linear sweep voltammeteries of the HEAs in the anodic direction showed good activity towards the oxygen evolution reaction, a first signal was observed for the HEA/g-120 material with a peak at 0.4 V, this signal was only observed for this material, this could be attributed to the increase in the metal loading which could favor the formation of an oxidized surface previous to the oxygen evolution reaction. A second signal was observed for the three catalysts, this signal was attributed to the oxygen evolution massive reaction (OER). The overpotentials for this reaction followed the same trend observed for the HER, where the HEA/g-40 showed the higher overpotential, therefore a bigger potential window to work without the solvent decomposition. Following these results, the material HEA/g-40 was selected to analyze the effect of pH on the behavior of the electroactive sites and the effect of nitrobenzene adsorption on the surface dynamics. The criteria to choose this material were two-fold, namely the separation of the reduction signals allowing a more comprehensive analysis and the wider potential window compared with the other two synthesized materials, which allows the study of the surface without the interference of the massive hydrogen evolution.

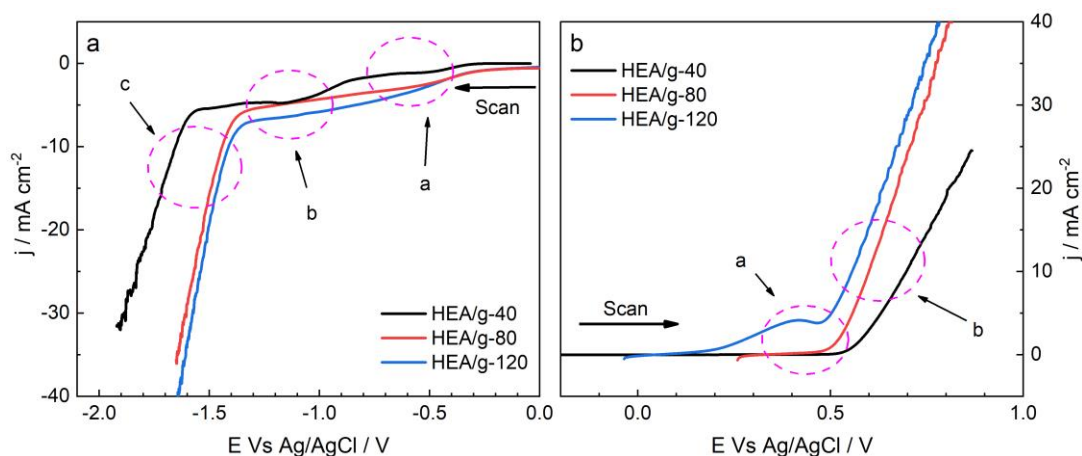


Figure 29: Linear sweep voltammograms of HEA electrodes with different loadings. Scan rate 1 mV/s , $\text{Na}_2\text{SO}_4 \text{ } 0.1 \text{ M}$. a) cathodic direction scan. b) anodic direction scan.

The hydrogen evolution mechanism on the HEAs was evaluated using the Tafel analysis, as shown in Figure 30a. The Tafel slope for the hydrogen evolution obtained for the three catalysts was 154 mV dec^{-1} (HEA/g-40), 129 mV dec^{-1} (HEA/g-80), and 136 mV dec^{-1} (HEA/g-120); these obtained values mean that the hydrogen evolution mechanism follows the Volmer-Heyrovsky mechanism and that the hydrogen production is strongly dependent on the applied potential.

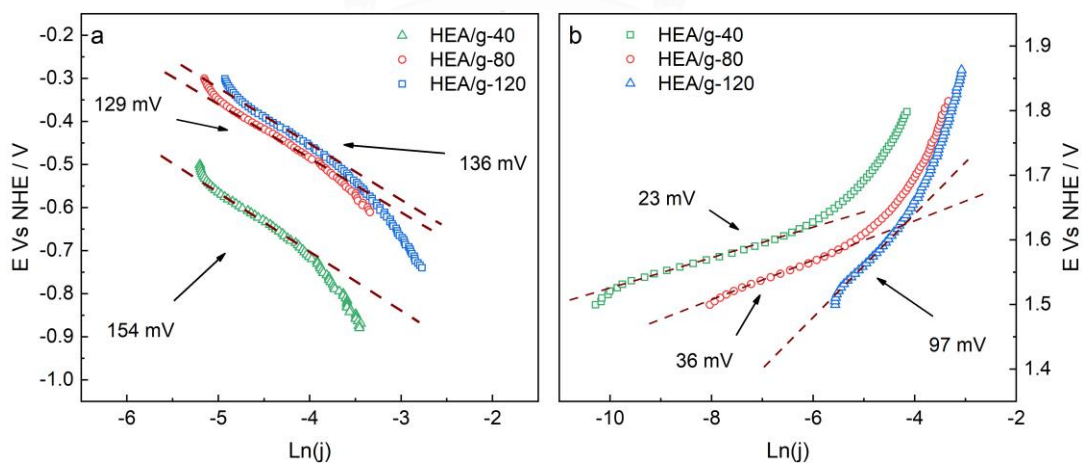


Figure 30: Tafel plots of HEA electrodes from LSV in figure 29. a) Cathodic scan. b) Anodic scan.

The activity at alkaline pH (i.e., in KOH) was higher for both hydrogen evolution and oxygen evolution, showing a stronger interaction between water molecules and the surface. In the case of hydrogen, the onset potential for massive H₂ evolution was located after the second reduction signal (-1.1 V), while for acid medium (i.e., Na₂SO₄) the H₂ evolution starts after -1.5 V and with a lower current than for the alkaline medium. This could be explained by a strong interaction between the protons and the surface, a behavior consistent with that reported for Cu electrodes [125], where the surface adsorption energy is considerably high thus stabilizing the adsorbed hydrogen species (-H) and reducing the effect of the applied potential, and slowing down the kinetics of the hydrogen evolution (Volmer-Tafel mechanism). In the case of the basic medium, the hydrogen promoting species was not the proton (H⁺), but the adsorbed water molecule (-OH₂), which adsorbs rapidly once the surface oxides were reduced, and reacted with a much stronger dependence on the potential than in acidic pH (Volmer-Heyrovsky mechanism) (Figure 31).

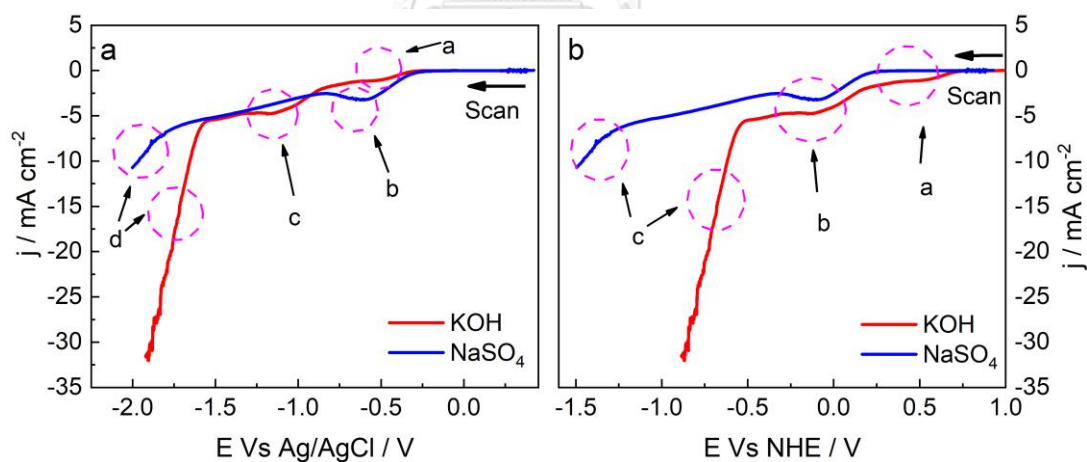


Figure 31: Linear sweep voltammograms of HEA/g-40 electrodes in different solutions. Scan rate 1 mV/s, Na₂SO₄ 0.1 M and KOH 1.0 M. a) Vs Ag/AgCl reference electrode. b) Vs NHE (pH = 0).

One of the causes for the drastic change in the electrochemical behavior as a function of the pH of the solution was the formation of the surface oxides, which enhanced the affinity of the surface to water molecules and therefore the oxygen evolution kinetics. It is important to notice that the oxygen evolution region showed a pronounced onset

near 0.5 V in alkaline solution, whereas, in acid solution, the surface was less susceptible to oxidation, and therefore the oxygen evolution kinetics were much slower. Similar behavior was observed in the reduction region (Figure 31a), where the electrode showed poor activity towards hydrogen evolution in Na₂SO₄ solution even at considerably high overpotentials ($\eta > -1.0$ V). In this regard, strong adsorption of protons on the surface, and high stability promoted by Cu and Zn [43] limit hydrogen evolution. On the contrary, in an alkaline medium, the reduced surface had also strong adsorption of water molecules, which were easily activated and catalyzed the massive hydrogen evolution after smaller overpotentials ($\eta > -0.5$ V). To properly evaluate the effect of the overpotential on the hydrogen evolution reaction and its availability for transferring to other organic molecules for hydrogen transfer reaction (HTR), the linear scan voltammetry was plotted in the reversible hydrogen potential scale (Figure 31b), as given by Eq. (8):

$$E_{\text{SHE}} = E_{\text{electrode}} + E_{\text{Ag/AgCl}}^0 + 0.059\text{pH} \quad \text{Eq. (8)}$$

In the hydrogen scale, the higher activity of the HEA electrode in alkaline medium was expected. The fact that the reduction signal at -0.1 V in both cases matches perfectly, means that the hydrogen (or water) adsorption takes place rapidly once the surface is completely reduced thereby exposing the metallic surface, and the subsequent hydrogen evolution.

When comparing the Tafel slopes in both conditions (acid and alkaline pH with no nitrobenzene), a remarkable difference was observed (Figure 32). The results showed a slope of 154 mV in alkaline medium meaning the hydrogen evolution reaction can be controlled by the Volmer reaction, and the surface coverage is the rate-limiting factor. In the case of the acidic medium, a much higher slope of 4413 mV was obtained, which implies the hydrogen evolution process was not controlled by the hydrogen reduction mechanisms (Volmer-Tafel, Volmer-Heyrovsky) but most likely controlled by diffusion, or a much higher voltage input is required to achieve proper activation of the adsorbed species.

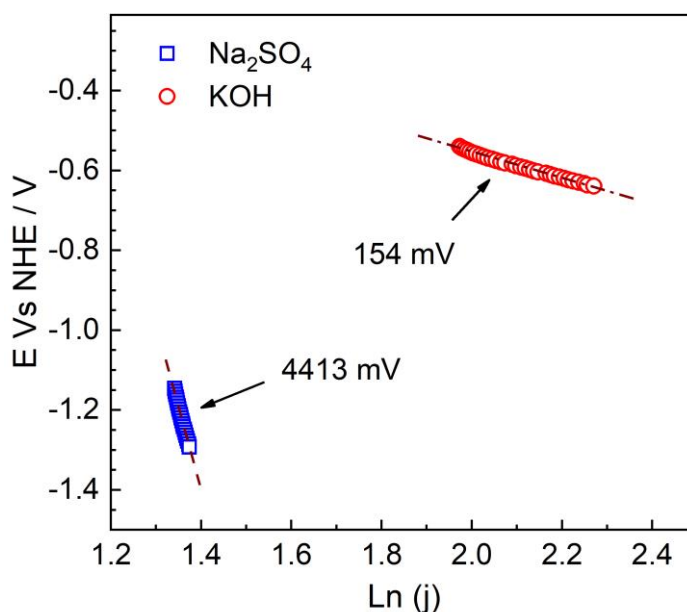


Figure 32: Tafel plots for hydrogen evolution reaction of the synthesized HEAs in two different pH values. Na_2SO_4 0.1 M (pH = 5) and KOH 1.0 M (pH = 14).

The hydrogen evolution reaction (HER) activity of the synthesized HEOs was evaluated using linear sweep voltammetries (LSV) at a slow scan rate (1 mV s^{-1}) to reduce the effect of capacitive currents (Figure 33a). The Tafel slopes (Figure 34a) were calculated and showed an increasing trend. The HER mechanism has been extensively studied [126] and the rate-limiting step (RLS) can be estimated using this parameter. First, when the mechanism is controlled by a fast reaction between the adsorbed hydrogen and a proton (or water molecule) from the medium (Volmer-Heyrovsky mechanism) Eq. (2) and (4), the Tafel slope has a value of 40 mV per decade, this condition is associated with a low concentration of hydrogen on the surface, this was the case observed for the Pt/C catalyst (46 mV dec^{-1}), as seen previously [127,128], and for the HEO300 (44 mV dec^{-1}) [128]. A second mechanism, characterized by a high surface concentration of adsorbed hydrogen, where the rate-limiting step is a potential independent reaction, the surface recombination, (Volmer-Tafel mechanism) following Eq. (2) and (3), normally presents a slope of 60 mV per decade, similar to the results obtained for the HEO400 (53 mV dec^{-1}), HEO600 (70 mV dec^{-1}) and HEO500 (61 mV dec^{-1}) [128]. In the third case, where the water

discharge reaction and the generation of active hydrogen is the rate-limiting step, the Tafel slope gives a higher value of 120 mV per decade (Volmer reaction Eq. (2)), this was similar to the results obtained by the HEO800 (93 mV dec⁻¹) and HEO1000 (100 mV dec⁻¹) [128].

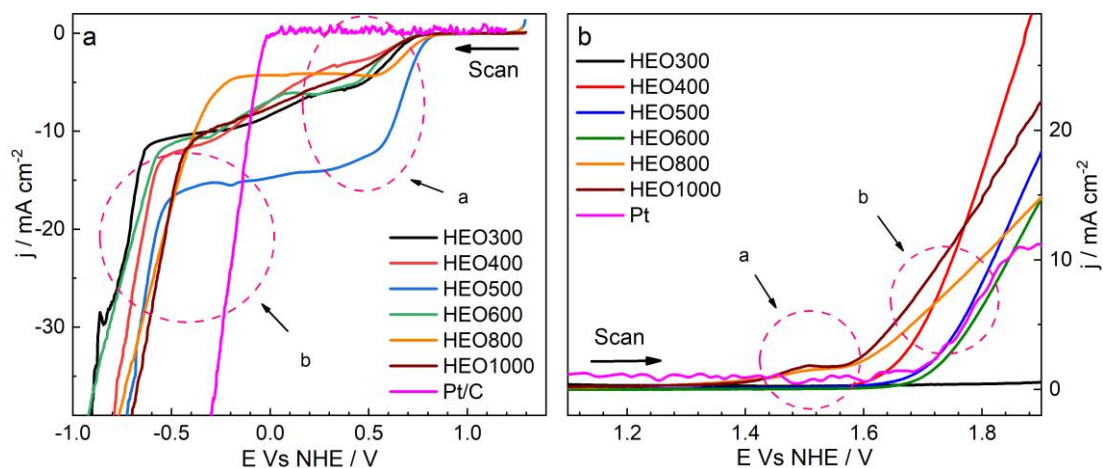


Figure 33: Linear sweep voltammies (LSV) of the synthesized HEOs in 1.0 M KOH solution at a scan rate of 1 mV/s. a) Cathodic scan. b) Anodic scan.

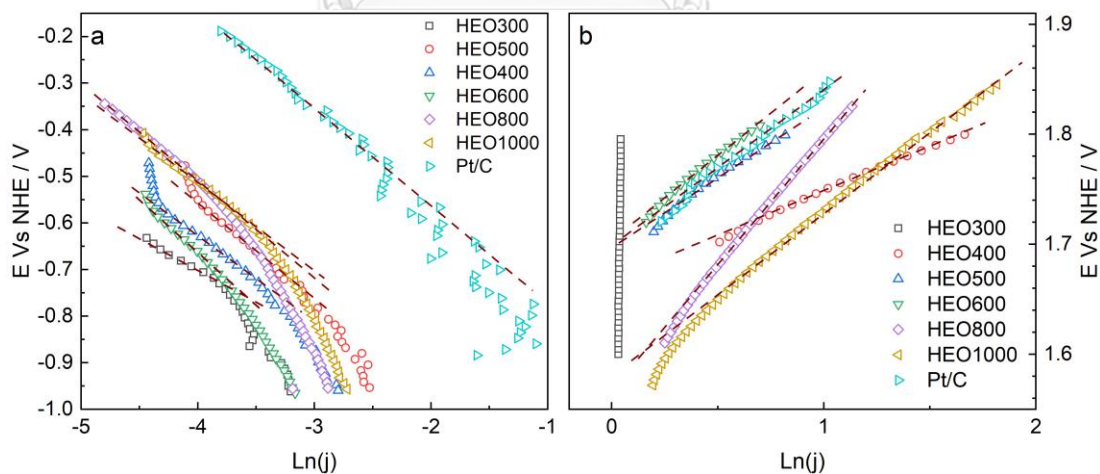


Figure 34: Tafel plots extracted from the data in figure 33 of the synthesized HEOs in 1.0 M KOH solution at a scan rate of 1 mV/s. a) HER. b) OER.

4.3.2 Cyclic voltammetry

4.3.2.1 Electrochemical behavior of HEA in acid medium

Figure 35a depicts the cyclic voltammetry data of the HEA/g-40 electrode in 0.1 M Na_2SO_4 (pH 5). At slow scan rates ($5 - 10 \text{ mV s}^{-1}$), a reduction signal was observed at -0.5 V , corresponding to the surface oxide reduction. When the scan rate increased ($50 - 500 \text{ mV s}^{-1}$), the signal shifted to 0 V and a strong capacitive behavior was observed. This high capacitance was caused by the roughness and porosity of the electrode. It can be noted that there is an oxidation signal at 0.6 V followed by the oxygen evolution signal after 1.0 V . The oxidation signal was attributed to the oxidation of the metallic surface. According to Löffler et al. [82], the broad nature of this signal can be related to the multiplicity of metals on the surface and their interactions. This behavior is characteristic of metallic alloys and supports the argument that the electrode is a solid-state solution [82,129]. In the case of metal segregation, the oxidation region would be composed of different individual peaks. The presence of surface oxides has been widely reported [130–132] to act as promoters to the oxygen evolution reaction (OER), or the oxygen transfer reaction (OTR). . Figure 35b shows the effect of adding nitrobenzene ($400 \mu\text{M}$) to the solution, to evaluate how it affects the surface dynamics of hydrogen adsorption, the surface oxides formation, and their subsequent reduction. Figure 9a shows an increase in the reduction current when nitrobenzene (NB) was added to the acidic solution starting at 0.8 V . This increase corresponds to the first reduction peak of the surface oxides of the electrode, which means the nitrobenzene rapidly adsorbs in the surface and was reduced once the metal surface was exposed. For applied potential more negative than -0.5 V ($\eta = 0 \text{ V}$ for hydrogen reduction), the current sharply increased, which can be attributed to the irreversible reduction of nitrobenzene involving hydrogen transfer. A similar behavior was observed for Cu electrodes [48–50], thus we can assume that Cu sites actively participate in the nitrobenzene hydrogenation process either by acting as the adsorption site or by providing the adsorbed hydrogen species required for the hydrogenation process.

In the positive scan direction, an oxidation signal appeared at 0 V, which was attributed to the reversible oxidation of reduced nitrobenzene where hydrogen transfer was not involved yet. Finally, a wider signal was observed above 0.2 V overlapping the oxygen evolution signal, which was attributed to the oxidation of reduced species coming from the reduction of nitrobenzene, and the formation of surface oxides of the alloy

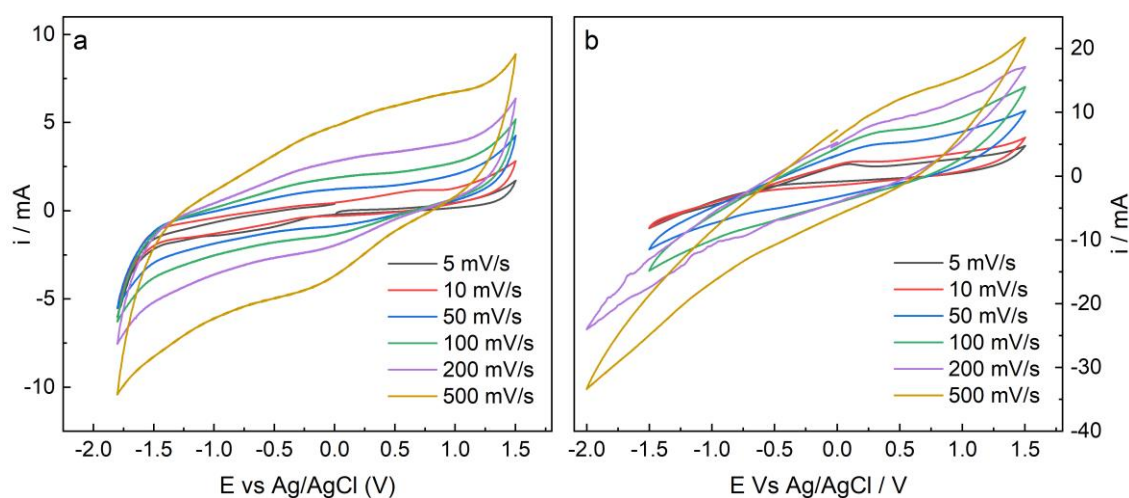


Figure 35: Cyclic voltammograms of HEA/g-40 electrode in Na_2SO_4 at different scan rates. a) $0.1 \text{ M Na}_2\text{SO}_4$. b) $0.1 \text{ M Na}_2\text{SO}_4 + 400 \mu\text{M NB}$

4.3.2.2 Electrochemical behavior of HEA in Alkaline medium

The same approach was used to analyze the electrochemical behavior of the HEA/g-40 electrode in an alkaline medium (KOH, pH 14). It has been reported that high-entropy alloys can present activities comparable to Pt when used for hydrogen evolution in highly alkaline media [135]. Results strongly depend on the composition of the alloy and the synthesis method, and their activity is much more difficult to understand and model due to the multiplicity of possible active sites and their behavior as a function of the pH. In Figure 36a, the cyclic voltammetry data of the HEA electrode shows a behavior completely different from the results obtained at acidic pH. In this case, two clearly defined reduction signals were present (-0.49 V and -1.0 V), which were attributed to the reduction of the surface oxides and the adsorption/reduction of water molecules [82]. In the positive direction scan, a single

but wide signal with a maximum at -0.4 V extended between -1.0 V to 0.2 V approximately. This type of signal was characteristic of multi-elemental alloys where many possible surface oxides can be produced due to the multiplicity of metallic atoms and surrounding environments. Furthermore, the fact that only one peak was seen in that region means that there was a solid solution and there was no metal segregation. A final peak was present at 0.5 V, which is characteristic of Ni and Co alloys due to the formation of the oxo-hydroxide surface species (NiOOH and CoOOH) which have been reported [136] as intermediates for the oxygen evolution reaction in this kind of metals and as important reactive species in electrochemical direct oxidation processes. When it comes to the hydrogen evolution/transfer process, the HEA electrode presented a high overpotential for the reaction to take place (Figure 31, below -1.5 V). This gave a broad working window making it possible to tune the desired products obtained by means of controlling the applied potential. Figure 36b shows how the first reduction signal of the alloy (-0.5 V) was drastically reduced at pH 14, while there was an increase in the reduction signal afterward, overlapping with the second reduction signal of the alloy (-1.0 V). This was attributed to the strong adsorption of the nitrobenzene on the surface and the competition with the water molecules (H_2 precursors) for the active sites. This strong adsorption and subsequent competition also hindered the surface oxidation of the electrode, which caused the loss or decrease in the oxidation signals of the electrode at positive potentials. These results also imply that the reversible direct reduction of the nitrobenzene was unfavored and that the hydrogenation mechanism was favored during the nitrobenzene conversion

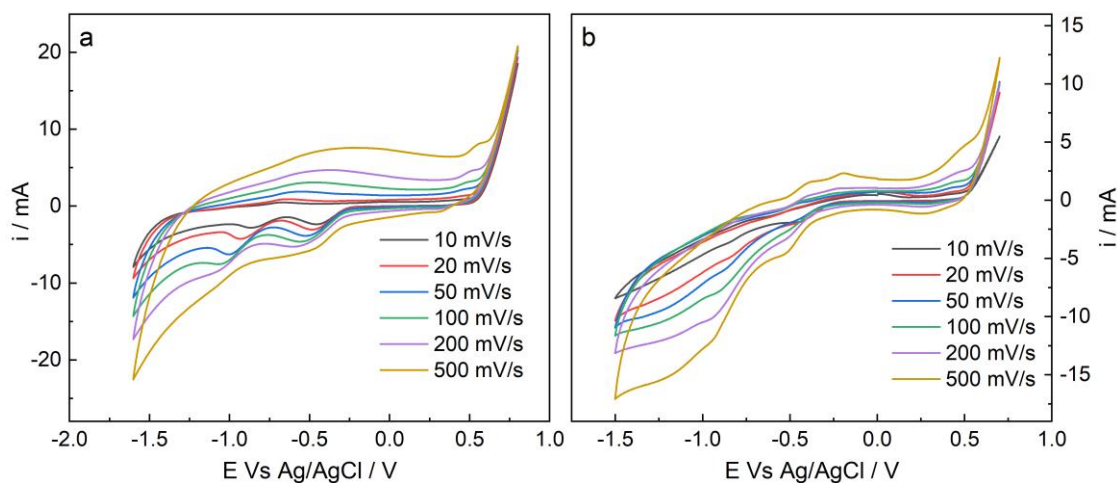


Figure 36: Cyclic voltammograms of HEA/g-40 electrode in KOH at different scan rates. a) 1.0 M KOH. b) 1.0 M KOH + 400 μ M NB.

4.3.2.3 Electrochemical behavior of HEOs

The electrochemical properties of the HEO catalysts were measured using cyclic voltammetry (CV) to determine their potential working window, and stability. Figure 37 shows the CVs for the HEO catalysts and the substrate clean (graphite). Three principal oxidation peaks (O_{x1} , O_{x2} , and O_{x3}) and two reduction peaks (R_{ed1} and R_{ed2}) were obtained for all the catalysts. The first signal (O_{x1}) was attributed to the oxidation of Cu^0 sites to produce Cu_2O and the oxidation of Fe^0 to Fe_3O_4 [137,138]. This peak (O_{x1}) was observed for the HEOs sintered above 400 $^{\circ}C$, the peak position shifted to more positive values with increasing temperatures from -0.66 V (HEO400) to -0.58 V (HEO1000) vs. Ag/AgCl. The increase in the intensity of this signal was correlated to the increase in the tenorite and magnetite phases observed from the XRD results (Figure 23). The second oxidation peak (O_{x2}) showed a shift from -0.39 V (HEO400) to -0.29 V (HEO1000). This peak was attributed to the oxidation of the spinel structures comprising Fe_3O_4 to the Fe_2O_3 , $Co(OH)_2$ to Co_3O_4 , and NiO to Ni_3O_4 [137–139]. The last oxidation signal (O_{x3}) was assigned to the formation of the species CuO , CoO , and NiO_2 [137]. This last signal was observed for all the catalysts, and showed a considerable potential shift and increase in current value from -0.2 V and 1.59 mA (HEO300) to 0.07 V and 8.19 mA (HEO1000). The shift observed for

the oxidation signals was explained by the increased stability of the oxide species with an increase in particle size and crystallinity. The enhanced interaction of all the elements of the single-phase high-entropy condition had a beneficial effect on the electrochemical stability. A singular behavior was observed for the electrode prepared with the HEO500, the three oxidation signals appeared to be more overlapped than for the rest of the materials, this could be caused by the presence of the spinel structures as the main structure, produced from the heat treatment. This result is also consistent with a higher current at potentials where the oxo-hydroxide species are normally observed (≈ 0.5 V vs Ag/AgCl) [137,138]



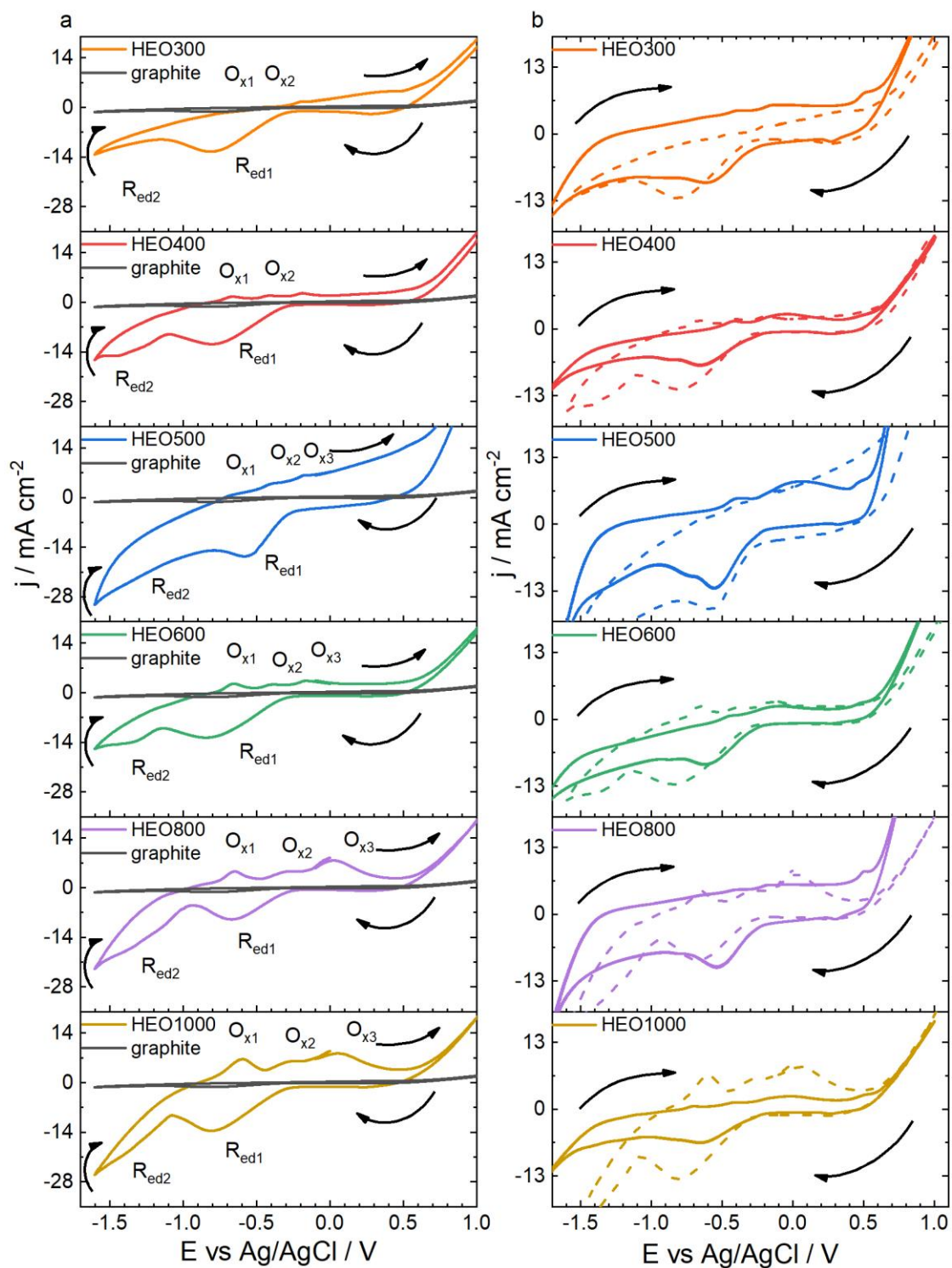


Figure 37: Cyclic voltammeteries obtained for the different HEO electrodes at a scan rate of 50 mV/s. a) in 1.0 M KOH. b) in 1.0 M KOH + 400 μM NB.

The reduction signals observed for all the materials were attributed to two principal processes. The first process (R_{ed1}) was attributed to the reduction of the surface oxides, and the second signal (R_{ed2}) was attributed to the accumulation of hydrogen on the surface of the catalysts [140,141]. The region after the first reduction (from -1.0 to -1.6 V) was defined as the working window to promote surface hydrogenation reactions. The HEO500 catalyst exhibited a different behavior, with a lower potential for the reduction of the oxides (-0.56 V) than the other electrodes, and a continuous current increase until reaching the hydrogen evolution region ($E_{app} < -1.6$ V). This pseudocapacitive behavior was attributed to the increased number of structural defects and oxygen vacancies; these two factors increase the number of available electroactive sites for adsorption [142] and facilitate the electrochemical processes increasing the current [143].

4.3.3 Electrochemical impedance spectroscopy

4.3.3.1 The impedance of HEA in acid medium

To analyze the surface coverage and the effect of the applied potential, electrochemical impedance spectroscopy (EIS) was used by applying an AC perturbation of $\Delta E = 10$ mV. The Nyquist plots collected at different applied potentials are shown in Figure 38, and the results were compared to an (R(RQ)) equivalent circuit [144]. The values for charge transfer resistance (R_{ct}) and capacitance (C) are shown in Figure 39, where a progressive increase in the capacitance of the electrode was observed from -0.5 V, reaching a maximum value at -1.5 V and decreasing steeply at -2.0 V. This trend, combined with the linear sweep voltammetry results, indicates a strong adsorption and high coverage of the surface of the electrode as a function of the applied potential [133,134]. This strong adsorption occupies the available electroactive sites causing an increase in the surface concentration of hydrogen. However, the recombination of these H atoms is slow, which means they are available to be transferred to different organic molecules, thus increasing the possibility of controlled hydrogenation processes. When the applied potential is more negative than -1.5 V, the energy is enough to activate the adsorbed

hydrogen atoms and generate the massive hydrogen evolution. This may be the cause of the sharp decrease in the capacitance of the electrode due to the decrease in the surface concentration of H atoms. This decrease in the surface concentration and increase in the hydrogen evolution is also promoted by a decrease in the charge transfer resistance as a function of the applied potential (Figure 39), which reaches a minimum value at -2.0 V. The combination of high hydrogen coverage and low charge transfer resistance makes the applied potential of -1.5 V a convenient electrical condition when it comes to the catalysis of the hydrogen transfer reaction because it promotes a hydrogenation process with low participation of the hydrogen evolution [133,134].

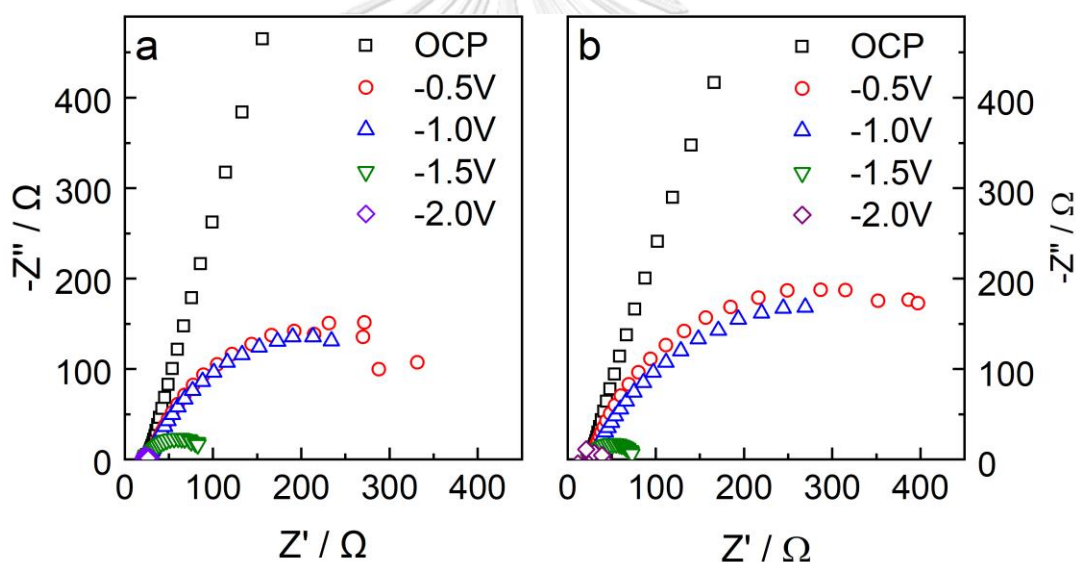


Figure 38: EIS measurements (Nyquist plot) of the HEA/g-40 electrode at different applied potentials. a) in 0.1 M Na_2SO_4 . b) in 0.1 M $\text{Na}_2\text{SO}_4 + 400 \mu\text{M NB}$

The aforementioned maximum in the capacitance due to hydrogen adsorption can be used as a boundary value to control the products obtained. At potential values below this maximum, the extensive hydrogenation products were not favored, and any direct reduction products were obtained favorably. On the other hand, at more negative potential values (i.e., beyond the maximum value), the extensive production of

hydrogenation products was improved, but at the cost of a lower Faradaic efficiency due to the strong activation of the H₂ evolution.

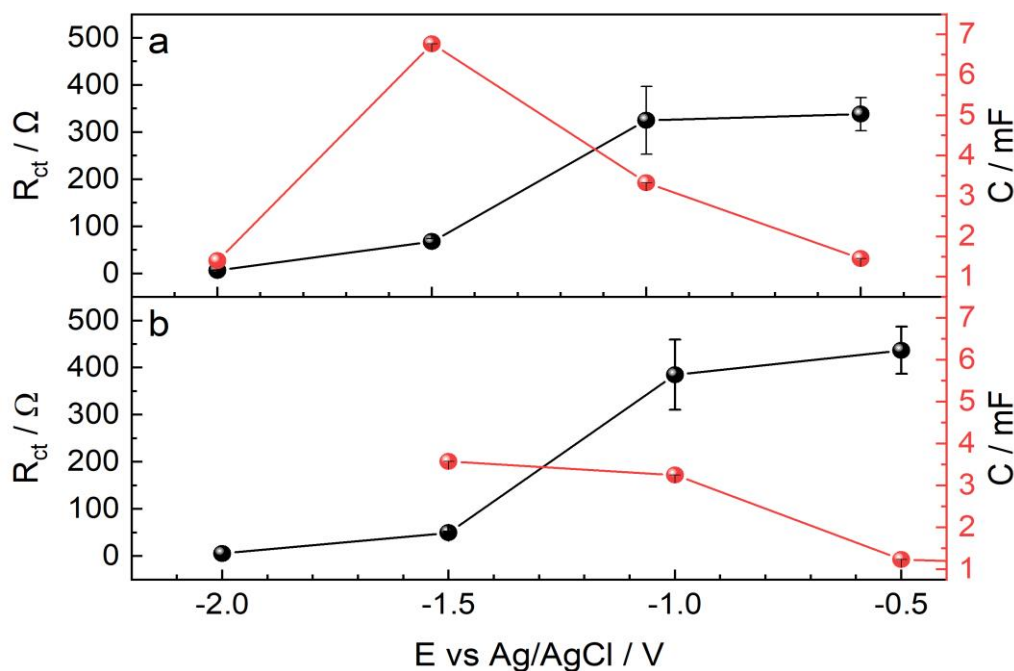


Figure 39: R_{ct} and C_p parameters extracted from the EIS measurements using an $R_s(R_{ct}C_p)$ equivalent circuit. a) in 0.1 M Na₂SO₄. b) in 0.1 M Na₂SO₄ + 400 μM NB.

4.3.3.2 The impedance of HEA in alkaline medium

The impedance experiments in an alkaline medium (Figure 40) showed an increase in surface capacitance (C) with a maximum value at -1.0 V, which corresponded to the position of the second reduction peak seen in the cyclic voltammetry and the linear scans. These results imply that the adsorption of water molecules was hindered by the presence of surface oxides, which also explains the dramatic reduction of the charge transfer resistance (R_{ct}), at -1.5 and -2.0 V, once the oxides were reduced (Figure 41). When the reduction process was completed after -1.0 V the metallic surface was exposed, and the adsorption reached a maximum value [133,134]. This surface concentration of adsorbed water molecules decreased at -1.5 and -2.0 V. The decrease in the surface concentration was attributed to the activation of the hydrogen evolution process, which did not seem to be strongly affected by the applied potential between -1.0 V and -1.5 V [133]. This means the process followed the Volmer-Tafel

mechanism, and after -1.5 V the current increases exponentially with the applied potential, and the Volmer-Heyrovsky mechanism became dominant. Because of this, the surface concentration of hydrogen (or water in alkaline pH) was considerably reduced, caused by these reactions taking place simultaneously.

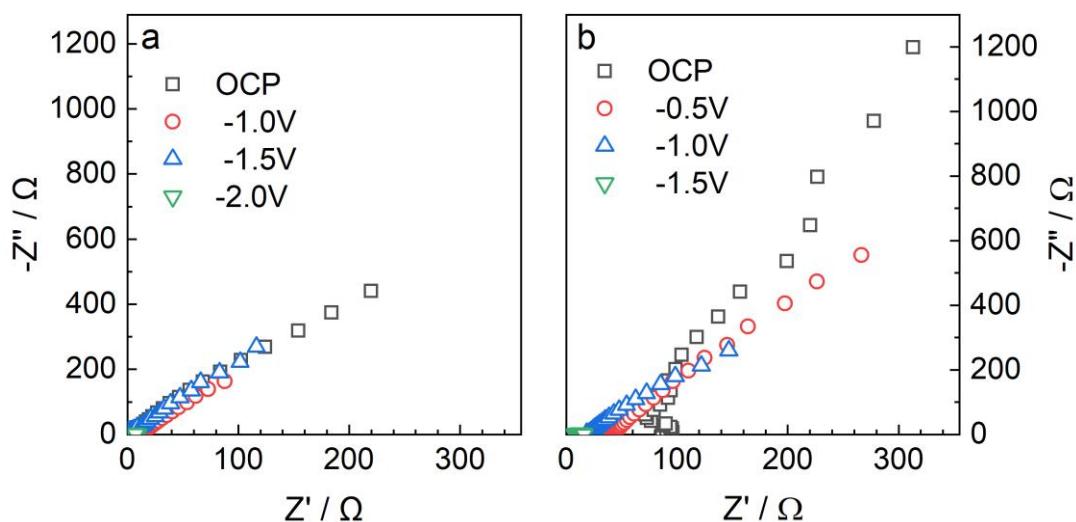


Figure 40: EIS measurements (Nyquist plot) of the HEA/g-40 electrode at different applied potentials. a) in 1.0 M KOH. b) in 1.0 M KOH + $400 \mu\text{M}$ NB

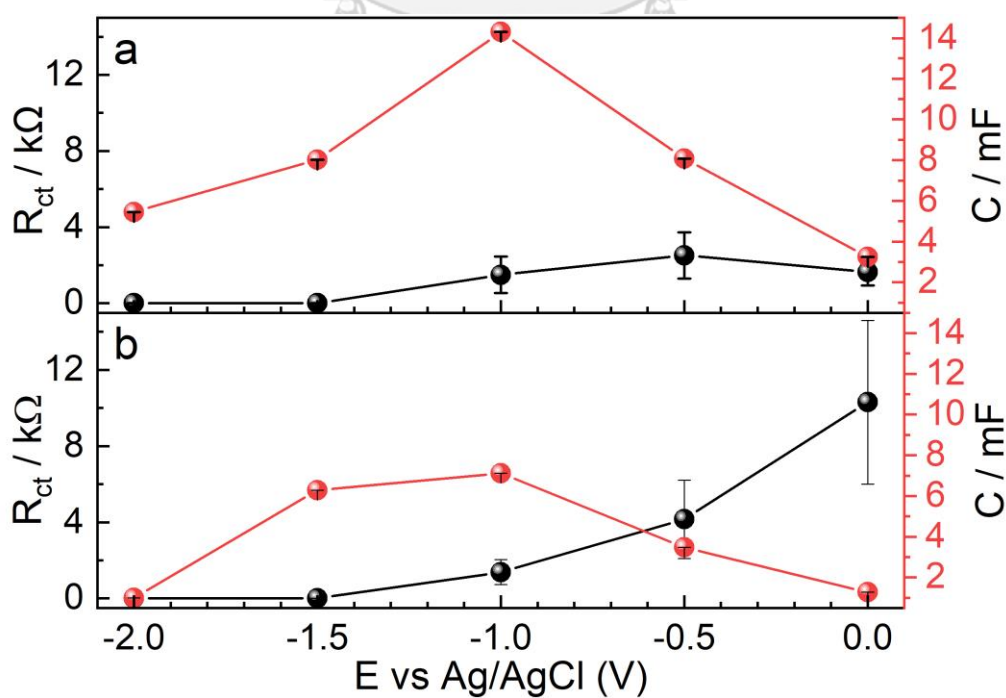


Figure 41: R_{ct} and C_p parameters extracted from the EIS measurements using an $R_s(R_{ct}C_p)$ equivalent circuit. a) in 1.0 M KOH. b) in 1.0 M KOH + 400 μ M NB.

4.3.3.3 The impedance of HEOs

The surface properties of the electrodes were measured using electrochemical impedance spectroscopy (EIS) to determine the surface dynamics and the possible reaction on the surface [72,133]. Figure 42 depicts the EIS spectra obtained at -1.0 V and -1.4 V in 1.0 M KOH and 1.0 M KOH + 400 μ M solutions and the equivalent circuits used to fit the data. Figure 42a shows the results obtained at the lowest applied potential used (-1.0 V). Under this condition, there was a low overpotential for the nitrobenzene reduction (-0.1 V), and the hydrogen evolution reaction contribution was not measurable. All the electrodes showed a mostly resistive behavior with a distorted semi-circle shape, as the result of pseudo-capacitive effects probably caused by the irregularities of the surface, causing a deviation from the ideal behavior[145]. The EIS measurements of the HEOs in the presence of NB, shown in Figure 42b, the uncompensated resistance (R_s), and the polarization resistance, shifted to lower values. This change was attributed to the adsorption of the NB on the electrodes having a reducing effect, improving the electron transfer rate[133]. This behavior was also observed in the cyclic voltammetry experiments when NB was added (Figure 37)

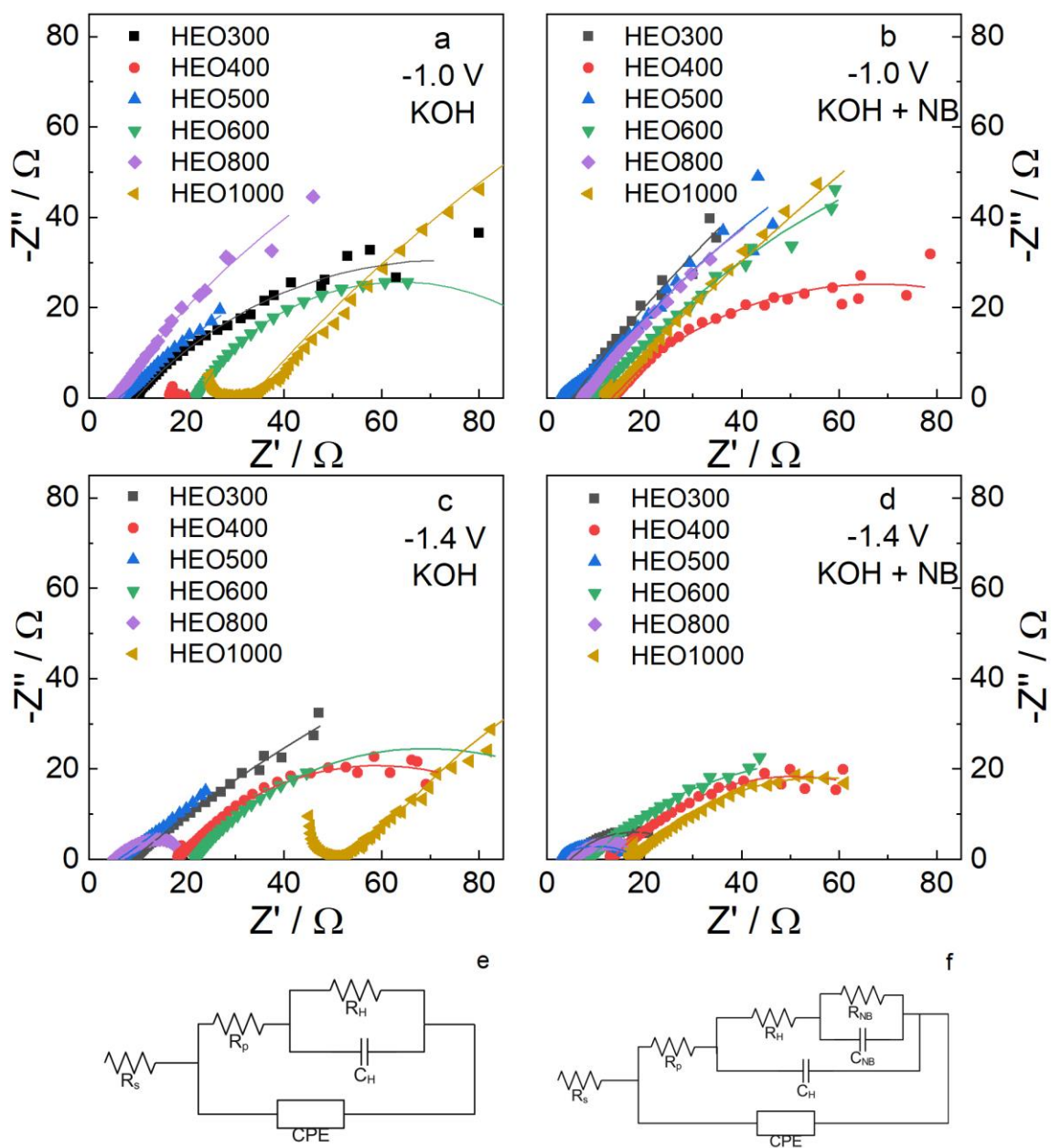


Figure 42: Impedance results for HEOs sintered at different temperatures measured in 1.0 M KOH (a), (c), and 1.0 M KOH + 400 μ M NB (b), (d). Symbol (experimental data), continuous line (numerical fitting) using equivalent circuits (e) and (f).

Figure 42c and 42d present the EIS results from the HEOs evaluated at -1.4 V in the absence and presence of NB, respectively. A decrease in the resistive behavior of the electrodes (R_s and R_p) was observed in both conditions. This decrease in the resistive behavior of the electrodes is consistent with the increase in the applied driving force, enhancing the kinetics of the electrochemical reactions. Considering the surface

reactions, two different equivalent circuits were used to fit the impedance results. In the case of the measurements in KOH, two time constants were used (Figure 42e)[134,145]. The uncompensated resistance of the solution, polarization resistance, hydrogen reduction resistance, surface roughness effects, and the surface adsorption of hydrogen were labeled as R_s , R_p , R_H , CPE, and C_H , respectively. In the case of the experiments in the presence of KOH + NB, a third time constant was included to account for the simultaneous surface reaction of nitrobenzene (Figure 42f) [134,145], where R_{NB} and C_{NB} correspond to the direct reduction of nitrobenzene and the surface adsorption, respectively. In both cases, the equivalent circuits were derived from the proposed kinetic mechanism where an adsorption equilibrium (two in the presence of nitrobenzene) must be faster than the surface reaction. Second, Langmuir-type adsorption without lateral interactions was assumed. Finally, a high concentration of the adsorbed species in the solution (H_2O and NB) and a sufficiently small current to make sure the system remains unchanged during the measurements were used. A detailed derivation of the mathematical expressions used to select the equivalent circuit was reported by Lasia[145].

The results of the fitting for the EIS measurements performed at -1.4 V in KOH + NB solution are shown in Table 9. Among the HEOs, the HEO800 showed the lowest R_{NB} value, while the HEO400 presented the highest one; in the case of the R_H , the HEO800 also showed the lowest value while the HEO400 reported the highest one. The Pt/C electrodes showed the lowest resistance to the hydrogen and NB reduction, this is consistent with the highly catalytic nature of the Pt/C. These results indicate that the electrochemical reactions of the hydrogen evolution and direct reduction of NB are favored on the HEO800 catalyst, while the HEO400 seemed to be the less active material.

Table 9: Fitting parameters extracted from EIS analysis of figure 42d.

| Material | E_{app} (V) | R_s (Ω) | R_p (Ω) | CPE* | | C_{DL} (mF) | R_H (Ω) | C_H (mF) | R_{NB} (Ω) | C_{NB} (mF) |
|----------------|------------------|-----------------------|-----------------------|-----------------|------|------------------|-----------------------|---------------|--------------------------|------------------|
| | | | | Y (mMho*s^N) | N | | | | | |
| HEO300 | -1.4 | 4.8 | 2.1 | 32.7 | 0.52 | 9.56 | 9.2 | 0.08 | 15.5 | 2.80 |
| HEO400 | -1.4 | 13.1 | 20.4 | 11.7 | 0.54 | 1.59 | 35.0 | 0.14 | 22.2 | 2.31 |
| HEO500 | -1.4 | 2.7 | 1.1 | 18.7 | 0.41 | 1.16 | 9.0 | 0.12 | 16.5 | 0.21 |
| HEO600 | -1.4 | 7.9 | 12.2 | 21.6 | 0.45 | 2.59 | 24.6 | 0.57 | 8.6 | 1.64 |
| HEO800 | -1.4 | 5.4 | 5.0 | 15.5 | 0.53 | 2.34 | 4.0 | 0.56 | 6.07 | 4.07 |
| HEO1000 | -1.4 | 17.1 | 15.0 | 13.8 | 0.50 | 1.55 | 28.1 | 0.26 | 19.2 | 6.42 |
| Pt/C | -1.4 | 8.5 | 3.5 | 35.5 | 0.40 | 5.35 | 3.6 | 0.38 | 1.79 | 11.00 |

$$* Z_{CPE} = \frac{1}{Y^N} e^{-\frac{\pi}{2}Ni}$$

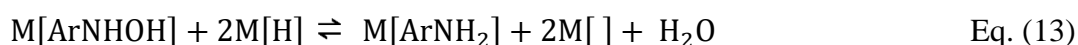
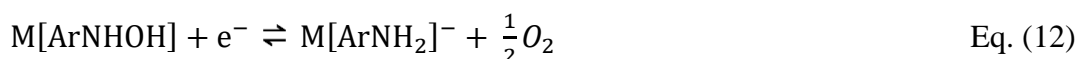
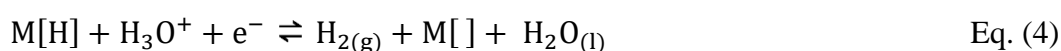
4.4 Electrocatalytic hydrogenation of Nitrobenzene

4.4.1 Hydrogenation over HEAs

The sodium sulfate medium (pH 5) was chosen to study the effect of the applied potential, due to the biggest potential range available before the HER became the main reaction. Figure 43.a-b show the concentrations of nitrobenzene (NB) and aniline (AN), respectively, as a function of time at different applied potentials. A linear behavior in NB conversion was observed, meaning the reaction rate was independent of the concentration. This result corroborates the argument of the surface concentration of adsorbed hydrogen (-H) is the rate-limiting factor, therefore, the adsorption equilibrium and surface reactions were the controlling processes. It is important to notice that the conversion decreased as a function of the applied (negative) potential, while the selectivity towards aniline increased going from 21% at -1.0 V to 97% at -2.0 V (see Figure 43.c). This behavior can be explained by the direct hydrogenation of nitrobenzene on the surface without involving hydrogen transfer, favoring the formation of the partially hydrogenated product at lower overpotentials (-1.0 V). In this regard, a byproduct identified as p-nitrophenol was observed when performing the electrolysis at -1.0 V. This can be the result of OH⁻

species produced near the electrode surface after the formation of the adsorbed -H species that can attack the nucleophilic para position of the nitrobenzene, reducing the selectivity of the process.

In the opposite condition, when the overpotential is high enough to completely activate the hydrogen evolution, the surface hydrogen species are much more active and can attack the nitro group (preferentially adsorbed), favor the extensive hydrogenation, and improve the aniline formation. This higher selectivity had a lower conversion rate because most of the electrons are used in the HER, thus resulting in lower Faradaic efficiency. It is important to note that the reaction rate was not constant in time during the electrolysis. Figure 43.d shows that the aniline production rate or turnover frequency (TOF) decreased in time. As mentioned before, the strong adsorption of the nitrobenzene on the electrode surface hinders the hydrogenation reaction, resulting in a rate drop of about 53% at -1.0 V and 60% at -1.5 V. However, if the hydrogen evolution was activated and the amount of hydrogen in the surface was much higher than the concentration of nitrobenzene (i.e., at -2.0 V), the passivation of the electrode was inhibited, and the aniline production rate was only reduced by 10%. A proposed mechanism for the electrocatalytic hydrogenation of nitrobenzene is represented as follows:



Where ArNO_2 , ArNO , ArNHOH , and ArNH_2 refer to nitrobenzene, nitrosobenzene, phenylhydroxylamine, and aniline, respectively [35,67]. According to this mechanism, the HER (Eq. (3) and (4)) and the direct reduction of nitrobenzene (Eq. (8), (9), and (10)) can lead to the production of undesired byproducts, reducing the selectivity of the electrodes and causing a decrease in the faradaic efficiency.

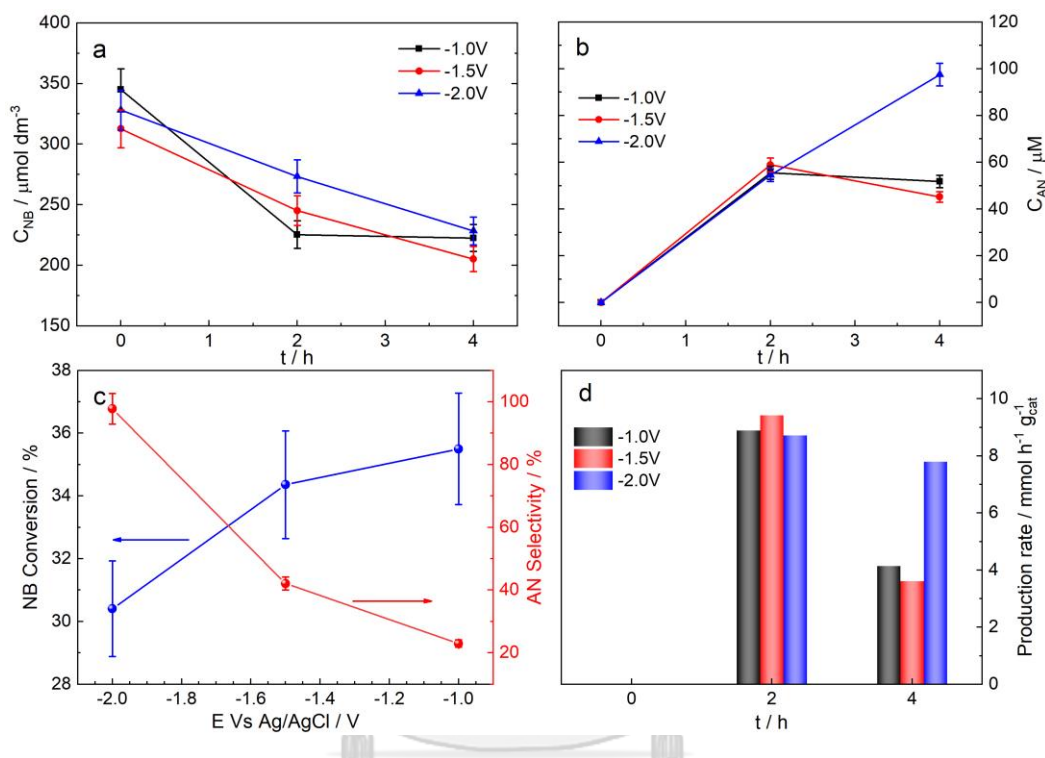


Figure 43: Concentrations of (a) nitrobenzene and (b) aniline measured during the hydrogenation process in 0.1 M Na_2SO_4 solution at different applied potentials. (c) Conversion and selectivity (towards aniline) at different applied potentials. (d) Aniline production rate as a function of time at different applied potentials.

The effect of pH was evaluated by comparing the results of the nitrobenzene hydrogenation at both pH conditions. Figure 44a shows the NB conversion rate and the AN production rate, according to the results previously shown ($E_{\text{app}} = -1.0 \text{ V}$). The higher NB conversion rate in the Na_2SO_4 supporting electrolyte was expected since the direct hydrogenation of nitrobenzene was observed which decreased the selectivity and the production of AN. In an alkaline medium (KOH), this direct hydrogenation was not possible due to the oxidized surface (Figure 31), requiring a more negative potential to activate the hydrogenation process. Figure 44b shows the

conversion and selectivity toward AN production and the results were outstanding, as the selectivity of the process was approximately 93% for the KOH supporting electrolyte, and the conversion was about 24%, surpassing by far the results obtained by a Pt electrode in the same conditions with a selectivity of 34% towards aniline, and a conversion of 23%.

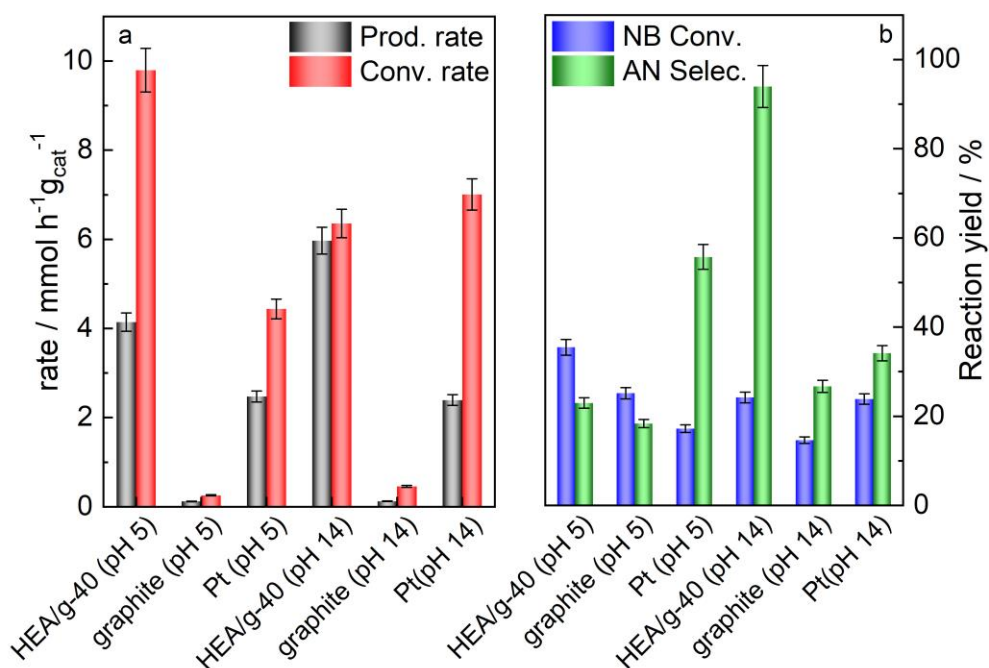


Figure 44: Comparison of results obtained in different media at $E_{app} = -1.0$ V. (a) Aniline (AN) production and nitrobenzene (NB) conversion rates. (b) NB conversion and AN selectivity. (pH 5 in case of Na_2SO_4 and pH 14 for KOH)

CHULALONGKORN UNIVERSITY

These results are like the results obtained at -2.0 V in Na_2SO_4 (conversion 21%, and selectivity 97%). In this regard, it can be concluded that the selectivity of the process is a function of the adsorbed species, i.e. $-\text{H}$ and $-\text{OH}_2$ for acid and basic media, respectively. This can be better understood when comparing the electrochemical behavior of the electrode in both media (Figure 31b) represented in the reversible hydrogen scale. This means that at higher pH values, the adsorbed hydrogen species (produced by the electrolysis of water) are more reactive, improving the reaction rates, conversion, and selectivity. Only when the massive hydrogen evolution is achieved, at pH 14, the surface has the optimal conditions for improving the reaction selectivity towards AN.

4.4.2 Hydrogenation over HEOs

The (electro)catalytic activity of the HEOs was evaluated at two different applied potentials, -1.0 V and -1.4 V. The first hour of electrolysis was analyzed to extract kinetic information, to avoid the interference of by-products. Figure 45a shows the nitrobenzene concentration as a function of time for the hydrogenation experiments performed at -1.4 V, which were fitted by a first-order kinetic model. All the HEOs outperformed the Pt/C electrode in terms of NB conversion and selectivity, this was attributed to the high catalytic nature of Pt/C for the HER reducing the NB efficiency and AN production (Figure 45.b). At constant applied potential condition (constant supplied energy), the adoption of a pseudo-first-order kinetics constant ($k = [s^{-1}]$) to adjust the NB conversion measurements is consistent with the derivation of the kinetic model used to simulate the EIS results; where the inverse of the second time constant ($1/\tau_{NB} = 1/(R_{NB}C_{NB}) = [s^{-1}]$), added to account for the nitrobenzene hydrogenation has the dimensions. If the order of the reaction obtained from the degradation were different from one, a different expression for the mathematical model used for simulating the EIS results should be used to correctly represent the results.

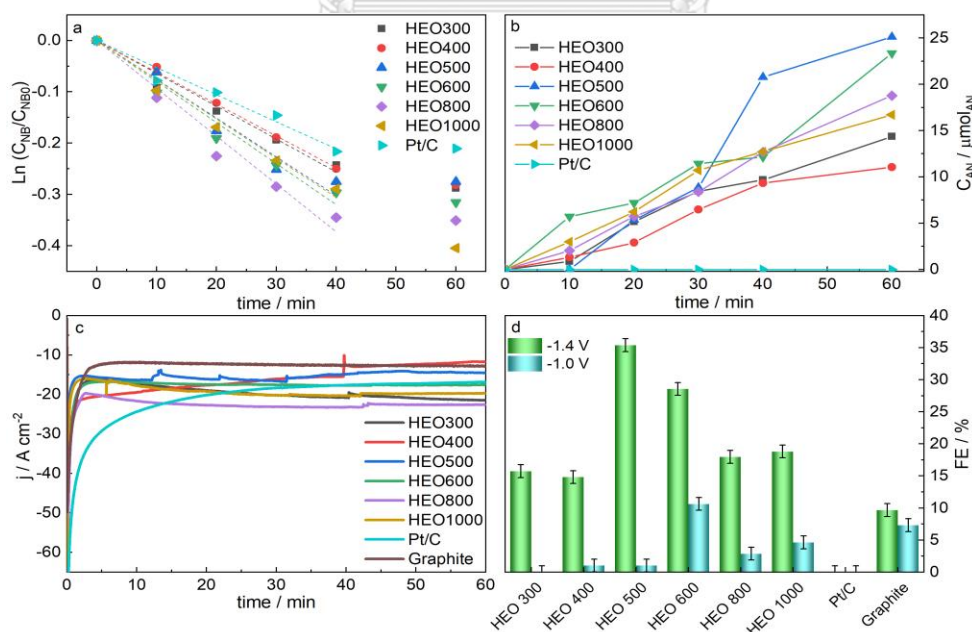


Figure 45: (a) First-order adjustment for the conversion of nitrobenzene. (b) the concentration of aniline vs time. (c) Current density during the hydrogenation reaction.

Figure 45c presents the current vs time profiles obtained during the hydrogenation tests. A strong deactivation of the surface (~60%) was observed for the Pt/C electrode, where the current density decreased from -60 mA cm^{-2} to -20 mA cm^{-2} . The HEO400 showed similar passivating behavior with a decrease in the activity of 50% (-20 mA cm^{-2} to -10 mA cm^{-2}). The rest of the HEO electrodes showed a stable current density, after the first 30 minutes, this was attributed to the reduction of the oxides on the surface. Figure 45d shows the faradaic efficiency (FE), calculated from the AN production results, the differences observed between the two applied potential conditions highlight the effect of the surface concentration of hydrogen on the electrodes for the extensive hydrogenation of nitrobenzene. The HEO500 outperformed the rest of the catalysts exhibiting a stable operation current (-15 mA cm^{-2}) and the highest faradaic efficiency (35%). These results become more important when compared to the benchmark catalyst for hydrogenation (Pt/C). The clean graphite results showed a slight catalytic activity towards nitrobenzene hydrogenation, but the sensitivity with the potential and the low stability makes them poor catalysts as shown in Figure 45d.

Besides the faradaic efficiency and the current density stability, the conversion percentage and the selectivity are two important parameters to evaluate the catalytic activity of different materials. These parameters were calculated according to Eq. (15) and (16):

$$\text{Conversion} = \frac{(C_{NB(0)} - C_{NB(t)})}{C_{NB(0)}} \times 100 \quad \text{Eq.(15)}$$

$$\text{Selectivity} = \frac{C_{AN(t)}}{(C_{NB(0)} - C_{NB(t)})} \times 100 \quad \text{Eq.(16)}$$

Where $C_{NB(0)}$, $C_{NB(t)}$, and $C_{AN(t)}$ represent the initial concentration of nitrobenzene, the concentration of nitrobenzene at different times, and the concentration of aniline in time, respectively.

Figure 46 shows the productivity results obtained from the hydrogenation experiments performed at -1.0 V and -1.4 V . Figure 46a presents the selectivity and

conversion results obtained at -1.0 V, where the hydrogen surface concentration is the lowest. At first sight, the selectivity for AN is remarkably low ($< 15\%$) for all the electrodes used, and the catalyst with the highest selectivity was the HEO1000, which also exhibited the lowest conversion. These results can be explained by the high resistance observed for the direct reduction of the nitrobenzene, due to a low reduction overpotential, and a low concentration of surface hydrogen, inhibiting the surface reaction, from the EIS measurements (Figure 42a and 42b) at this applied potential. On the other hand, the conversion obtained for most of the catalysts was considerably low, with the HEO600 having the maximum conversion (38%) and an extremely low selectivity close to 5%.

In the case of the higher applied potential condition (-1.4 V) in Figure 46, an improvement in AN selectivity and conversion values were observed. A sharp increase in the selectivity was observed for all the catalysts, with the HEO500 standing on a selectivity superior to 45% without using sacrificial agents[146] or precious metals[73]. The conversion also showed a notable improvement, with a rising trend promoted by the increase of the annealing temperature, and the consequent increase of the HEO crystallinity. A very interesting result was obtained for the HEO1000, the selectivity remained almost constant, but the conversion increased from 10% to 25%, when the potential changed from -1.0 V to -1.4 V.

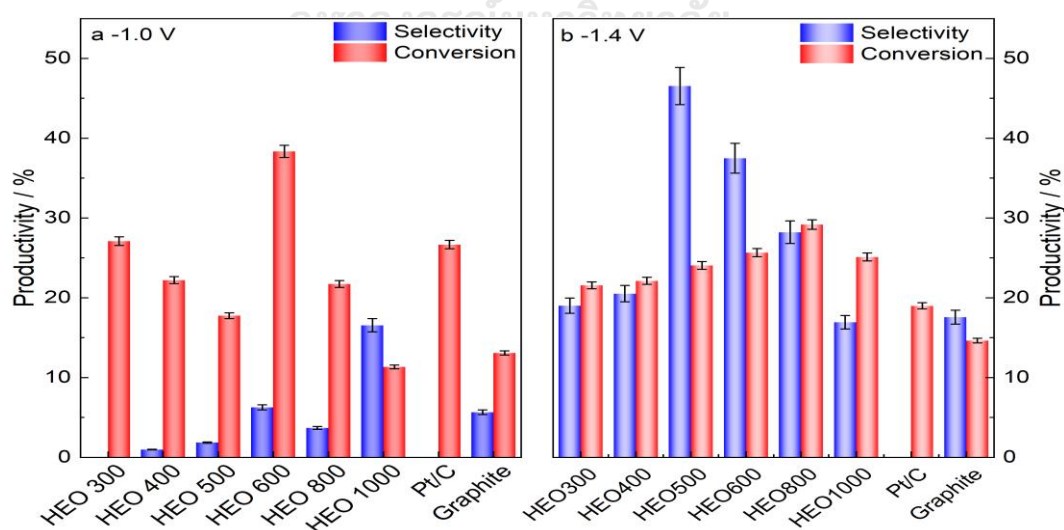


Figure 46: Productivity of nitrobenzene hydrogenation using different HEOs catalysts at (a) -1.0 V and (b) -1.4 V.

To understand the differences in the catalytic performance of each material, we compared the kinetic information obtained from the hydrogenation tests at -1.4 V and calculated the pseudo-first-order [147] reaction constants (k) for each catalyst. These results showed an indirect correlation with the measured resistance to the nitrobenzene hydrogenation (R_{NB}) obtained from the EIS measurements. We found that a lower R_{NB} corresponded to a higher first-order reaction constant as seen in Figure 47. This trend supports the validity of the mechanism adopted, since faster reduction kinetics, could lead to a faster production of intermediates (Eq. 9 – 11), accelerating the overall conversion process, but possibly reducing the aniline formation. The correlation between the kinetic behavior and the adsorption of the NB is highly relevant to properly discussing the surface chemistry of the catalysts and performing adequate comparisons of the catalytic activity. An increasing trend in the adsorption of NB (C_{NB}) was observed following the annealing temperature $\text{HEO}500 < \text{HEO}600 < \text{HEO}800 < \text{HEO}1000$; a similar behavior was observed for the kinetic constant $\text{HEO}500 < \text{HEO}600 < \text{HEO}800$ decreasing sharply for the $\text{HEO}1000$ catalyst. From this relation can be concluded that surface adsorption plays a very important role in the nitrobenzene hydrogenation process and when the adsorption energy is too high the catalysts rapidly passivate.

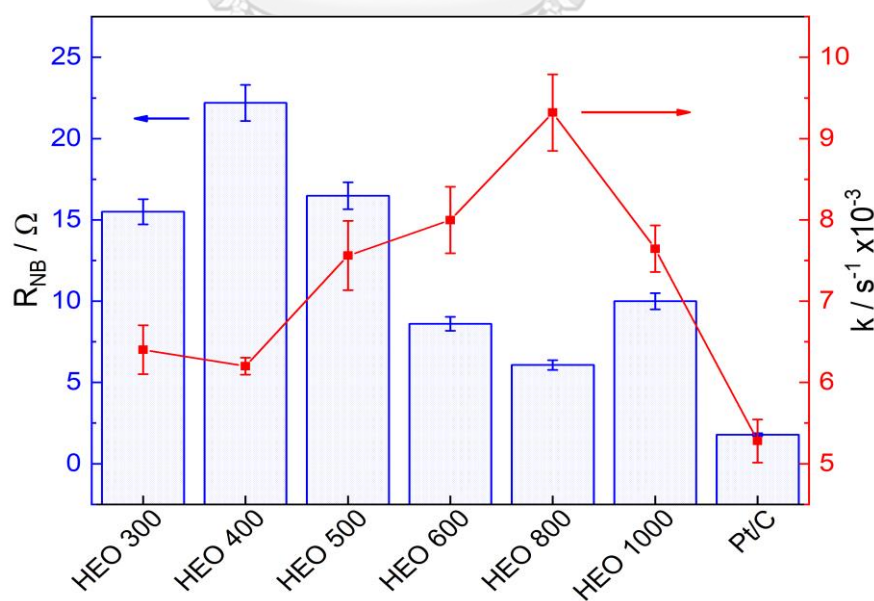


Figure 47: Correlation between resistance to the NB reduction (R_{NB}) and the pseudo-first-order reaction constant for the nitrobenzene hydrogenation at $E_{\text{app}} = -1.4\text{ V}$ (vs Ag/AgCl) in $1\text{ M KOH} + 400\ \mu\text{M NB}$.

On the other hand, the selectivity of the reaction might be controlled by the concentration of the adsorbed species on the surface of the electrodes. Moreover, the complete hydrogenation of nitrobenzene to aniline is a six electron ($6e^-$) and six protons ($6H^+$) transfer, which means that a high concentration of hydrogen on the surface would be required to increase the selectivity of the aniline production. This surface concentration was estimated from the EIS measurements (Table 9) and the surface charge of hydrogen (Q_H) and NB (Q_{NB}) were calculated. Figure 48 shows the correlation between the ratio of the concentrations of H and NB (Q_H/Q_{NB}) and the selectivity of the reaction towards aniline. When the concentration ratio reached its maximum value (HEO500, $Q_H/Q_{NB}= 2$) the selectivity was the highest, while the electrodes with the lowest ratio (HEO1000, $Q_H/Q_{NB}= 0.15$) exhibited the lowest selectivity overall. In the case of the Pt/C electrode, surprising results were obtained, with one of the lowest surface concentrations of H and selectivity of 0%. This can be explained on the base of the fast discharge of hydrogen on the surface of the Pt electrode, promoting the H_2 evolution reaction while suppressing any surface hydrogenation reaction. Furthermore, the effect of the annealing temperature on the physical properties of the catalyst can be summarized by a difference in crystallinity and the crystal size of the materials. This change in the crystallite size (Table 6) showed an indirect effect on the selectivity of the HEO catalysts. The effect of the crystallite size became more important when the calcination temperature was above 500 °C. Especial attention should be paid to the samples synthesized at lower temperatures (HEO300 and HEO400), where a small change in the crystallite size corresponded to a small increase in the selectivity. When the calcination temperature was increased to 500 °C, a sharp increase in selectivity was observed, this sudden change could be attributed to the formation of the spinel structure (Fig. 3) with better redox properties, this has been previously reported for single metal electrodes, especially Cu electrodes[73].

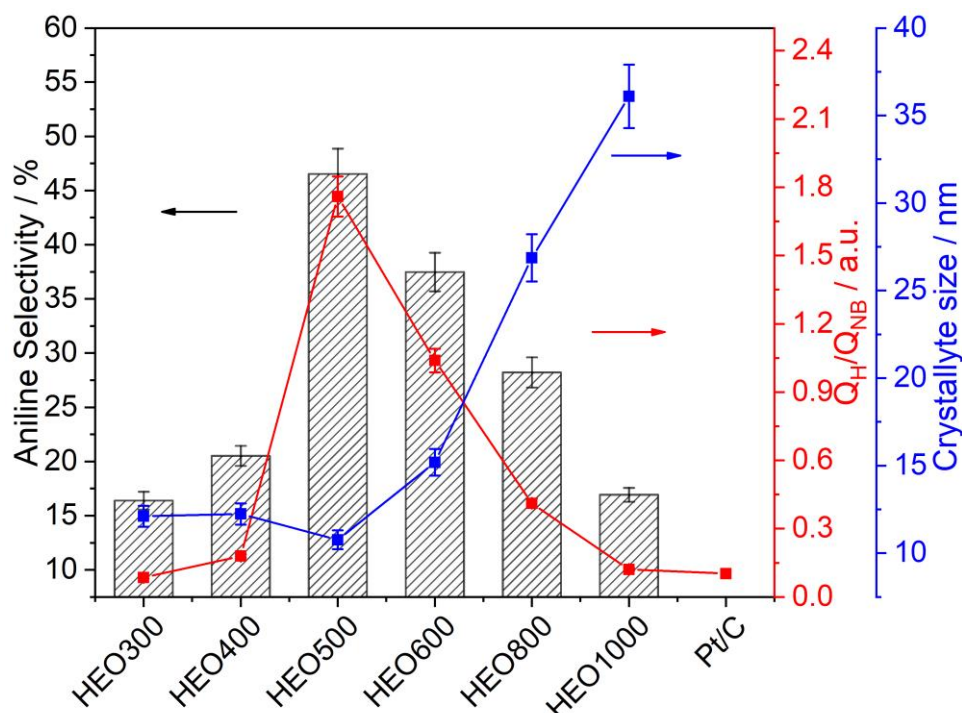


Figure 48: Correlation between the aniline selectivity (%), the ratio of surface concentration of H and NB (Q_H/Q_{NB}), and the crystallite size of the different catalysts.

4.5 Electrocatalytic degradation of nitrobenzene

The catalysts with the highest hydrogenation selectivity, HEO500, was selected to evaluate the effect of the hydrogenation reaction on the nitrobenzene degradation process. Two criteria were used for the selection of the catalyst. First, the selectivity towards nitrobenzene hydrogenation, as mentioned previously, the direct oxidation of nitrobenzene is a complicated process, caused by the high stability of the *nitro* group against radical attacks. In this regard, the aniline is more active and susceptible to being attacked and subsequently degraded. The second criterion to select the HEO500 catalyst is the relatively high overpotential for the oxygen evolution reaction (OER) as seen in Figure 33b. A higher overpotential for OER means a bigger potential window without water oxidation. When the OER is suppressed, the possibilities of directly oxidating nitrobenzene (or aniline) increase, and the energy efficiency increases.

A separate cell setup (Figure 14a) was used to evaluate the direct electrocatalytic oxidation of nitrobenzene. The effect of the applied potential for direct oxidation was

evaluated in a range from 1.3 to 1.7 V vs Ag/AgCl, the result shown in Figure 49 are consistent with the results found in the literature. The direct degradation showed a slight increase from 15.5% at 1.3 V to 18% at 1.7 V, these results indicate that the direct anodic oxidation of nitrobenzene is not favored and to achieve extensive degradation higher oxidation potentials must be used. Using the oxidation potentials of the most common radicals used to degrade organic pollutants in water as a reference, the applied potential for direct oxidation should be above 2.7 V to have a similar energy to the OH^* radical and 3.1 V to be compared with the SO_4^{*-} radical[148].

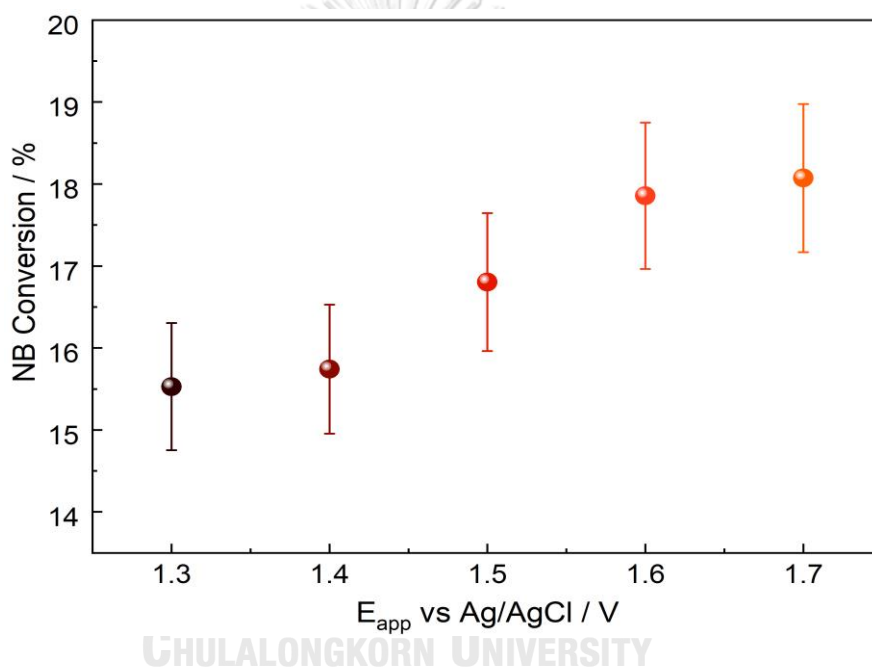


Figure 49: Nitrobenzene conversion at different applied potentials for a separate cell setup in a 1M KOH solution.

Considering direct oxidation results, a different approach was used to improve the degradation process. Using a single compartment setup like the one shown in Figure 14b, the reduction reactions on the counter electrode, necessary to maintain the current flow, can be used to hydrogenate the nitrobenzene to aniline, and then oxidize it on the anode electrode. Using this approach has been very effective for the degradation of resistant pollutants. As a first step, the degradation of nitrobenzene was evaluated in a 1.0 M KOH solution at different applied potentials after purging the solution with N_2 for 30 minutes. A remarkable improvement in the nitrobenzene

conversion was observed at all the applied potentials studied, going from 67% at 1.3 V to 75% at 1.7 V as seen in Figure 50. This improvement evidences the effect of the hydrogenation reaction in the nitrobenzene conversion.

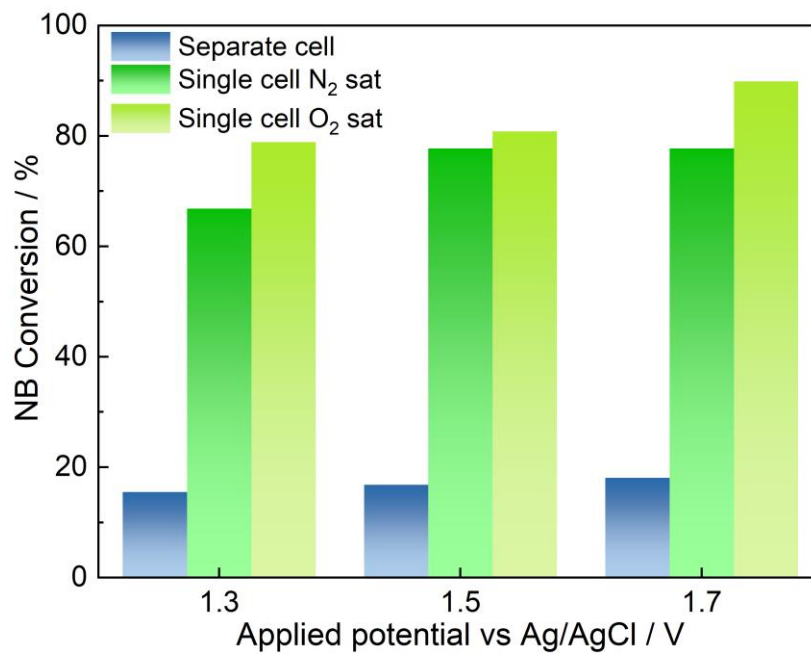


Figure 50: NB conversion vs type of cell setup used for the degradation experiments.

To further study the hydrogenation effect on the degradation processes the solution was saturated with Air instead of N₂, using the same solution used previously. This modification was made to evaluate the effect of oxygen reduction in the hydrogenation process. Oxygen reduction has been extensively studied in the electrochemical field and the results concluded that the presence of oxygen normally reduces the efficiency of the hydrogenation reactions. This effect has been attributed to the adsorption of oxygen on the surface of the catalyst blocking active sites for the desired reaction, the low overpotential for this reaction ($E^0 = 0.40$ V vs RHE), and the sluggish kinetics for the reduction reaction to take place. For all these reasons oxygen is removed from most electrochemical systems, but in real operating conditions for wastewater treatment, the N₂ purging would not be of practical application. The results from the nitrobenzene degradation in the air saturated condition are shown in Figure 50, and the nitrobenzene conversion was slightly improved in comparison to the results with N₂ saturation. The NB conversion increased from 80% at 1.3 V to

90% at 1.7 V. These results provided important information on the surface reactivity of the electrodes, as well as the advantage of using multielement materials with different active sites. An increase in the conversion by including another specie that can adsorb on the surface of the electrode implies that there is no important competition for the adsorption and both reactions can take place without any compromise. The simultaneous reduction of oxygen has another advantage, which is the formation of radical species like the superoxide ($O_2^{\bullet-}$) or the hydroxyl radical (OH^{\bullet}), these two species can accelerate the nitrobenzene degradation and can also promote the aniline, and other by-products oxidation and final mineralization.

To further analyze the electrocatalytic degradation process, the NB conversion rate of the three systems used was calculated and is shown in Figure 51a-c. It is evident that the single chamber system, taking advantage of both electrodes, has a much better performance for conversion. As mentioned previously, the system saturated with Air (O_2) showed the highest reaction rate in all the applied potential conditions. Interestingly the difference between the N_2 saturated system and the Air saturated system decreased considerably at 1.7 V. This change can be attributed to the fast oxygen production in the anodic electrode, rapidly compensating for the amount of dissolved oxygen and increasing the conversion rate. Figure 51d shows the charge efficiencies calculated for the three conditions analyzed; as expected, the highest charge efficiency was obtained at the lowest applied potential, especially because the oxygen evolution was not activated below 1.6 V. When the applied potential was 1.7 V, the oxygen evolution reaction was highly favored and most of the charge was used to oxidize water instead of the nitrobenzene (and by-products). This decrease in the charge efficiency also supports the conclusion that the reaction NB conversion rates at 1.7 V are similar for the N_2 and Air saturated because of the fast production of oxygen on the positively charged electrode.

To evaluate the extension of the degradation, the aniline concentration was followed as a function of time during the degradation experiments. As a principle, the degradation of nitrobenzene is assisted by the hydrogenation to aniline, which in turn can be easily degraded by the produced radicals or by direct oxidation on the electrode.

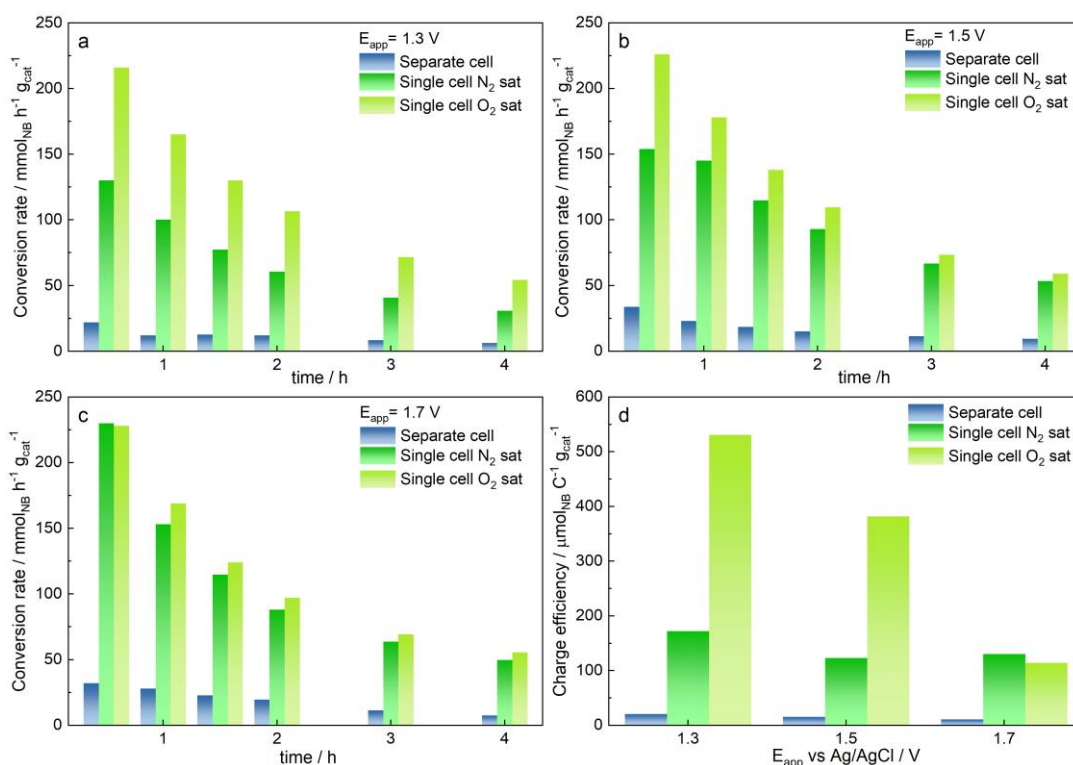


Figure 51: Conversion rate Vs applied potential for the different experimental setups used. a) 1.3 V. b) 1.5 V. c) 1.7 V. d) Charge efficiency of the hydrogenation process in different conditions.

Figure 52 shows the evolution of the concentration of the principal species analyzed, NB and AN. These results clearly show the effect of the hydrogenation reaction and the subsequent degradation of nitrobenzene. The results obtained from the separated chamber cell demonstrate that direct oxidation showed poor results, and the slight increase in the aniline concentration might have been produced by some condensation reactions taking place among reactive oxidation intermediates but always keeping the concentration below 25 μM. In the case of the reaction evaluated with N₂ saturated solution the results are completely different, the aniline concentration follows the expected pattern for an intermediate product, reaching a maximum concentration above 100 μM and then slowly decreasing alongside the concentration of nitrobenzene. The results from the Air saturated experiments showed a similar behavior as the previous one, but the rate of AN degradation was much higher, the maximum concentration measured was below 70 μM and then rapidly decreased like the NB concentration. These results prove that there was no aniline accumulation in

the solution and that an effective degradation of nitrobenzene was achieved using the single compartment setup with Air saturation.

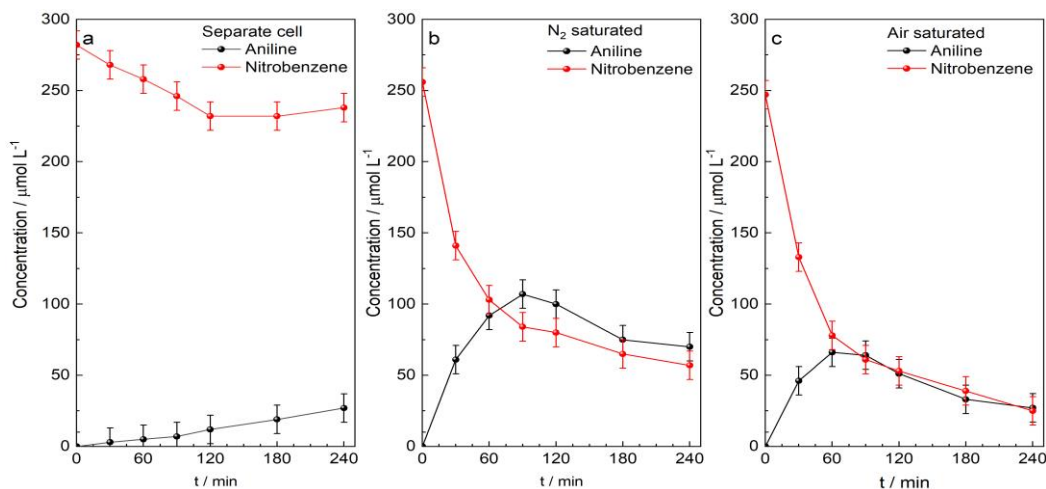


Figure 52: Nitrobenzene and aniline concentration profiles as a function of hydrogenation time in the different experimental setups used. a) Separate cells. b) Single-cell N₂ saturated. c) Single-cell Air saturated E_{app} : 1.7 V vs Ag/AgCl in 1.0 M KOH.

Once the degradation capacity of the HEO500 electrodes was demonstrated, the next step was the evaluation of the applicability of this process and the effect of the initial concentration of nitrobenzene in the solution. The results of the nitrobenzene degradation at different initial concentrations are shown in Figure 53a, a slight decrease in the overall conversion from 92% at 100 μM to 81% at 1000 μM was observed, this result is consistent with previous reports. In this same range of initial concentrations, the conversion rate was calculated and an increase from 1.4 $\mu\text{mol L}^{-1} \text{min}^{-1}$ at 100 μM to 17 $\mu\text{mol L}^{-1} \text{min}^{-1}$ at 1000 μM as shown in Figure 53b. These results show that there is a loss of approximately 10% conversion and a 10-fold increase in the reaction rate when the initial concentration is increased from 100 μM to 1000 μM . The observed trend means there is no surface adsorption limitation, in the range of studied concentrations, and the degradation reaction can be modeled as a pseudo-first-order reaction with a reaction constant of $k = 1.5 \times 10^{-2} \text{ min}^{-1}$ and shows the potential applicability of this process to the wastewater treatment with an extended range of Initial NB concentration with degradation results above 80%.

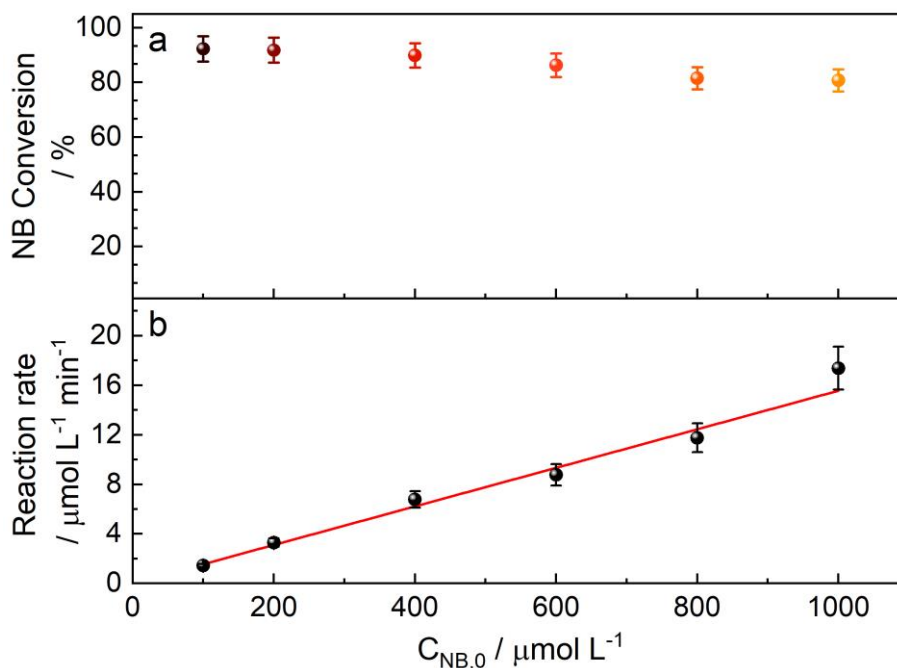


Figure 53: a) Nitrobenzene conversion as a function of initial concentration. b) NB degradation rate at different initial concentrations.

4.6 Catalysts Stability

The catalyst treated at 500 °C (HEO500) showed the best performance for selective hydrogenation of nitrobenzene to aniline, higher selectivity, and hydrogenation yield (46% and 11.2%, respectively). The current stability during the hydrogenation reaction also showed a considerably stable behavior (Figure 45c). To further investigate the stability, the HEO500 was used 5 consecutive times. After each hydrogenation experiment, the electrode was rinsed with DI water, air-dried, and finally dried in the oven at 80 °C for 30 min, after this the electrode was mounted in the electrochemical cell and used as the working electrode. Figure 54 depicts the results from the stability tests, calculated at a constant passed current ($Q = -20$ C), performed on HEO500 electrode by chronoamperometry at $E_{\text{app}} = -1.4$ V (vs Ag/AgCl) in 1 M KOH + 400 μM NB solution for 3600 s in five reaction cycles. The conversion results in Figure 54a show a slow deactivation with the conversion decreasing from 40% to 20% for the fifth consecutive run. In Figure 54b, a notorious change in the selectivity was observed, a drop from 95% to 54% was obtained after

the 5th reaction cycle, and a similar trend was obtained for the faradaic efficiency with a decrease of 50% approximately after the five reaction cycles, as seen in Figure 54c. The current density for each hydrogenation cycle is shown in Figure 54d, where a considerable increase was observed from the first hydrogenation cycle (-3 mA cm^{-2}) until the fourth cycle (-8 mA cm^{-2}) and a final decrease for the fifth cycle (-6 mA cm^{-2}). Another revealing result was found from the analysis of the relaxation current measured before the hydrogenation tests. In this case, the applied voltage used was 0 V (vs Ag/AgCl) to allow the double layer to discharge and to make sure all the measurements started from the same condition. The results in Figure 54e revealed an increase in the oxidation current obtained from the initial condition to the last repeating cycle and some possible explanations were considered.

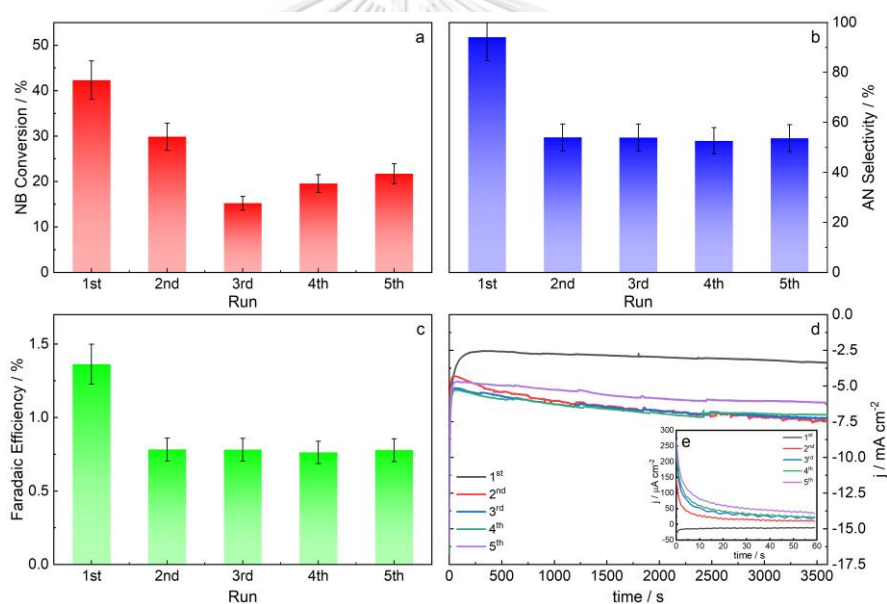


Figure 54: Stability tests of HEO500 electrode in 1.0 M KOH + 400 μM NB at -1.4 V Vs Ag/AgCl. a) Conversion. b) selectivity. c) Faradaic Efficiency. d) Electrode current density during hydrogenation. e) transient current density pre hydrogenation.

One hypothesis is that this increase in the current density could be attributed to the oxidation of any adsorbed species remaining from the consecutive hydrogenation cycles, meaning some of the deactivations can be caused by poisoning of the surface. Another possible reason is the extensive reduction of the surface, during the hydrogenation experiments and then re-oxidized during this pre-treatment. The surface reduction of the surface was evaluated by measuring the open circuit potential

decay (OCPD) of the electrodes after applying a reduction potential. Figure 55 shows the time-resolved evolution of the electrode potential in the open circuit condition. In this condition, the electrons cannot flow through the electrical circuit and the only way to release the energy is by transferring it to any species in the interphase. If there is any electrochemical process that can use those “free” electrons on the surface, the potential of the electrode will stabilize if there are electrons or electron-acceptors available, this relaxation process will make the potential of the electrode “decrease” towards the equilibrium condition. Figure 55b shows the OCPD profile of the HEO1000 electrode, it can be seen how the potential of the electrode rapidly decreases from the applied potential to below -0.3 V in the first 100 s, this potential value corresponds to the reduction potential of the surface, as seen in Figure 37. The fast relaxation of the potential means there is no extensive modification of the surface of the catalyst during the hydrogenation process and the charge can be easily relaxed to the solution and no redox process is present to hold the potential at a higher energy level. A slightly different behavior was observed for the OCPD profile after applying 1.5 V where a longer time is required to reach the relaxation of the energy, this different behavior could be attributed to the presence of adsorbed hydrogen on the surface of the electrode.

Figure 55a shows the OCPD of the HEO500 electrode in the same conditions of applied potential as the HEO1000. In this case, there is a remarkable difference between the relaxation profiles, the profile for the lowest applied potential (-1.0 V) shows a fast relaxation in the first 20 s and stabilizing at -0.5 V for 30 s, after this the potential rapidly decreased towards the equilibrium potential. When the applied potential was increased (-1.1 V and -1.2 V) the OCPD profile showed a considerable difference. In this case, the potential relaxed sharply during the first few seconds, attributed to the relaxation of the double layer, and then an almost-linear decrease of the potential with the time, remaining stable at -0.5 V, the electrode potential remained stable for a longer time when the applied potential was more negative, this could be attributed to the surface reduction, promoted by the presence of oxygen vacancies causing a more extensive modification of the surface than in the case of the HEO1000. Nevertheless, after the reduced surface was re-oxidized, the OCP

decreased towards the equilibrium potential as seen previously. Once the applied potential was considerably higher (-1.3 to -1.5 V) the applied potential presented another stabilization process during the first 20 s (Figure 55a insert) and then relaxed almost linearly towards the -0.5 V. Once the potential reached the stabilization potential remained constant for the rest of the measurement period. This is evidence of an extensive modification of the interface between the surface of the electrode and the solution. This modification could be caused by surface reduction of the oxide, strong hydrogen adsorption, or hydrogen absorption. To properly assess all the changes on the surface an extended time-resolved analysis of element-specific techniques might be required.

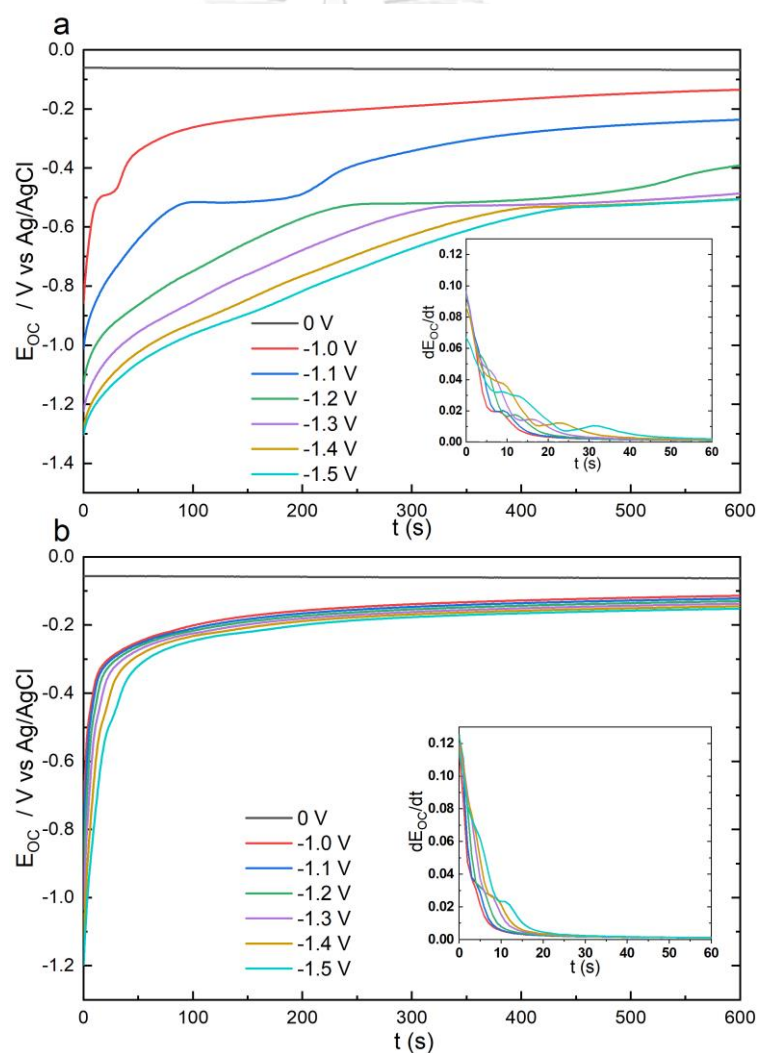


Figure 55: Open circuit potential decay after the applied potential for 200 s in a 1.0 M KOH + 400 μ M NB solution. a) HEO500 electrode. b) HEO1000 electrode.

A third cause of the deactivation observed could be the loss of elements from the surface, especially some segregated phases not included in the major crystalline structure as can be seen in Figure 56, where a loss of the Zn 2p signal and a change in the C 1s was observed after the repeated experiments. This loss of the Zn signal was also corroborated by the SEM-EDX results comparing the fresh and used electrodes (Figure 57 and Table 10), in general, the decrease in the concentration of Zn could be attributed to the dissolution of the segregated phase seen in the XRD measurements (Figure 23). Another cause for the loss of activity during the stability test can be the mechanical separation of the catalyst powder from the surface electrode, caused by the stress produced by the bubbles produced inside the pores of the catalyst causing a mechanical failure of the microstructure. The ink composition was used to prepare the HEOs oxides, which included 5 %wt. Nafion, covered part of the catalyst surface reducing the elemental signals from the XPS measurements, this interference did not allow for the determination of the oxidation state and chemical environment of the elements on the HEO500 electrodes.

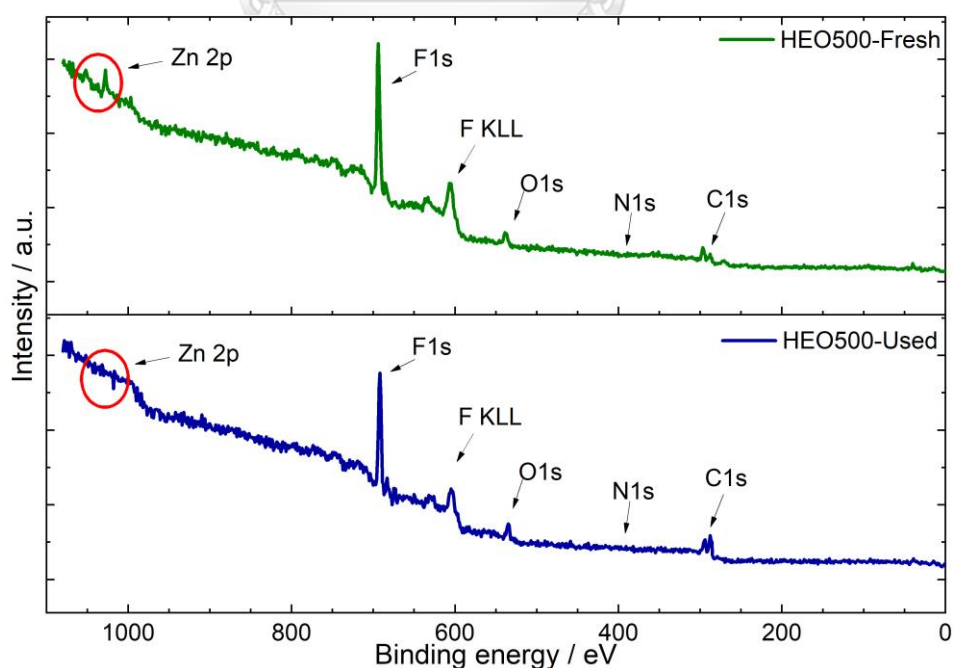


Figure 56: XPS wide scan measurement of a) fresh and b) used HEO500 electrode after the 5th stability experiment.

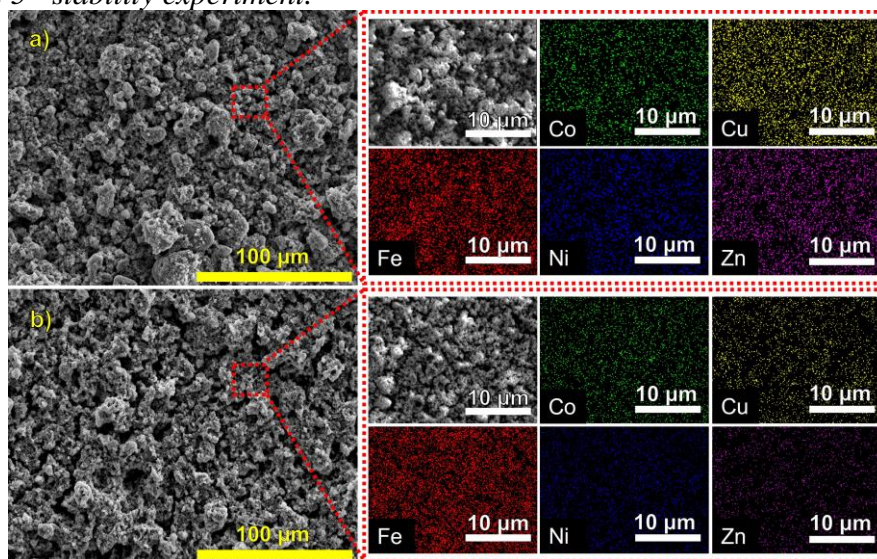


Figure 57: SEM-EDX images measure from the HEO500 electrode a) before the stability tests. b) after the stability tests.

Table 10: Elements concentration on the HEO500 electrode before and after stability tests

| Element | Fresh electrode (At% ± 1) | Used Electrode (At% ± 1) | Variation (ΔAt% ± 2) |
|---------|------------------------------|-----------------------------|-------------------------|
| Fe | 29 | 45 | 16 |
| Co | 5 | 9 | 4 |
| Ni | 9 | 15 | 6 |
| Cu | 31 | 16 | -15 |
| Zn | 26 | 15 | -11 |

To properly address the causes of the deactivation further research must be done, especially evaluating the dynamics of each element during the reaction condition, and the nature of the adsorbed species, ideally using *in-situ* measurements in operation conditions

CHAPTER V:

CONCLUSIONS AND RECOMMENDATIONS

5.1 Conclusions

High entropy materials (HEMs) are promising materials for catalytic applications, and their development has been fast in recent years. Their synthesis, electrocatalytic properties, and stability were studied for the hydrogenation of nitrobenzene using a systematic approach.

High entropy alloys (HEAs) and High entropy oxides (HEOs) were successfully synthesized using simple methods. For the (HEAs) the extension of the hydrogenation is dependent on the hydrogen concentration on the surface of the electrocatalysts, while for the (HEOs) the surface concentration of active hydrogen can change the reduction mechanism for electrocatalytic hydrogenation of nitroarenes.

For the high entropy material (HEM) electrodes, the oxygen reduction and the nitrobenzene hydrogenation processes enhance the degradation of nitrobenzene. The HEM electrodes exhibited deactivation during the nitrobenzene hydrogenation process, and loss of the active surface was the main cause.

5.2 Recommendations

- Evaluate the selective electrocatalytic activity of high entropy materials on different nitroarenes to establish a structure reactivity relationship.
- Use *in situ* and *operando* coupled techniques, like electrochemical FT-IR or electrochemical XAS, to have information on the surface dynamics during the hydrogenation processes.
- Extend the use of high entropy materials with different compositions to study the effect on the hydrogenation mechanisms.
- Evaluate the effect of the temperature in the hydrogenation reactions.
- Evaluate the catalytic activity of different high entropy materials for different reactions of interest like CO₂ reduction, N₂ hydrogenation, or O₂ reduction and evolution reactions.
- Perform theoretical simulations of high entropy materials and evaluate the adsorption properties of the catalysts in applied potential conditions.

REFERENCES



จุฬาลงกรณ์มหาวิทยาลัย
CHULALONGKORN UNIVERSITY

- [1] J. Willbourn, C. Partensky, W.G. Morgan, IARC evaluates printing processes and printing inks, carbon black and some nitro compounds, *Scand. J. Work. Environ. Heal.* 22 (1996) 154–156.
- [2] A. Bharadiya, A. Lakhota, A. Patange, J. Jaju, K. Choraria, Nitrobenzene poisoning presenting as Methemoglobinemia, *Muller J. Med. Sci. Res.* 5 (2014) 185. <https://doi.org/10.4103/0975-9727.135774>.
- [3] D. Gu, N. Shao, Y. Zhu, H. Wu, B. Wang, Solar-driven thermo- and electrochemical degradation of nitrobenzene in wastewater: Adaptation and adoption of solar STEP concept, *J. Hazard. Mater.* 321 (2017) 703–710. <https://doi.org/10.1016/j.jhazmat.2016.09.069>.
- [4] W. Hu, F. Wu, W. Liu, Facile synthesis of Z-scheme $\text{Bi}_2\text{O}_3/\text{Bi}_2\text{WO}_6$ composite for highly effective visible-light-driven photocatalytic degradation of nitrobenzene, *Chem. Phys.* 552 (2022) 111377. <https://doi.org/10.1016/j.chemphys.2021.111377>.
- [5] D. Liu, Z. Liao, Z. Hu, E. Shang, Electrochemical Degradation of Nitrobenzene Wastewater: From Laboratory Experiments to Pilot-Scale Industrial Application, *Catalysts*. 12 (2022). <https://doi.org/10.3390/catal12020190>.
- [6] M. Li, X. Peng, X. Liu, H. Wang, S. Zhang, G. Hu, Single-atom niobium doped BCN nanotubes for highly sensitive electrochemical detection of nitrobenzene, *RSC Adv.* 11 (2021) 28988–28995. <https://doi.org/10.1039/d1ra05517h>.
- [7] T. Wang, Y. Song, H. Ding, Z. Liu, A. Baldwin, I. Wong, H. Li, C. Zhao, Insight into synergies between ozone and in-situ regenerated granular activated carbon particle electrodes in a three-dimensional electrochemical reactor for highly efficient nitrobenzene degradation, *Chem. Eng. J.* 394 (2020) 124852. <https://doi.org/10.1016/j.cej.2020.124852>.
- [8] C. Ratanatamskul, S. Chintitanun, N. Masomboon, M.C. Lu, Inhibitory effect of inorganic ions on nitrobenzene oxidation by fluidized-bed Fenton process, *J. Mol. Catal. A Chem.* 331 (2010) 101–105. <https://doi.org/10.1016/j.molcata.2010.08.007>.
- [9] T. Wang, Y. Song, H. Ding, Z. Liu, A. Baldwin, I. Wong, H. Li, C. Zhao, Insight into synergies between ozone and in-situ regenerated granular activated carbon particle electrodes in a three-dimensional electrochemical reactor for highly efficient nitrobenzene degradation, *Chem. Eng. J.* 394 (2020) 124852. <https://doi.org/10.1016/j.cej.2020.124852>.
- [10] T. Wang, J. Zhang, Y. Song, Z. Liu, H. Ding, C. Zhao, P. Wang, Role of micro-size zero valence iron as particle electrodes in a three-dimensional

- heterogeneous electro-ozonation process for nitrobenzene degradation, *Chemosphere*. 276 (2021) 130264. <https://doi.org/10.1016/j.chemosphere.2021.130264>.
- [11] S. Jiao, Y. Zhao, C. Li, B. Wang, Y. Qu, Recyclable adsorbent of BiFeO₃/Carbon for purifying industrial dye wastewater via photocatalytic reproducible, *Green Energy Environ.* 4 (2019) 66–74. <https://doi.org/10.1016/j.gee.2018.05.001>.
- [12] A. Corma, P. Concepción, P. Serna, A different reaction pathway for the reduction of aromatic nitro compounds on gold catalysts, *Angew. Chemie - Int. Ed.* 46 (2007) 7266–7269. <https://doi.org/10.1002/anie.200700823>.
- [13] M. Boronat, P. Concepción, A. Corma, S. González, F. Illas, P. Serna, A molecular mechanism for the chemoselective hydrogenation of substituted nitroaromatics with nanoparticles of gold on TiO₂ catalysts: A cooperative effect between gold and the support, *J. Am. Chem. Soc.* 129 (2007) 16230–16237. <https://doi.org/10.1021/ja076721g>.
- [14] F.A. Westerhaus, R. V. Jagadeesh, G. Wienhöfer, M.M. Pohl, J. Radnik, A.E. Surkus, J. Rabeah, K. Junge, H. Junge, M. Nielsen, A. Brückner, M. Beller, Heterogenized cobalt oxide catalysts for nitroarene reduction by pyrolysis of molecularly defined complexes, *Nat. Chem.* 5 (2013) 537–543. <https://doi.org/10.1038/nchem.1645>.
- [15] R. V Jagadesh, A.-E. Surkus, H. Junge, M.-M. Pohl, J. Radink, J. Rabeah, H. Huan, V. Schünemann, A. Brückner, M. Beller, Nanoscale Fe₂O₃-Based Catalysts for Selective Hydrogenation of Nitroarenes to Anilines, *Science* (80-.). 342 (2013) 1583–1587.
- [16] M. Li, F. Cárdenas-Lizana, M.A. Keane, Combined catalytic action of supported Cu and Au in imine production from coupled benzyl alcohol and nitrobenzene reactions, *Appl. Catal. A Gen.* 557 (2018) 145–153. <https://doi.org/10.1016/j.apcata.2018.03.024>.
- [17] C. Wu, C. Zhu, K. Liu, S. Yang, Y. Sun, K. Zhu, Y. Cao, S. Zhang, S. Zhuo, M. Zhang, Q. Zhang, H. Zhang, Nano-pyramid-type Co-ZnO/NC for hydrogen transfer cascade reaction between alcohols and nitrobenzene, *Appl. Catal. B Environ.* 300 (2022) 120288. <https://doi.org/10.1016/j.apcatb.2021.120288>.
- [18] J. Song, Z.F. Huang, L. Pan, K. Li, X. Zhang, L. Wang, J.J. Zou, Review on selective hydrogenation of nitroarene by catalytic, photocatalytic and electrocatalytic reactions, *Appl. Catal. B Environ.* 227 (2018) 386–408. <https://doi.org/10.1016/j.apcatb.2018.01.052>.

- [19] J.T. Stock, Fritz Haber (1868-1934) and the electroreduction of nitrobenzene, *J. Chem. Educ.* 65 (1988) 337–338. <https://doi.org/10.1021/ed065p337>.
- [20] J.A. Makaryan, V.I. Savchenko, n-Arylhydroxylamines Transformation in the Presense of Heterogeneous Catalysts, *Stud. Surf. Sci. Catal.* 75 (1993) 2439–2442. [https://doi.org/10.1016/S0167-2991\(08\)64319-0](https://doi.org/10.1016/S0167-2991(08)64319-0).
- [21] F. Visentin, G. Puxty, O.M. Kut, K. Hungerbühler, Study of the hydrogenation of selected nitro compounds by simultaneous measurements of calorimetric, FT-IR, and gas-uptake signals, *Ind. Eng. Chem. Res.* 45 (2006) 4544–4553. <https://doi.org/10.1021/ie0509591>.
- [22] T. Erdey-Grúz, M. Volmer, Zur Theorie der Wasserstoff Überspannung, *Zeitschrift Für Phys. Chemie.* 150A (1930) 203–213. <https://doi.org/10.1515/zpch-1930-15020>.
- [23] J. Tafel, Über die Polarisation bei kathodischer Wasserstoffentwicklung, *Z. Phys. Chem.* 50 (1905) 641–712. <https://doi.org/10.1515/zpch-1905-5043>.
- [24] S. Trasatti, Work function, electronegativity, and electrochemical behaviour of metals. III. Electrolytic hydrogen evolution in acid solutions, *J. Electroanal. Chem.* 39 (1972) 163–184. [https://doi.org/10.1016/S0022-0728\(72\)80485-6](https://doi.org/10.1016/S0022-0728(72)80485-6).
- [25] G. Zhao, K. Rui, S.X. Dou, W. Sun, Heterostructures for electrochemical hydrogen evolution reaction: A review, *Adv. Funct. Mater.* 28 (2018) 1–26. <https://doi.org/10.1002/adfm.201803291>.
- [26] F. Safizadeh, E. Ghali, G. Houlachi, Electrocatalysis developments for hydrogen evolution reaction in alkaline solutions - A Review, *Int. J. Hydrogen Energy.* 40 (2015) 256–274. <https://doi.org/10.1016/j.ijhydene.2014.10.109>.
- [27] H.A. Hansen, V. Viswanathan, J.K. Nørskov, Unifying kinetic and thermodynamic analysis of 2 e⁻ and 4 e⁻ reduction of oxygen on metal surfaces, *J. Phys. Chem. C.* 118 (2014) 6706–6718. <https://doi.org/10.1021/jp4100608>.
- [28] C. Tsai, K. Chan, J.K. Nørskov, F. Abild-Pedersen, Theoretical insights into the hydrogen evolution activity of layered transition metal dichalcogenides, *Surf. Sci.* 640 (2015) 133–140. <https://doi.org/10.1016/j.susc.2015.01.019>.
- [29] Z.W. She, J. Kibsgaard, C.F. Dickens, I. Chorkendorff, J.K. Nørskov, T.F. Jaramillo, Combining theory and experiment in electrocatalysis: Insights into materials design, *Science* (80-.). 355 (2017). <https://doi.org/10.1126/science.aad4998>.
- [30] V. Márquez, J.S. Santos, J.G. Buijnsters, S. Praserthdam, P. Praserthdam, Simple, controllable and environmentally friendly synthesis of FeCoNiCuZn-

based high-entropy alloy (HEA) catalysts, and their surface dynamics during nitrobenzene hydrogenation, *Electrochim. Acta.* 410 (2022).
<https://doi.org/10.1016/j.electacta.2022.139972>.

- [31] D. Carvajal, R. Arcas, C.A. Mesa, S. Giménez, F. Fabregat-Santiago, E. Mas-Marzá, Role of Pd in the Electrochemical Hydrogenation of Nitrobenzene Using CuPd Electrodes, *Adv. Sustain. Syst.* 6 (2022) 1–10.
<https://doi.org/10.1002/adsu.202100367>.
- [32] Y. Yang, J. Jiang, X. Lu, J. Ma, Y. Liu, Production of Sulfate Radical and Hydroxyl Radical by Reaction of Ozone with Peroxymonosulfate: A Novel Advanced Oxidation Process, *Environ. Sci. Technol.* 49 (2015) 73307339.
<https://doi.org/10.1021/es506362e>.
- [33] B. Yang, Q. Ma, X. Ren, X. Peng, H. Wang, L. Li, J. Hao, The Journal of Supercritical Fluids Supercritical Water Oxidation of Aniline, Nitrobenzene, and Indole: Effect of Catalysts on Nitrogen Conversion Mechanism, *J. Supercrit. Fluids.* 188 (2022) 105680.
<https://doi.org/10.1016/j.supflu.2022.105680>.
- [34] D. Gu, N. Shao, Y. Zhu, H. Wu, B. Wang, Solar-driven thermo- and electrochemical degradation of nitrobenzene in wastewater: Adaptation and adoption of solar STEP concept, *J. Hazard. Mater. J.* 321 (2017) 703–710.
<https://doi.org/10.1016/j.jhazmat.2016.09.069>.
- [35] S. Nellaiappan, N.K. Katiyar, R. Kumar, A. Parui, K.D. Malviya, K.G. Pradeep, A.K. Singh, S. Sharma, C.S. Tiwary, K. Biswas, High-Entropy Alloys as Catalysts for the CO₂ and CO Reduction Reactions: Experimental Realization, *ACS Catal.* 10 (2020) 3658–3663.
<https://doi.org/10.1021/acscatal.9b04302>.
- [36] J.K. Pedersen, T.A.A. Batchelor, A. Bagger, J. Rossmeisl, High-entropy alloys as catalysts for the CO₂ and CO reduction reactions, *ACS Catal.* 10 (2020) 2169–2176. <https://doi.org/10.1021/acscatal.9b04343>.
- [37] X. Wang, W. Guo, Y. Fu, High-entropy alloys: Emerging materials for advanced functional applications, *J. Mater. Chem. A.* 9 (2021) 663–701.
<https://doi.org/10.1039/d0ta09601f>.
- [38] J.W. Yeh, S.K. Chen, S.J. Lin, J.Y. Gan, T.S. Chin, T.T. Shun, C.H. Tsau, S.Y. Chang, Nanostructured high-entropy alloys with multiple principal elements: Novel alloy design concepts and outcomes, *Adv. Eng. Mater.* 6 (2004) 299–303. <https://doi.org/10.1002/adem.200300567>.
- [39] X. Xu, Y. Guo, B.P. Bloom, J. Wei, H. Li, H. Li, Y. Du, Z. Zeng, L. Li, D.H.

- Waldeck, Elemental core level shift in high entropy alloy nanoparticles via X-ray photoelectron spectroscopy analysis and first-principles calculation, *ACS Nano*. 14 (2020) 17704–17712. <https://doi.org/10.1021/acsnano.0c09470>.
- [40] W. Zhang, P.K. Liaw, Y. Zhang, Science and technology in high-entropy alloys, *Sci. China Mater.* 61 (2018) 2–22. <https://doi.org/https://doi.org/10.1007/s40843-017-9195-8>.
- [41] B. Cantor, I.T.H. Chang, P. Knight, A.J.B. Vincent, Microstructural development in equiatomic multicomponent alloys, *Mater. Sci. Eng. A*. 375–377 (2004) 213–218. <https://doi.org/10.1016/j.msea.2003.10.257>.
- [42] T. Löffler, A. Ludwig, J. Rossmeisl, W. Schuhmann, What Makes High-Entropy Alloys Exceptional Electrocatalysts?, *Angew. Chemie - Int. Ed.* 60 (2021) 26894–26903. <https://doi.org/10.1002/anie.202109212>.
- [43] A. Garzón-Manjón, H. Meyer, D. Grochla, T. Löffler, W. Schuhmann, A. Ludwig, C. Scheu, Controlling the amorphous and crystalline state of multinary alloy nanoparticles in an ionic liquid, *Nanomaterials*. 8 (2018) 1–11. <https://doi.org/10.3390/nano8110903>.
- [44] T. Löffler, A. Savan, H. Meyer, M. Meischein, V. Strotkötter, A. Ludwig, W. Schuhmann, Design of complex solid-solution electrocatalysts by correlating configuration, adsorption energy distribution patterns, and activity curves, *Angew. Chemie - Int. Ed.* 59 (2020) 5844–5850. <https://doi.org/10.1002/anie.201914666>.
- [45] T. Löffler, H. Meyer, A. Savan, P. Wilde, A. Garzón Manjón, Y.T. Chen, E. Ventosa, C. Scheu, A. Ludwig, W. Schuhmann, Discovery of a Multinary Noble Metal-Free Oxygen Reduction Catalyst, *Adv. Energy Mater.* 8 (2018) 1–7. <https://doi.org/10.1002/aenm.201802269>.
- [46] C.M. Rost, E. Sachet, T. Borman, A. Moballeggh, E.C. Dickey, D. Hou, J.L. Jones, S. Curtarolo, J.P. Maria, Entropy-stabilized oxides, *Nat. Commun.* 6 (2015). <https://doi.org/10.1038/ncomms9485>.
- [47] R. Wei, K. Zhang, P. Zhao, Y. An, C. Tang, C. Chen, X. Li, X. Ma, Y. Ma, X. Hao, Defect-rich FeCoNiPB/(FeCoNi)₃O_{4-x} high-entropy composite nanoparticles for oxygen evolution reaction: Impact of surface activation, *Appl. Surf. Sci.* 549 (2021) 149327. <https://doi.org/10.1016/j.apsusc.2021.149327>.
- [48] A. Gautam, M.I. Ahmad, Low-temperature synthesis of five component single phase high entropy oxide, *Ceram. Int.* 47 (2021) 22225–22228. <https://doi.org/10.1016/j.ceramint.2021.04.128>.

- [49] B. Talluri, M.L. Aparna, N. Sreenivasulu, S.S. Bhattacharya, T. Thomas, High entropy spinel metal oxide (CoCrFeMnNi)₃O₄ nanoparticles as a high-performance supercapacitor electrode material, *J. Energy Storage*. 42 (2021) 103004. <https://doi.org/10.1016/j.est.2021.103004>.
- [50] V. Márquez, M. Fereidooni, J.S. Santos, S. Praserthdam, P. Praserthdam, Effect of the annealing temperature of multi-elemental oxides (FeCoNiCuZn)_yO_x on the electrocatalytic hydrogenation of nitrobenzene at room temperature, *Electrochim. Acta*. 428 (2022) 140975. <https://doi.org/10.1016/j.electacta.2022.140975>.
- [51] J.S. Santos, M. Fereidooni, V. Marquez, M. Arumugam, M. Tahir, S. Praserthdam, P. Praserthdam, Single-step fabrication of highly stable amorphous TiO₂ nanotubes arrays (am-TNTA) for stimulating gas-phase photoreduction of CO₂ to methane, *Chemosphere*. 289 (2022) 133170. <https://doi.org/10.1016/j.chemosphere.2021.133170>.
- [52] J. Huang, P. Wang, P. Li, H. Yin, D. Wang, Regulating electrolytic Fe_{0.5}CoNiCuZn_x high entropy alloy electrodes for oxygen evolution reactions in alkaline solution, *J. Mater. Sci. Technol.* 93 (2021) 110–118. <https://doi.org/10.1016/j.jmst.2021.03.046>.
- [53] A.G. Shard, X-ray photoelectron spectroscopy, Elsevier Inc., 2019. <https://doi.org/10.1016/B978-0-12-814182-3.00019-5>.
- [54] P.S. Bagus, E.S. Ilton, C.J. Nelin, The interpretation of XPS spectra: Insights into materials properties, *Surf. Sci. Rep.* 68 (2013) 273–304. <https://doi.org/10.1016/j.surfrep.2013.03.001>.
- [55] P.S. Bagus, C.J. Nelin, C.R. Brundle, B. Vincent Crist, N. Lahiri, K.M. Rosso, Covalency in Fe₂O₃ and FeO: Consequences for XPS satellite intensity, *J. Chem. Phys.* 153 (2020). <https://doi.org/10.1063/5.0030350>.
- [56] P.S. Bagus, E. Ilton, C.J. Nelin, Extracting chemical information from XPS spectra: A perspective, *Catal. Letters*. 148 (2018) 1785–1802. <https://doi.org/10.1007/s10562-018-2417-1>.
- [57] A. Claypole, J. Claypole, T. Claypole, D. Gethin, L. Kilduff, The effect of plasma functionalization on the print performance and time stability of graphite nanoplatelet electrically conducting inks, *J. Coatings Technol. Res.* 18 (2021) 193–203. <https://doi.org/10.1007/s11998-020-00414-4>.
- [58] M. Trought, I. Wentworth, T. Leftwich, K. Perrine, Effects of wet chemical oxidation on surface functionalization and morphology of highly oriented pyrolytic graphite, *ChemRxiv*. (2020) 1–32.

<https://doi.org/doi:10.26434/chemrxiv.12907604.v1>.

- [59] N.R. Ostyn, B. Thijs, J.A. Steele, S.P. Sree, W. Wangermez, J. Teyssandier, M.M. Minjauw, J. Li, C. Detavernier, M.B.J. Roeffaers, S. De Feyter, J.A. Martens, Controlled graphite surface functionalization using contact and remote photocatalytic oxidation, *Carbon N. Y.* 172 (2021) 637–646. <https://doi.org/10.1016/j.carbon.2020.10.069>.
- [60] S.H. Albedwawi, A. AlJaberi, G.N. Haidemenopoulos, K. Polychronopoulou, High entropy oxides-exploring a paradigm of promising catalysts: A review, *Mater. Des.* 202 (2021) 109534. <https://doi.org/10.1016/j.matdes.2021.109534>.
- [61] G.R. Rao, M.M. Ali, S. Roychowdhury, L. Prasad, Promising oxygen storage capacity of equimolar high entropy transition metal oxide (MgCoNiCuZn)O, *Mater. Lett.* 304 (2021) 130635. <https://doi.org/10.1016/j.matlet.2021.130635>.
- [62] A.V. Saghir, S.M. Beidokhti, J.V. Khaki, A. Salimi, One-step synthesis of single-phase (Co, Mg, Ni, Cu, Zn) O High entropy oxide nanoparticles through SCS procedure: Thermodynamics and experimental evaluation, *J. Eur. Ceram. Soc.* 41 (2021) 563–579. <https://doi.org/10.1016/j.jeurceramsoc.2020.08.044>.
- [63] T.H. Chou, J.C. Huang, C.H. Yang, S.K. Lin, T.G. Nieh, Consideration of kinetics on intermetallics formation in solid-solution high entropy alloys, *Acta Mater.* (2020). <https://doi.org/10.1016/j.actamat.2020.05.015>.
- [64] G. Anand, A.P. Wynn, C.M. Handley, C.L. Freeman, Phase stability and distortion in high-entropy oxides, *Acta Mater.* 146 (2018) 119–125. <https://doi.org/10.1016/j.actamat.2017.12.037>.
- [65] R. Reske, H. Mistry, F. Behafarid, B. Roldan Cuenya, P. Strasser, Particle size effects in the catalytic electroreduction of CO₂ on Cu nanoparticles, *J. Am. Chem. Soc.* 136 (2014) 6978–6986. <https://doi.org/10.1021/ja500328k>.
- [66] G. Santhosh, G.P. Nayaka, A.S. Bhatt, Ultrahigh capacitance of NiCo₂O₄/CeO₂ mixed metal oxide material for supercapacitor applications, *J. Alloys Compd.* 899 (2022) 163312. <https://doi.org/10.1016/j.jallcom.2021.163312>.
- [67] K. Kannan, D. Radhika, K.R. Reddy, A. V. Raghu, K. Sadadivuni, G. Palani, K. Gurushankar, Gd³⁺ and Y³⁺ co-doped mixed metal oxide nanohybrids for photocatalytic and antibacterial applications, *Nano Express.* (2021). <https://doi.org/10.1088/2632-959x/abdd87>.
- [68] A.A. Ali, I.S. Ahmed, E.M. Elfiky, Auto-combustion Synthesis and Characterization of Iron Oxide Nanoparticles (α -Fe₂O₃) for Removal of Lead

- Ions from Aqueous Solution, *J. Inorg. Organomet. Polym. Mater.* 31 (2021) 384–396. <https://doi.org/10.1007/s10904-020-01695-3>.
- [69] H. Zhu, H. Xie, Y. Zhao, S. Dai, M. Li, X. Wang, Structure and magnetic properties of a class of spinel high-entropy oxides, *J. Magn. Magn. Mater.* 535 (2021) 168063. <https://doi.org/10.1016/j.jmmm.2021.168063>.
- [70] H. Wang, C. Zhen, D. Xu, X. Wu, L. Ma, D. Zhao, D. Hou, Multiple magnetic phase transitions in $\text{Ni}_x\text{Mn}_{1-x}\text{Co}_2\text{O}_4$, *Ceram. Int.* 46 (2020) 16126–16134. <https://doi.org/10.1016/j.ceramint.2020.03.165>.
- [71] H. Qiao, X. Wang, Q. Dong, H. Zheng, G. Chen, M. Hong, C.P. Yang, M. Wu, K. He, L. Hu, A high-entropy phosphate catalyst for oxygen evolution reaction, *Nano Energy.* 86 (2021) 106029. <https://doi.org/10.1016/j.nanoen.2021.106029>.
- [72] D. Flak, Q. Chen, B.S. Mun, Z. Liu, M. Rekas, A. Braun, In situ ambient pressure XPS observation of surface chemistry and electronic structure of α - Fe_2O_3 and γ - Fe_2O_3 nanoparticles, *Appl. Surf. Sci.* 455 (2018) 1019–1028. <https://doi.org/10.1016/j.apsusc.2018.06.002>.
- [73] Q.T. Trinh, K. Bhola, P.N. Amaniampong, F. Jérôme, S.H. Mushrif, Synergistic Application of XPS and DFT to Investigate Metal Oxide Surface Catalysis, *J. Phys. Chem. C.* 122 (2018) 22397–22406. <https://doi.org/10.1021/acs.jpcc.8b05499>.
- [74] Y. Wang, Z. Chen, P. Han, Y. Du, Z. Gu, X. Xu, G. Zheng, Single-Atomic Cu with Multiple Oxygen Vacancies on Ceria for Electrocatalytic CO_2 Reduction to CH_4 , *ACS Catal.* 8 (2018) 7113–7119. <https://doi.org/10.1021/acscatal.8b01014>.
- [75] K. Zhu, F. Shi, X. Zhu, W. Yang, The roles of oxygen vacancies in electrocatalytic oxygen evolution reaction, *Nano Energy.* 73 (2020) 104761. <https://doi.org/10.1016/j.nanoen.2020.104761>.
- [76] S. Chen, D. Huang, D. Liu, H. Sun, W. Yan, J. Wang, M. Dong, X. Tong, W. Fan, Hollow and porous NiCo_2O_4 nanospheres for enhanced methanol oxidation reaction and oxygen reduction reaction by oxygen vacancies engineering, *Appl. Catal. B Environ.* 291 (2021) 120065. <https://doi.org/10.1016/j.apcatb.2021.120065>.
- [77] Y. Liu, P. Deng, R. Wu, X. Zhang, C. Sun, H. Li, Oxygen vacancies for promoting the electrochemical nitrogen reduction reaction, *J. Mater. Chem. A.* 9 (2021) 6694–6709. <https://doi.org/10.1039/d0ta11522c>.

- [78] M.C. Biesinger, B.P. Payne, A.P. Grosvenor, L.W.M. Lau, A.R. Gerson, R.S.C. Smart, Resolving surface chemical states in XPS analysis of first row transition metals, oxides and hydroxides: Cr, Mn, Fe, Co and Ni, *Appl. Surf. Sci.* 257 (2011) 2717–2730. <https://doi.org/10.1016/j.apsusc.2010.10.051>.
- [79] L. Lukashuk, K. Föttinger, E. Kolar, C. Rameshan, D. Teschner, M. Hävecker, A. Knop-Gericke, N. Yigit, H. Li, E. McDermott, M. Stöger-Pollach, G. Rupprechter, Operando XAS and NAP-XPS studies of preferential CO oxidation on Co_3O_4 and $\text{CeO}_2\text{-Co}_3\text{O}_4$ catalysts, *J. Catal.* 344 (2016) 1–15. <https://doi.org/10.1016/j.jcat.2016.09.002>.
- [80] J. Zhong, Y. Zeng, M. Zhang, W. Feng, D. Xiao, J. Wu, P. Chen, M. Fu, D. Ye, Toluene oxidation process and proper mechanism over Co_3O_4 nanotubes: Investigation through in-situ DRIFTS combined with PTR-TOF-MS and quasi in-situ XPS, *Chem. Eng. J.* 397 (2020) 125375. <https://doi.org/10.1016/j.cej.2020.125375>.
- [81] M.C. Biesinger, L.W.M. Lau, A.R. Gerson, R.S.C. Smart, Resolving surface chemical states in XPS analysis of first row transition metals, oxides and hydroxides: Sc, Ti, V, Cu and Zn, *Appl. Surf. Sci.* 257 (2010) 887–898. <https://doi.org/10.1016/j.apsusc.2010.07.086>.
- [82] V.K. Soni, S. Sanyal, S.K. Sinha, Investigation of phase stability of novel equiatomic FeCoNiCuZn based-high entropy alloy prepared by mechanical alloying, *AIP Conf. Proc.* 1953 (2018). <https://doi.org/10.1063/1.5032588>.
- [83] Y. Zhu, C. Huang, C. Li, M. Fan, K. Shu, H.C. Chen, Strong synergetic electrochemistry between transition metals of A phase Ni–Co–Mn hydroxide contributed superior performance for hybrid supercapacitors, *J. Power Sources.* 412 (2019) 559–567. <https://doi.org/10.1016/j.jpowsour.2018.11.080>.
- [84] T.C. Chou, C.C. Chang, H.L. Yu, W.Y. Yu, C.L. Dong, J.J. Velasco-Vélez, C.H. Chuang, L.C. Chen, J.F. Lee, J.M. Chen, H.L. Wu, Controlling the oxidation state of the Cu electrode and reaction intermediates for electrochemical CO_2 reduction to ethylene, *J. Am. Chem. Soc.* 142 (2020) 2857–2867. <https://doi.org/10.1021/jacs.9b11126>.
- [85] Y.X. Chen, S.P. Chen, Z.Y. Zhou, N. Tian, Y.X. Jiang, S.G. Sun, Y. Ding, L.W. Zhong, Tuning the shape and catalytic activity of Fe nanocrystals from rhombic dodecahedra and tetragonal bipyramids to cubes by electrochemistry, *J. Am. Chem. Soc.* 131 (2009) 10860–10862. <https://doi.org/10.1021/ja904225q>.
- [86] Y. Zhang, Z. Chen, H. Qiu, W. Yang, Z. Zhao, J. Zhao, G. Cui, Pursuit of

reversible Zn electrochemistry: a time-honored challenge towards low-cost and green energy storage, *NPG Asia Mater.* 12 (2020) 1–24.
<https://doi.org/10.1038/s41427-019-0167-1>.

- [87] K.K. Lee, W.S. Chin, C.H. Sow, Cobalt-based compounds and composites as electrode materials for high-performance electrochemical capacitors, *J. Mater. Chem. A.* 2 (2014) 17212–17248. <https://doi.org/10.1039/c4ta02074j>.
- [88] R.L. Doyle, I.J. Godwin, M.P. Brandon, M.E.G. Lyons, Redox and electrochemical water splitting catalytic properties of hydrated metal oxide modified electrodes, *Phys. Chem. Chem. Phys.* 15 (2013) 13737–13783.
<https://doi.org/10.1039/c3cp51213d>.
- [89] B. Wouters, X. Sheng, A. Boschin, T. Breugelman, E. Ahlberg, I.F.J. Vankelecom, P.P. Pescarmona, A. Hubin, The electrocatalytic behaviour of Pt and Cu nanoparticles supported on carbon nanotubes for the nitrobenzene reduction in ethanol, *Electrochim. Acta.* 111 (2013) 405–410.
<https://doi.org/10.1016/j.electacta.2013.07.210>.
- [90] M.E. Björketun, A.S. Bondarenko, B.L. Abrams, I. Chorkendorff, J. Rossmeisl, Screening of electrocatalytic materials for hydrogen evolution, *Phys. Chem. Chem. Phys.* 12 (2010) 10536–10541. <https://doi.org/10.1039/c003826c>.
- [91] D. Merki, S. Fierro, H. Vrubel, X. Hu, Amorphous molybdenum sulfide films as catalysts for electrochemical hydrogen production in water, *Chem. Sci.* 2 (2011) 1262–1267. <https://doi.org/10.1039/c1sc00117e>.
- [92] S. Anantharaj, K. Karthick, S. Kundu, NiTe₂ Nanowire Outperforms Pt/C in High-Rate Hydrogen Evolution at Extreme pH Conditions, *Inorg. Chem.* 57 (2018) 3082–3096. <https://doi.org/10.1021/acs.inorgchem.7b02947>.
- [93] U.Č. Lačnjevac, B.M. Jović, V.D. Jović, N.V. Krstajić, Determination of kinetic parameters for the hydrogen evolution reaction on the electrodeposited Ni–MoO₂ composite coating in alkaline solution, *J. Electroanal. Chem.* 677–680 (2012) 31–40. <https://doi.org/10.1016/j.jelechem.2012.05.004>.
- [94] G.M. Tomboc, T. Kwon, J. Joo, K. Lee, High entropy alloy electrocatalysts: A critical assessment of fabrication and performance, *J. Mater. Chem. A.* 8 (2020) 14844–14862. <https://doi.org/10.1039/d0ta05176d>.
- [95] V.A. Saveleva, L. Wang, D. Teschner, T. Jones, A.S. Gago, K.A. Friedrich, S. Zafeirotos, R. Schlögl, E.R. Savinova, Operando evidence for a universal oxygen evolution mechanism on thermal and electrochemical iridium oxides, *J. Phys. Chem. Lett.* 9 (2018) 3154–3160.
<https://doi.org/10.1021/acs.jpcclett.8b00810>.

- [96] E. Fabbri, T.J. Schmidt, Oxygen evolution reaction - The enigma in water electrolysis, *ACS Catal.* 8 (2018) 9765–9774. <https://doi.org/10.1021/acscatal.8b02712>.
- [97] P. Rasiyah, A.C.C. Tseung, A mechanistic study of oxygen evolution on NiCo₂O₄: II. Electrochemical kinetics, *J. Electrochem. Soc.* 130 (1983) 2384–2386. <https://doi.org/10.1149/1.2119592>.
- [98] C. Gabrielli, P.P. Grand, A. Lasia, H. Perrot, Investigation of hydrogen adsorption-absorption into thin palladium films, *J. Electrochem. Soc.* 151 (2004) A1925. <https://doi.org/10.1149/1.1797033>.
- [99] H. Duncan, A. Lasia, Mechanism of hydrogen adsorption/absorption at thin Pd layers on Au(1 1 1), *Electrochim. Acta.* 52 (2007) 6195–6205. <https://doi.org/10.1016/j.electacta.2007.03.068>.
- [100] M. Liu, Z. Zhang, F. Okejiri, S. Yang, S. Zhou, S. Dai, Entropy-maximized synthesis of multimetallic nanoparticle catalysts via a ultrasonication-assisted wet chemistry method under ambient conditions, *Adv. Mater. Interfaces.* 6 (2019) 1–6. <https://doi.org/10.1002/admi.201900015>.
- [101] R.K. Singh, A. Schechter, Electrochemical investigation of urea oxidation reaction on β Ni(OH)₂ and Ni/Ni(OH)₂, *Electrochim. Acta.* 278 (2018) 405–411. <https://doi.org/10.1016/j.electacta.2018.05.049>.
- [102] M.B. Stevens, L.J. Enman, E.H. Korkus, J. Zaffran, C.D.M. Trang, J. Asbury, M.G. Kast, M.C. Toroker, S.W. Boettcher, Ternary Ni-Co-Fe oxyhydroxide oxygen evolution catalysts: Intrinsic activity trends, electrical conductivity, and electronic band structure, *Nano Res.* 12 (2019) 2288–2295. <https://doi.org/10.1007/s12274-019-2391-y>.
- [103] X. Bo, Y. Li, X. Chen, C. Zhao, Operando Raman Spectroscopy Reveals Cr-Induced-Phase Reconstruction of NiFe and CoFe Oxyhydroxides for Enhanced Electrocatalytic Water Oxidation, *Chem. Mater.* 32 (2020) 4303–4311. <https://doi.org/10.1021/acs.chemmater.0c01067>.
- [104] C. Xu, J. bo Zhou, M. Zeng, X. ling Fu, X. jiang Liu, J. ming Li, Electrodeposition mechanism and characterization of Ni–Mo alloy and its electrocatalytic performance for hydrogen evolution, *Int. J. Hydrogen Energy.* 41 (2016) 13341–13349. <https://doi.org/10.1016/j.ijhydene.2016.06.205>.
- [105] Q. Wang, X. Wu, L. Zhang, Designed of bifunctional Z-scheme CuSnO₃@Cu₂O heterojunctions film for photoelectrochemical catalytic reduction and ultrasensitive sensing nitrobenzene, *Chem. Eng. J.* 361 (2019) 398–407. <https://doi.org/10.1016/j.cej.2018.12.079>.

- [106] M. Jin, Y. Liu, X. Zhang, J. Wang, S. Zhang, G. Wang, Y. Zhang, H. Yin, H. Zhang, H. Zhao, Selective electrocatalytic hydrogenation of nitrobenzene over copper-platinum alloying catalysts: Experimental and theoretical studies, *Appl. Catal. B Environ.* 298 (2021) 120545.
<https://doi.org/10.1016/j.apcatb.2021.120545>.
- [107] E. Fachinotti, E. Guerrini, A.C. Tavares, S. Trasatti, Electrocatalysis of H₂ evolution by thermally prepared ruthenium oxide. Effect of precursors: Nitrate vs. chloride, *J. Electroanal. Chem.* 600 (2007) 103–112.
<https://doi.org/10.1016/j.jelechem.2006.04.017>.
- [108] Y. Zhao, C. Liu, C. Wang, X. Chong, B. Zhang, Sulfur vacancy-promoted highly selective electrosynthesis of functionalized aminoarenes via transfer hydrogenation of nitroarenes with H₂O over a Co₃S_{4-x} nanosheet cathode, *CCS Chem.* 3 (2021) 507–515.
<https://doi.org/10.31635/ccschem.020.202000218>.
- [109] R.Q. Yao, Y.T. Zhou, H. Shi, W. Bin Wan, Q.H. Zhang, L. Gu, Y.F. Zhu, Z. Wen, X.Y. Lang, Q. Jiang, Nanoporous surface high-entropy alloys as highly efficient multisite electrocatalysts for nonacidic hydrogen Evolution reaction, *Adv. Funct. Mater.* 31 (2021) 1–9. <https://doi.org/10.1002/adfm.202009613>.
- [110] A. Lasia, *Electrochemical Impedance Spectroscopy and its Applications* Andrzej, Springer, 1999.
- [111] A. Goswami, R.G. Kadam, J. Tuček, Z. Sofer, D. Bouša, R.S. Varma, M.B. Gawande, R. Zbořil, Fe⁽⁰⁾-embedded thermally reduced graphene oxide as efficient nanocatalyst for reduction of nitro compounds to amines, *Chem. Eng. J.* 382 (2020). <https://doi.org/10.1016/j.cej.2019.122469>.
- [112] X. Duan, J. Yin, M. Huang, P. Wang, J. Zhang, Hydrogenation kinetics of halogenated nitroaromatics over Pt/C in a continuous Micro-packed bed reactor, *Chem. Eng. Sci.* 251 (2022) 117483.
<https://doi.org/10.1016/j.ces.2022.117483>.

VITA

NAME Victor Manuel Marquez espinosa

DATE OF BIRTH 08 July 1989

PLACE OF BIRTH Caracas, Venezuela

INSTITUTIONS ATTENDED Simon Bolivar University, M.Sc. in Chemistry
Simon Bolivar University, B.Sc. in Chemistry

HOME ADDRESS Soi Charoen Nakhon 17, Bang Lamphu Lang, Khlong San, Bangkok 10600

PUBLICATION V. Márquez, M. Fereidooni, J.S. Santos, S. Praserthdam, P. Praserthdam, Effect of the annealing temperature of multi-elemental oxides (FeCoNiCuZn) y O x on the electrocatalytic hydrogenation of nitrobenzene at room temperature, *Electrochim. Acta.* 428 (2022) 140975.

V. Márquez, J.S. Santos, J.G. Buijnsters, S. Praserthdam, P. Praserthdam, Simple, controllable and environmentally friendly synthesis of FeCoNiCuZn-based high-entropy alloy (HEA) catalysts, and their surface dynamics during nitrobenzene hydrogenation, *Electrochim. Acta.* 410 (2022).